Oral nanocrystal formulations
and their biopharmaceutical characterization

Katharina Anhalt

Dissertation

submitted to the

Combined Faculties of the Natural Sciences and Mathematics

of the Ruperto-Carola-University of Heidelberg, Germany

for the degree of

Doctor of Natural Sciences

presented by

Katharina Anhalt

Apothekerin

born in Bad Friedrichshall, Germany

Oral examination: November 5, 2012

Oral nanocrystal formulations

and their biopharmaceutical characterization

Referees

Prof. Dr. Gert Fricker

Prof. Dr. Jürgen Reichling

Abstract

The aim of this thesis was a biopharmaceutical characterization of oral nanocrystal formulations. Crystalline nanosuspensions (nanocrystals) are one of the most promising and successful formulation approaches for the bioavailability enhancement of poorly water soluble drugs. Crystalline nano- and microsuspensions of fenofibrate and the Merck Serono Compound AS were prepared by wet media milling. The suspensions covered a wide particle size range (100 nm to 8 μm) and exhibited narrow particle size distributions.

It was challenging to determine the solubility and dissolution of nanocrystal formulations. Very small particles with rapid dissolution kinetics complicated the separation of solid from dissolved material. Therefore, an in situ noninvasive analytical method based on the monitoring of light scattering intensities was developed. It avoided the critical separation step, both in solubility and dissolution testing. The determination of solubilities revealed that the solubility was slightly increased only by the smallest sized nanocrystals ($10 - 20\,\%$ for particle size < 200 nm).

The dissolution assessment by the light scattering technique had a high temporal resolution, sensitivity, and reproducibility. A straightforward and small scale experimental setup was an additional advantage. The ideal applicability was observed for particle diameters of $100 - 500$ nm. Dissolution times as short as 90 s could be determined. The method was still applicable for dissolution of particles with up to 1 μm in size and a good correlation to a conventional dissolution setup (USP II apparatus with sample filtration) was demonstrated for suspensions in this size range. Biexponential modeling of the dissolution curves was successful and allowed for analysis of the dissolution kinetics. The experimental dissolution results were in good agreement to the Noyes-Whitney theory of dissolution.

The next step of biopharmaceutical characterization was the permeability assessment of drug substances formulated as crystalline suspensions with various particle sizes. The permeabilities were measured across Caco-2 cell monolayers. An assay with vertical monolayer arrangement was compared to the classical horizontal assay. The vertical setup did not improve the discriminative power and the adjustment of standardized experimental conditions was difficult. Therefore, the horizontal setup was selected for further experiments. A variation of apical transport medium by using a biorelevant medium instead of a classical buffered salt solution did not alter the permeabilities essentially.

A nanosuspension (150 nm) of the Merck Serono Compound AS enabled a higher permeability with reference to larger sized suspensions (860 nm and 7 μm). This correlated well with an observed accelerated dissolution and an observed slight increase in solubility of the nanosuspension. On the contrary, a positive effect of size reduction on permeability was not detected for fenofibrate. This unexpected result might be due to the enzymatic fenofibrate conversion to fenofibric acid, a better soluble and evenly permeable metabolite. A correlation of permeability with apical fenofibric acid concentration dominated the

correlation of permeability with particle size. The metabolization interfered with the effects of particle size reduction. However, this phenomenon was not explicitly investigated in this study.

The biopharmaceutical investigation was completed by pharmacokinetic studies on the oral administration of suspensions to rats. Nanosuspensions of both drug substances improved the bioavailability with reference to microsuspensions.

The presented work covers a thorough particle size distribution analysis, solubility, dissolution, permeation and *in vivo* pharmacokinetic investigation of micro- and nanosuspensions of two drug substances. These data are very useful to investigate the *in vitro-in vivo* relation of oral nanocrystal formulations. In this work a good linear correlation of the logarithmic dissolution times to the bioavailability was demonstrated. Furthermore plasma concentration-time profiles were successfully simulated using the Advanced Compartmental Absorption and Transit (ACAT) model. For nanocrystal formulations the fit of simulated to observed profiles was improved by applying the nanofactor effect implemented in the ACAT model.

Zusammenfassung

Ziel dieser Arbeit war eine biopharmazeutische Charakterisierung von oralen nanokristallinen Formulierungen. Kristalline Nanosuspensionen (Nanokristalle) sind einer der erfolgreichsten Ansätze zur Verbesserung der Bioverfügbarkeit von schwer wasserlöslichen Arzneistoffen. Kristalline Nano- und Mikrosuspensionen des Arzneistoffes Fenofibrat und des Merck Serono Wirkstoffes AS wurden mittels Nassvermahlung hergestellt. Die Partikelgröße wurde schrittweise reduziert um einen breiten Größenbereich abzudecken (100 nm bis 8 μm). Die Suspensionen zeigten eine enge Partikelgrößenverteilung.

Die Messung der Löslichkeit und Freisetzung von Nanokristall Formulierungen bergen besondere Herausforderungen. Da es sich um äußerst kleine Partikel mir sehr schneller Auflösungskinetik handelt, ist die Abtrennung der festen Partikel vom gelösten Material schwierig. Deshalb wurde eine nichtinvasive analytische Methode basierend auf der Messung der Intensität des Streulichtes entwickelt. Sowohl für die Löslichkeits- als auch für die Freisetzungsbestimmung konnte der kritische Separationsschritt durch die neue Methode vermieden werden. Die Löslichkeitsmessungen ergaben, dass nur die Löslichkeit der kleinsten Nanokristalle geringfügig gesteigert wurde (10 − 20 % für Partikel < 200 nm).

Die Freisetzungsmessung mittels der Lichtstreumethode zeigte eine hohe zeitliche Auflösung, Sensitivität und Reproduzierbarkeit. Ein unkomplizierter experimenteller Aufbau im Kleinstmaßstab war ein weiterer Vorteil. Der optimalen Anwendungsbereich lag im Partikelgrößenbereich von 100 − 500 nm. Auflösungszeiten bis zu minimal 90 s konnten bestimmt werden. Auch für die Freisetzungsmessung im Partikelgrößenbereich bis zu 1 μm war die Methode anwendbar. Eine gute Übereinstimmung der Ergebnisse mit einer konventionellen Freisetzungsbestimmung (Blattrührer Apparatur und Probenfiltration) konnte für diesen Größenbereich gezeigt werden. Die Freisetzungskurven konnten durch eine biexponentielle Funktion erfolgreich beschrieben werden und dies ermöglichte die Analyse der Auflösungskinetik. Die experimentellen Ergebnisse stimmten gut mit der Noyes-Whitney Theorie der Freisetzung überein.

Einen weiterer Baustein der biopharmazeutischen Charakterisierung war die Permeabilitätsmessung der als kristalline Suspensionen formulierten Wirkstoffe. Das Caco-2 Zellkulturmodel wurde für die Bestimmung der Permeabilitäten verwendet. Ein vertikaler wurde mit einem klassischen horizontalen Versuchsaufbau verglichen. Keine positive Auswirkung des vertikalen Aufbaus auf die Unterscheidbarkeit von Formulierungen wurde festgestellt und die Einstellung standardisierter experimenteller Bedingungen im vertikalen System war schwierig. Folglich wurde der horizontale Aufbau für die weiteren Versuche gewählt. Die Verwendung eines biorelevanten Transportmediums als alternatives apikales Medium beeinfusste die Permeabilitäten nur unwesentlich im Vergleich mit einer klassischen gepufferten Salzlösung.

Eine Nanosuspension des Wirkstoffes AS mit 150 nm mittlerem Teilchendurchmesser zeigte eine höhere

Permeabilität als Suspensionen mit größeren Partikeln (860 nm und 7 μm). Dies korreliert mit der Beobachtung einer schnelleren Auflösung und einer leicht erhöhten Löslichkeit der Nanosuspension. Dahingegen wurde für Fenofibrat kein positiver Einfluss der Partikelgrößenreduktion auf die Permeabilität beobachtet. Dieses unerwartete Ergebnis ist möglicherweise durch die enzymatische Esterspaltung von Fenofibrat zu Fenofibrinsäure bedingt, welche im Caco-2 Versuch auftritt. Fenofibrinsäure ist besser löslich und ebenso permeabel wie Fenofibrat. Die Korrelation von Permeabilität mit der apikalen Fenofibrinsäurekonzentration war deutlicher als die Korrelation von Permeabilität und Partikelgröße. Die Metabolisierung überlagerte den Einfluss der Partikelgrößenreduktion. Jedoch wurden diese Zusammenhänge in der vorliegenden Arbeit nicht systematisch untersucht.

Abgerundet wurde die biopharmazeutische Untersuchung durch *in vivo* Pharmakokinetikstudien, in denen Suspensionsformulierungen oral an Ratten verabreicht wurden. Nanosuspensionen beider Wirkstoffe verbesserten die Bioverfügbarkeit im Vergleich zu Mikrosuspensionen.

Diese Arbeit umfasst eine gründliche Untersuchung der Partikelgrößenverteilung, eine Bestimmung der Löslichkeit, Freisetzung, Permeation und *in vivo* Pharmakokinetik für Mikro- und Nanosuspensionen zweier verschiedener Wirkstoffe. Diese Daten sind sehr wertvoll für eine Untersuchung der *in vitro-in vivo* Beziehung von oralen kristallinen Nanosuspensionen. In der vorliegenden Arbeit wurde eine gute lineare Korrelation der logarithmischen Auflösungszeit zur Bioverfügbarkeit gezeigt. Weiterhin konnten Plasma Konzentrations-Zeit Verläufe erfolgreich mittels des erweiterten Absorptions-Kompartimentmodel (ACAT) simuliert werden. Für nanokristalline Formulierungen wurde die Übereinstimmung simulierter und experimenteller Daten durch die Anwendung des Nanofaktor Effektes im ACAT Model verbessert.

Contents

1

Introduction

1.1 Nanocrystal technology

Many new drug candidates exhibit poor water solubility and thus low bioavailability after oral admin-
istration. This forms a major challenge for formulation scientists and the nanocrystal technology has
emerged as a valuable tool to build the bridge between drug discovery and (pre)clinical application (Lip-
inski 2002; Rabinow 2004; Kesisoglou et al. 2007). The oral administration of nanosuspensions offers the
advantages of enhanced bioavailability, reduced variability and diminished food effect (Rabinow 2004;
Kesisoglou et al. 2007; Muller 2000; Van Eerdenbrugh et al. 2010; Quinn et al. 2012). In the following
a short introduction will be given into preparation methods, market products and the physico-chemical
properties leading to favorable *in vivo* performance of nanocrystals.

Crystalline nanosuspensions are defined as colloidal aqueous dispersions of submicron sized active phar-
maceutical ingredient (API) crystals and are stabilized by electrostatic and steric stabilizers (Rabinow
2004; Kesisoglou et al. 2007; Muller 2000). There are two main approaches to produce nanosized API
crystals: the 'top down' and the 'bottom up' technologies. The term 'bottom up' summarizes controlled
precipitation/crystallization techniques. The 'top down' approach is applied more often. API crystals
are downsized by crushing and mechanical attrition. This is realized by high-pressure homogenization
(e.g. the DissoCubes® technology) or by wet media milling (e.g. the NanoCrystal® technology). Stabi-
lizers which adsorb to the particle surface are required to prepare a stable formulation. They protect the
submicron sized particles against inter-particle forces leading to aggregation. Polymers (e.g. cellulose
derivatives) are used as steric stabilizers and anionic surfactants (e.g. sodium laurylsulfate or dioctyl
sulfosuccinate) typically function as electrostatic stabilizers. In Table 1.1 the currently available market
products based on nanocrystalline API are listed (Kesisoglou et al. 2007; Van Eerdenbrugh et al. 2008).

Table 1.1: Marketed pharmaceutical products based on nanocrystalline drug substance.

Product	Drug substance	Company	Technology	Approved[1]
RAPAMUNE®	Sirolimus	Wyeth	NanoCrystal®[2]	2000
EMEND®	Aprepitant	Merck	NanoCrystal®	2003
TriCor®	Fenofibrate	Abbott	NanoCrystal®	2004
MEGACE® ES	Megestrol acetate	PAR Pharmaceuticals	NanoCrystal®	2005
Triglide[TM]	Fenofibrate	SkyPharma[3]	IDD®-P[4]	2005

[1] Date of Approval by the US Food and Drug Administration.   [2] Elan Drug Delivery NanoCrystal®.
[3] Shionogi/First Horizon Pharmaceuticals   [4] Insoluble Drug Delivery-Microparticle.

The improvement in bioavailability by orally administered nanocrystalline API is attributed to an enhanced dissolution rate through enlarged surface area and to an increased solubility. A high curvature, the creation of high energy surfaces and a less ordered structure of molecules in nanocrystals have been suggested to give further contributions (Van Eerdenbrugh et al. 2010). Two equations are most often quoted to provide the physico-chemical background of these phenomena. The Noyes-Whitney equation with modifications by Nernst and Brunner (Noyes and Whitney 1897; Nernst 1904; Brunner 1904; Costa and Sousa Lobo 2001) describes a proportional increase in dissolution rate with increasing surface area (Eq. 1.2). The increase in saturation solubility is described by the Ostwald-Freundlich equation (Ostwald 1900; Freundlich 1923; Kesisoglou et al. 2007):

$$C_{S,r} = C_{S,\infty} \exp\left(\frac{2\gamma M}{r\rho RT}\right) \tag{1.1}$$

where $C_{S,r}$ is the saturation solubility of a particle with radius r, $C_{S,\infty}$ is the saturation solubility of infinitely large particle, γ is the particle medium interfacial tension, M is the compound molecular weight, ρ is the particle density, R the universal gas constant and T the absolute temperature. However, recent publications report solubility increases of not more than 15%, which is in good agreement with the Ostwald-Freundlich equation. An only small solubility increase highlights the role of an enhanced dissolution rate for the bioavailability improvement by nanocrystals (Jinno et al. 2006; Kesisoglou and Wu 2008; Van Eerdenbrugh et al. 2010).

1.2   Biopharmaceutics

In the development of drug substances and drug products not only pharmacology but also biopharmaceutics is an integral component. Biopharmaceutics relates pharmacodynamics (effect of the drug on the organism) to pharmacokinetics (effect of the organism on the drug). It deals with the interdependence of biological aspects of the living organism and physical-chemical characteristics of the drug substance and formulations. The processes of absorption (A), distribution (D), metabolism (M) and elimination (E) are important for the *in vivo* performance of a drug. They are often summarized in the term ADME. Additionally the liberation of drug molecules from solid dosage forms has been recognized to influence pharmacokinetics, since drug molecules are required to be in the solution phase for absorption (Langguth et al. 2004; Krishna and Yu 2008).
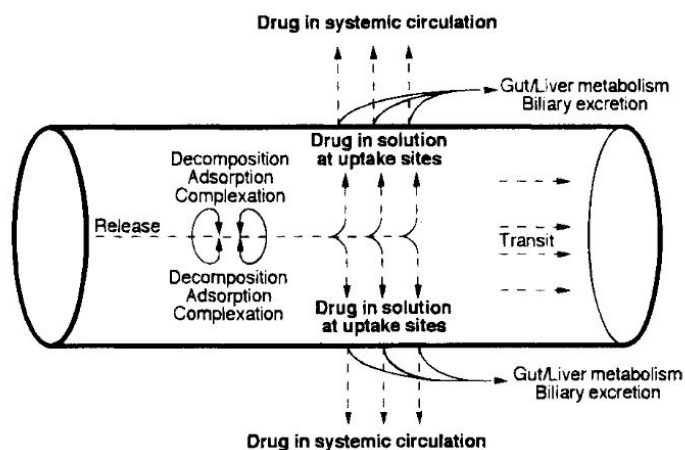
Figure 1.1: A schematic representation of the factors that determine the fraction of drug absorbed across the intestinal mucosa. Reproduced from Dressman et al. (1998) with kind permission from Springer Science and Business Media.

The bioavailability is one of the principal *in vivo* pharmacokinetic parameters of a drug or drug formulation. Bioavailability is defined as the rate and extent to which a drug or its active moiety is absorbed and reaches the systemic circulation, thereby accessing the side of action (Langguth et al. 2004; Krishna and Yu 2008). The rate limiting factors to oral drug absorption were summarized by Dressman et al. (1998) and are illustrated in Figure 1.1. Incomplete absorption can be referred to

- incomplete dissolution at the gastrointestinal (GI) sites where it is well absorbed

- decomposition in the GI tract or formation of nonabsorbable complexes

- insufficient transport across the GI wall

- first pass metabolization or elimination.

In 1995 Amidon et al. (1995) introduced the biopharmaceutical classification system (BCS), which is based on the understanding that the rate and extent of intestinal absorption is controlled by the solubility and permeability of a drug. Both the amount of drug in solution at the epithelial barrier and the ability of that drug to diffuse across the gastrointestinal wall determine absorption. According to the BCS drugs are classified into four groups: BCS I (high solubility, high permeability), BCS II (low solubility, high permeability), BCS III (high solubility, low permeability) and BCS IV (low solubility, low permeability). The BCS has implications on the development of new drug products. For drugs with low solubility (BCS II and IV) formulation factors influencing dissolution rate or solubility have a great potential to influence the absorption. These factors may for example be the drug particle size or solubilizing excipients. Kawabata et al. (2011) recently reviewed the basic approaches and practical applications of the BCS in formulation development. An *in vitro-in vivo* correlation based on the dissolution rate can most likely be established for BCS II drugs, since dissolution is most often the rate-limiting step of absorption (Amidon et al. 1995).

In vitro dissolution and permeation tests are continuously modified to closely simulate physiological conditions and to meet the requirements of innovative dosage forms. The aim is to predict the rate and extent of drug absorption *in vivo*. In the following the basics and current developments in *in vitro* dissolution and permeation testing will be reviewed.

1.2.1   Dissolution

Dissolution is the process by which drug molecules are liberated from a solid phase and enter into a solution phase. *In vitro* dissolution studies are especially important in the development of every oral dosage form. They are not only used to predict how drug products will perform in patients. *In vitro* drug release kinetics are also an integral component of quality control testing (Sinko 2005). Furthermore *in vitro* dissolution testing plays a role in bioequivalence studies. The Food and Drug Administration (FDA) defines criteria under which *in vitro* dissolution testing can fully replace *in vivo* studies for BCS I drugs (FDA Guidance for Industry: Waiver of In Vivo Bioavailability and Bioequivalence Studies for Immediate-Release Solid Oral Dosage Forms Based on a Biopharmaceutics Classification System).
The forthcoming sections will provide an outline of mathematical dissolution models and experimental dissolution methods with the focus on nanoparticle dissolution.

Theories and mathematical models of dissolution

The dissolution process consists of two consecutive steps. The first step is the interfacial reaction, meaning the liberation of molecules from the solid surface. The second step is the transport of solutes from the solid-liquid interface into the bulk solution (Lee et al. 2008).
The diffusion layer model assumes that the interfacial reaction happens instantaneously and that the dissolution process is controlled by diffusion of liberated molecules through the stagnant liquid film layer surrounding the particle (diffusion layer) into the bulk solution. This model, which is based on the Fick´s first law, was developed by Noyes and Whitney and was modified by Nernst and Brunner (Noyes and Whitney 1897; Nernst 1904; Brunner 1904).

$$\frac{dm}{dt} = \frac{A_0 D}{h}(C_S - C) \tag{1.2}$$

where dm/dt is mass rate of dissolution, A_0 is the total surface area, D is the diffusion coefficient, h is the effective boundary layer thickness, C_S is the saturation solubility and C is the concentration of solute in the bulk solution at time t.
In this model the total surface area A_0 and the effective boundary layer thickness h are held constant during dissolution. Many authors describe that for particle dissolution, and especially for nanoparticle dissolution, this assumptions need to be refined. In the Higuchi-Hiestand equation the boundary layer h decreases proportionally with particle size r (Higuchi and Hiestand 1963; Higuchi et al. 1963). Johnson and coworkers specified this concept. They developed a theoretical model to describe the dissolution of polydisperse powders under non-sink conditions. They introduced a transition particle radius $r_{transition}$. Below this radius the diffusion layer thickness equals the particle radius ($h = r$) and above this radius

the diffusion layer thickness reaches a maximum value of h_{max} irrespective of particle size (Hintz and Johnson 1989; Johnson 2012). The following equations are derived:

$$\frac{dX_{S_i}}{dt} = -\frac{3DX_{0_i}^{1/3}X_{S_i}^{2/3}}{\rho h_i r_{0_i}}\left(C_{S_i} - \frac{X_{d_T}}{V}\right)$$ (1.3)

with

$$r_i = \left(\frac{3X_{S_i}}{4\pi\rho N_{0_i}}\right)^{1/3}$$ (1.4)

where the subscript i denotes a particle size fraction and where X_{S_i} is the mass of solid drug in particle size fraction i, X_{0_i} is the initial mass of solid drug, D is the diffusion coefficient, ρ is the drug density, h_i is the particle size dependent diffusion layer thickness, r_{0_i} is the initial radius of particles, r_i is the radius of particles, C_{S_i} is the particle size dependent solubility of drug particles (calculated by the Ostwald-Freundlich equation (Eq. 1.1)), X_{d_T} is the total mass of drug in solution from all size fractions, V is the dissolution volume, and N_{0_i} is the initial number of particles. The Johnson dissolution model takes into account changes in particle radius, diffusion layer and solubility. Additionally every size fraction of a particle size distribution is modeled individually.

An experimental confirmation that the particle radius is approximately equal to the boundary layer thickness was presented by Galli (2006) for particles with diameters of $0.5 - 5.9\,\mu$m. However, Wang and Flanagan (1999) proposed a general solution for diffusion-controlled dissolution of spherical particles, which assumes a constant diffusion layer thickness. Both models have been successfully applied to model experimental data (Johnson 2012).

The Johnson and the Wang-Flanagan equations consider many parameters. With the cube-root law and the Weibull function two more simple and often applied models will be shortly summarized. Hixson and Crowell (1931) considered that the surface area of a particle or dosage form diminishes during dissolution. They derived a cube-root law

$$W_0^{1/3} - W_t^{1/3} = \kappa * t$$ (1.5)

where W_0 is the initial amount of drug, W_t is the remaining solid amount of drug at the time t and κ is a constant incorporating the surface-volume relation (Costa and Sousa Lobo 2001).

The Weibull function is a general empirical equation and was adopted to model dissolution curves (Langenbucher 1972). It has ubiquitous applicability to dissolution curves obtained under versatile conditions. Recently attempts have been made to assign some mechanistic / kinetic meaning to the empirical Weibull parameters (Dokoumetzidis et al. 2006).

The presented models provide a first insight into the field of dissolution theories and modeling. The interested reader will find additional models in literature, for example in Langguth et al. (2004); Costa and Sousa Lobo (2001); Lee et al. (2008); Judefeind and Villiers (2009).
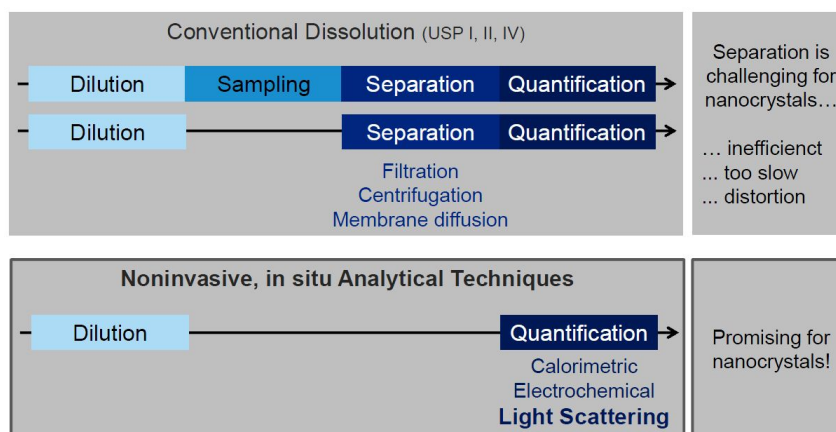
Figure 1.2: The principles and operation steps of different dissolution techniques (left boxes) and their suitability for nanocrystal dissolution testing (right boxes). (above) Compendial/conventional methods categorized as sampling and separation or membrane diffusion techniques and (below) in situ noninvasive techniques with examples of potential analytical methods.

In vitro dissolution testing

Various techniques are applied for dissolution testing of drug substances and pharmaceutical dosage forms. Most commonly the methods of the European and United States Pharmacopoeias (Ph. Eur. and USP) are used. For testing of immediate-release oral solid dosage forms the closed systems basket (USP I) and paddle (USP II) apparatus are the methods of choice. The apparatus consists of a rotating basket or paddle in a large vessel filled with $500 - 1000$ ml of dissolution medium. Usually samples are withdrawn and the undissolved material is filtered off to spectroscopically quantify the dissolved fraction of the dose. The reciprocating cylinder (USP III) and the flowthrough cell (USP IV) are alternative methods. They can be operated as closed or open systems and are most commonly used for modified-release systems, however, are not dedicated to this applications (Sinko 2005). Figure 1.2 summarizes the operation steps of the compendial/conventional dissolutions methods.

Commonly used media are aqueous salt solutions or buffers with or without the addition of surfactants. More physiological media are required to set up meaningful *in vitro-in vivo* correlations. As biorelevant dissolution media fasted state-simulated intestinal fluid (FaSSIF) or fed state-simulated intestinal fluid (FeSSIF) containing bile salts and phospholipids are frequently used (Galia et al. 1998; Kleberg et al. 2010).

Experimental methods for in vitro nanoparticle dissolution testing

The analytical question of determining the dissolution rate of nanoparticles was raised by Heng et al. (2008) who asked 'What is a suitable dissolution method for drug nanoparticles?'. Basically the disso-lution methods proposed in literature can be categorized as (a) being based on sampling and separation, (b) consisting of a membrane diffusion setup, or (c) true in situ analytical techniques (Fig. 1.2). (a) The sampling and separation technique prevails in many published studies where filtration, (ultra-) centrifugation or centrifugal-filtration are used to separate undissolved nanoparticles from dissolved API

(Xia et al. 2010; Shono et al. 2010; Jinno et al. 2008; Laaksonen et al. 2011; Li et al. 2011). Juenemann et al. (2011b) focused on the filtration step and concluded that pore sizes of $\leq 0.1\mu m$ result in predictive dissolution profiles. Shortcomings of all applied separation techniques are that they are slow and inefficient when applied to rapidly dissolving particles. It is challenging to separate particles that are less than a hundred nanometers in size, which shrink during the dissolution process. Furthermore, invasive separation steps, in which the systems to be analyzed are subjected to different forces, might alter the dissolution process. Due to the poor solubility of APIs, the dissolved concentrations are usually in the lower $\mu g/ml$ range. Taking this limitation into account, it is not favorable to perform a dissolution experiment which exposes the API to large surfaces and is therefore inevitably accompanied by adsorptive loss of API.

(b) The concept of membrane diffusion covers dialysis or reverse dialysis methods (Heng et al. 2008) and continuous flow membrane filtration under pressure (Magenheim et al. 1993; Helle et al. 2010). Recently, efforts have been made to modify compendial methods with dialysis membranes (USP apparatus IV (Bhardwaj and Burgess 2010) and USP apparatus I (Abdel-Mottaleb and Lamprecht 2011)). For studies on sustained release nanoparticulate formulations with an undissolvable matrix membrane diffusion techniques are eligible. However, results are heavily distorted for rapidly dissolving nanocrystals due to comparatively slow membrane diffusion kinetics of drug molecules. Also a microdialysis system was evaluated not suitable to measure dissolution of nanocrystals, since the surfactants and micelles commonly employed in dissolution media for poorly water soluble drugs cause problems (Junemann and Dressman 2012).

(c) In situ analytical techniques, which avoid the need to separate dissolved API, are certainly the most promising approach to assess nanocrystal dissolution. Ideally, they are designed as on-line and real-time methods with high temporal resolution and have a noninvasive character. Being implemented in dissolution testing of conventional solid dosage forms it was an obvious step to use UV/VIS fiber optic probes (Aldridge et al. 1995; Chen and Brown 1994; Tsinman et al. 2009; Alonzo et al. 2010; Galli 2006). However, recent research disproves the use of this technique for nanosized material due to the light absorption by nanoparticles (Van Eerdenbrugh et al. 2011). Moreover electrochemical analytics, like polarography, potentiometry and voltammetry, have been suggested, but are limited to electroactive APIs (Charalampopoulos et al. 2003; Rosenblatt et al. 2007; Mora et al. 2009; Juenemann et al. 2011a). Junemann and Dressman (2012) proposed to use the ultrasonic resonator technology, which measures the sound velocity in liquid samples, which is dependent on the solute concentration. This technique was too slow and not sensitive enough to detect fenofibrate in a saturated FaSSIF solution. Solution calorimetry has been applied to measure nanocrystal dissolution (Kayaert et al. 2010). Calorimetry detects many phenomena associated with any kind of molecular interaction and it is challenging to extract the net proportion of heat change resulting from particle dissolution. Nevertheless a sound method development could provide a platform for the measurement of nanoparticle dissolution by calorimetric methods in future. Finally, a turbidimetric approach to assess small particle dissolution was introduced by Tucker (2002) and was followed up by Crisp et al. (2007) and Chaubal and Popescu (2008). The use of the light scattering properties of particles dispersed in liquid to monitor dissolution generated promising results and encourages further research.

1.2.2 Permeation

The absorption of drug molecules across the intestinal membrane can basically follow two different paths. Either the drug permeates through the cell crossing the apical membrane, the cytosol and the basolateral membrane (transcellular route) or the drug transits through the water filled pores between epithelial cells thereby crossing the tight junctions (paracellular route). On both routes passive diffusion along a concentration gradient is the driving force. The physicochemical properties of a drug molecule determine the preferred pathway and the rate of permeation, the permeability. The molecules aqueous solubility, its lipophilicity, molecule size, polarity and ionizability play a role. Small, hydrophilic molecules, for instance, prefer the paracellular route (Karlsson et al. 1999). Lipophilic molecules partition into the cell membrane more easily and passage transcellularly. Passive transcellular permeability shows a predicted maximum for a octanol/water partition coefficient (log P) of 2 and decreases if log P values of 4 are exceeded (Artursson et al. 2001). Passive transcellular permeability is the main mechanism of absorption for many lipophilic compounds.

In addition to passive diffusive processes carriers can be involved in the transcellular pathway, if the drug molecule is substrate of a specific transporter localized in the cell membrane. Carrier-mediated uptake occurs via active transporters or passive transporters (facilitated diffusion) (Buckley et al. 2012; Balimane et al. 2006). Efflux transporters play a more important role in drug molecule permeation across epithelial barriers, since pharmaceuticals can be recognized as xenobiotics, the exposure to which the organism tries to minimize. The efflux transporters transport the substrates against a concentration gradient and adenosine triphosphate (ATP) hydrolysis supplies the energy for this active transport. P-glycoprotein (P-gp) or the multidrug resistance-associated protein 2 (MRP-2) are only two prominent examples (Fricker and Miller 2002). Finally endo- or transcytosis are possible transport mechanisms in which the drug does not pass the membrane but is entrapped and transported in vesicles formed by invagination of the plasma membrane.

In vitro permeation testing

Various methods are used as model systems for intestinal epithelial permeability and they can be classified into artificial membrane and cell culture systems. Buckley et al. (2012); Balimane et al. (2006); Hidalgo (2001); Braun et al. (2000) published excellent reviews, which will guide the reader through the variety of models and protocols, give an industrial perspective on permeability assessment, and describe current developments in permeability testing of poorly water soluble drugs.

The human colon carcinoma cell line Caco-2 plays the most important role in cell culture-based *in vitro* permeability testing. It displays many characteristics of the *in vivo* epithelial permeation barrier: Tight junctions, microvilli, metabolizing enzymes, and a wide range of drug transporters. As main differences to the *in vivo* situation were identified: the lack of a mucus layer adjacent to the cell surface, and a variable and in general lower expression level of transporters and enzymes (Ohura et al. 2010). Compared to artificial systems the work with biological systems is time consuming and costly. Their higher inherent variability adds effort and limits comparability. However, biological systems are more predictive for the *in vivo* situation. Figure 1.3 shows a schematic representation of a Caco-2 permeability assay.
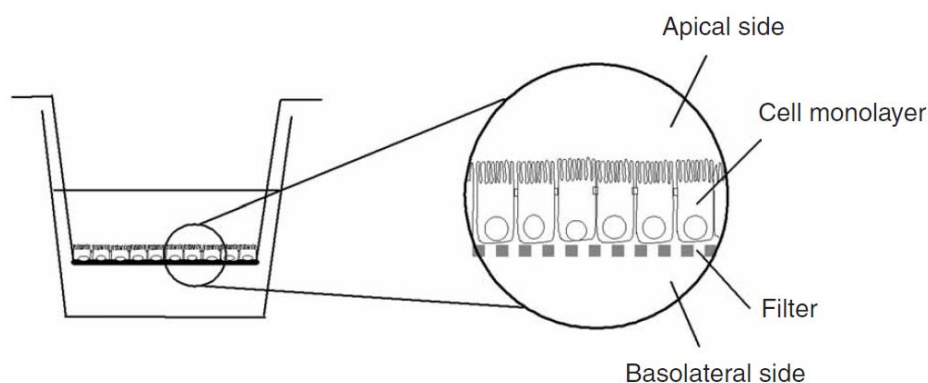
Figure 1.3: *In vitro* drug permeability assay. A cell monolyer (e.g. Caco-2 cells) grown on a permeable filter support forms the barrier between apical and basolateral compartment. Reprinted by permission from Macmillan Publishers Ltd: Nature Protocols (Hubatsch et al. 2007), copyright (2007) by Nature Publishing Group.

The permeability of drugs has been extensively studied by *in vitro* assays with Caco-2 monolayers (Braun et al. 2000). In general drugs are applied as solutions to the apical side. As transport media buffered saline solutions, supplemented with glucose are applied. Most often Hank´s balanced salt solution (HBSS) and Krebs bicarbonate Ringer solution (KBR) are used and often a pH gradient with pH 6.5 apically and pH 7.4 basolaterally mimicking phyiological conditions in the intestine is established (Braun et al. 2000; Ingels and Augustijns 2003; Buckley et al. 2012).

Attempts have been made to modify the experimental setup of permeability assays to overcome some of the hurdles associated with the permeability testing of poorly soluble drugs. As problems insufficient concentrations in the donor and receiver compartment, adsorption of API to the apparatus surfaces and accumulation in the permeation barrier have been identified. Consequences can be poor API recovery, non-sink conditions and analytical challenges (Buckley et al. 2012).

As an alternative to the standard horizontal setup (Fig. 1.3) a side-by-side diffusion chamber system with vertical orientation of the Caco-2 monolayer has been proposed (Hidalgo et al. 1991; Karlsson and Artursson 1992; Rubas et al. 1996; Yu and Sinko 1997; Braun et al. 2000). In *ex-vivo* transport experiments with excised tissues the vertical setup is widespread and side-by-side ussing chambers are used, which are similar to the used side-by-side diffusion chambers (Tsutsumi et al. 2003). The transport buffer is circulated by a gas-lift system and flows in parallel to the surface of the cell monolayer (Hidalgo et al. 1991). Improved hydrodynamics have been identified as a main advantage of this system. A reduction of the unstirred water layer (UWL) adjacent to the monolayer was achieved, which is close to physiological conditions in humans (Karlsson and Artursson 1992). The UWL forms a significant resistance to the permeation of highly permeable/lipohilic drugs, many of which are poorly soluble. Consequently control and minimization of the UWL in permeability assays can result in more meaningful permeability estimates of lipophilic compounds (Tsutsumi et al. 2003; Buckley et al. 2012).

Another more popular strategy to cope with the challenges associated with permeability testing of poorly soluble drugs is the modification of transport media. The addition of cosolvents and/or solubilizers has

been extensively studied, since higher dissolved concentrations can be achieved and the wettability of APIs can be improved. The cosolvent dimethylsulfoxide (DMSO) at concentrations of $\leq 1\%$ is used in standard screening procedures (Hidalgo 2001; Ingels and Augustijns 2003; Balimane et al. 2006). Within this development a focus was set on biorelevant amphiphilic molecules like bile salts and phospholipids. In addition to their solubilizing properties they mimic phyiological conditions and an improved *in vitro-in vivo* correlation is expected. The use of biorelevant media for transport studies goes in parallel with their use in dissoluion studies. Phosphatidylcholine (PC) and sodium taurocholate (NaTC) are most frequently used, since they are the most abundant phospholipid/bile salt in human bile secretions. 3 mM lecithin and 0.75 mM NaTC are often chosen to mimick the fasted condition. These concentrations are equally used in the fasted state simulated intestinal fluid (FaSSIF) for dissolution studies (Galia et al. 1998; Kleberg et al. 2010). On the basolateral side a media supplementation with bovine serum albumin (BSA) $1-4.5\%$ was successfully applied to mimick *in vivo* conditions and to enhance the API recovery (Saha and Kou 2002; Kataoka et al. 2003; Fossati et al. 2008).

A good compatibility of biorelevent media with Caco-2 cells was demonstrated, with respect to monolayer integrity and cell viability (Ingels et al. 2002, 2004; Patel et al. 2006; Fossati et al. 2008). Different effects on the permeability compared to standard media have been described. Permeabilities were increased by 60%, decreased by 75% or remained unaffected (Kleberg et al. 2010). In studies with a broad range of compounds (BCS I-IV) the overall correlation of *in vitro* permeability to *in vivo* fraction absorbed in humans was found to be very similar when comparing standard and biorelevant media. Impact was shown on the permeability of poorly water soluble drugs and the recovery of lipophilic compounds was improved. However, the inhibitory effect of NaTC on P-gp efflux transporters has to be carefully considered (Ingels et al. 2004; Fossati et al. 2008).

Only few mechanistic studies on the effect of biorelevant media on permeability are available. Micellar encapsulation, modulation of membrane fluidity and modulation of activity of membrane transporters have been suggested to give contributions. It is thought that only free drug molecules in solution are absorbable. Colloids might function as cargos delivering encapsulated drug molecules across the mucus layer and unstirred water layer towards the enterocytes by mechanism of facilitated diffusion. On the other hand colloids can function as depots for poorly water soluble drugs. In the case of a low partition coefficient of drug from the colloid into the solution the concentration of free drug available for absorption can be reduced (Brouwers et al. 2006; Yano et al. 2010; Kleberg et al. 2010).

In parallel to the modification of transport media, the application of permeability assays has been extended to study the effect of pharmaceutical excipients on drug permeation through solubilization or modulation of tight junctions (Takahashi et al. 2002; Thanou et al. 2001). Beyond that, effects of drug delivery systems incorporating poorly water soluble drugs on drug permeability are increasingly studied (Linn et al. 2012; Buckley et al. 2012). Permeability studies on formulations like self emulsifying drug delivery systems (SEDDS) (Buyukozturk et al. 2010; Kataoka et al. 2012), liposomes (Parmentier et al. 2010), melt-extruded solid dispersions (Linn et al. 2012), cyclodextrines (Dahan et al. 2010) and mesoporous silica (Kaukonen et al. 2007; Mellaerts et al. 2008) have been published. Buch et al. (2009) performed permeability studies with fenofibrate formulated as a tablet based on a melt-extrudate and a tablet formulation based on a nanosuspension.
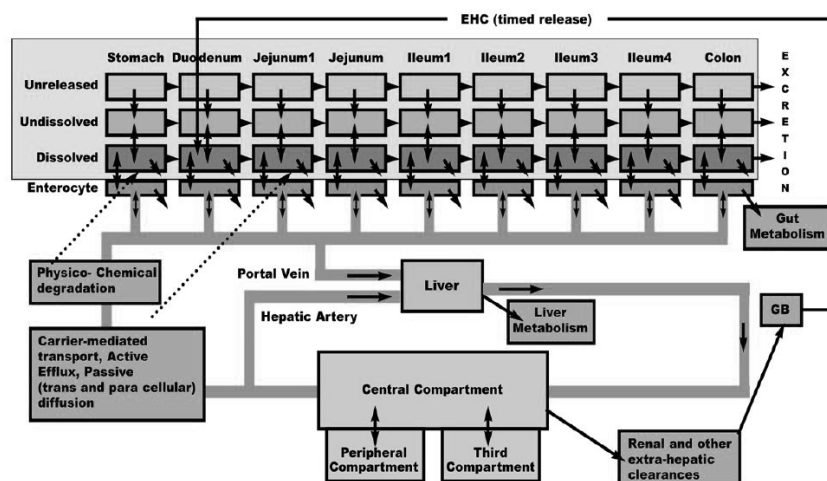
Figure 1.4: Advanced Compartmental Absorption and Transit (ACAT) model compartments (EHC: enterohepatic circulation, GB: gall bladder). Reproduced with permissions from Simulations Plus, Inc. (GastroPlus^{TM} 7.0 product manual).

1.2.3 Pharmacokinetic modeling & simulation

A mechanistic approach to mathematically model the oral absorption was developed based on the BCS and the physiology of the gastrointestinal tract. The model is known as the Compartmental Absorption and Transit (CAT) model (Yu et al. 1996a,b) and was further refined to form the Advanced CAT (ACAT) model. More physiochemical and physiological parameters as well as absorption in the stomach and colon are considered in the ACAT model. It describes the release, dissolution, luminal degradation, metabolism, and absorption of a drug as it transits through the GI tract. Nine GI compartments (stomach, seven segments of the small intestine, colon) and six states of drug component (unreleased, undissolved, dissolved, degraded, metabolized, absorbed) are distinguished (Fig. 1.4). The ACAT model was developed by Simulations Plus, Inc. and is available under the name GastroPlus^{TM}. Detailed model descriptions and case studies using the ACAT model in pharmaceutical research and development are available from Huang et al. (2009); Kesisoglou and Wu (2008); Mathias and Crison (2012), the GastroPlus^{TM} manual and others.

GastroPlus^{TM} offers the opportunity to adjust the saturation solubility of nanoparticles by the so called nanofactor effect. It was introduced to adjust the model to better simulate PK profiles of nanocrystal formulations. A need to modify the model for nano formulations was identified, since it was observed that faster dissolution and/or enhanced solubility alone were not sufficient to describe higher bioavailabilities. The nanofactor effect is based on the hypothesis that a local supersaturation at the apical membrane could occur when nano-sized particles are trapped between apical microvilli. The local supersaturation is given by the nanofactor effect, which specifies the extent by which drug can dissolve from different sized particles above the solubility limit. It is an empirical equation and requires the input of a user-defined, compound specific parameter, the nanofactor. The default equation with the default nanofactor (0.5) was calibrated to explain aprepitant PK profiles with particle sizes of 120 nm up to 5.5 μm (Wu et al. (2004), GastroPlus^{TM} manual).

(a) Rayleigh vs Mie scattering

(b) Rayleigh vs Mie scattering: Zoom
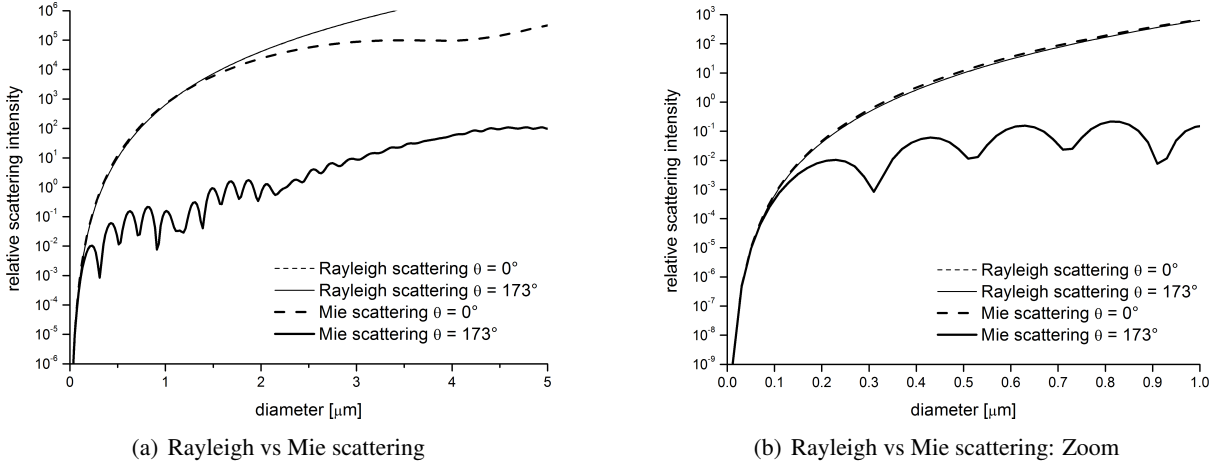
Figure 1.5: Relative scattering intensities vs particle diameter according to Rayleigh and Mie theory of light scattering. Calculated with MiePlot 4.2.03 (http://www.philiplaven.com/mieplot.htm). Input values: wavelength $\lambda_0 = 633$ nm, unpolarized light, refractive index of particle $n_{part} = 1.51$, imaginary refractive index of particle $n_{part,im} = 0$, refractive index of medium $n_{med} = 1.33$, different detection angles θ.

1.3 Light Scattering

The light scattering properties of a cloud of particles depend on particle size and number. The correlation between scattering intensity and particle number is linear for diluted samples, in which each particle scatters light independently without being influenced by proximate particles (van de Hulst 1957; Elsayed and Cevc 2011).

The dependence of scattering properties on particle size is more complex. Depending on the size range different theories describe the correlation between scattering intensity and particle size or detection angle. The Rayleigh theory describes the light scattering by spherical homogeneous particles smaller than the wavelength of incident light. In the case of an unpolarized light beam the scattering intensity I of light scattered by a single particle is given by

$$I = \frac{8\pi^4 a^6 n_{med}^6 I_0}{r^2 \lambda_0^4} \left| \frac{m^2 - 1}{m^2 + 2} \right|^2 (1 + cos^2\theta) \tag{1.6}$$

where I_0 is the intensity of incident monochromatic light with the wavelength λ_0, a is the radius, n_{med} is the refractive index of the medium surrounding the particle, r is the observation distance, m is the relative refractive index of the bulk particle material ($m = n_{part}/n_{med}$ with n_{part} being the refractive index of the particle), and θ is the angle between the detection direction and the forward direction of the incident light beam (Yguerabide and Yguerabide 1998).

Strictly spoken the Rayleigh theory applies to particles for which the radius is $a \ll \lambda_0/(2\pi n_{med}|m|)$, which is approximately $a \ll \lambda_0/10$. Equation 1.6 denotes that the scattered light intensity increases with the sixth power of the particle radius. Figure 1.5 shows the scattering intensity vs particle size graphs for two different detection angles θ. No differences can be observed between the detection angles 0° and 173°.

As an approximation isotropic light scattering into all directions can be assumed for small particles. The Mie theory describes the light scattering by spherical homogeneous particles of any size. Figure 1.5 illustrates that for an increasing particle size the scattering intensity does not continuously increase, but varies around a mean value with maxima and minima. More light is scattered into the forward direction ($\theta = 0°$) than into the backward direction ($\theta = 173°$) (Yguerabide and Yguerabide 1998).

1.4   Aim

The aim of this thesis was a biopharmaceutical characterization of oral nanoscopic formulations. As a nanoscopic formulation crystalline nanosuspensions – also referred to as nanocrystals – were selected, since the nanocrystal technology has proved to be one of the most promising and successful strategies for a bioavailability enhancement of poorly water soluble drugs. The biopharmaceutical characterization conducted in this study comprises solubility, dissolution, permeation and *in vivo* pharmacokinetic studies. Special emphasis was put on a quantification of the effects of particle size reduction on solubility, dissolution, permeation and bioavailability. The intention was to evaluate, whether an *in vitro-in vivo* correlation can be established.

The goals of this thesis were:

- Manufacturing and characterization of nanosuspensions and microsuspensions with various particle sizes and narrow particle size distributions.

- Determination of the solubility and dissolution kinetics of nanocrystals. Solubility and dissolution testing on nanocrystal formulations is challenging and reliable methods are rare. Especially for dissolution testing the pharmaceutical industries identified a need to evaluate and establish new techniques, which are *in vivo* predictive and/or can serve as quality control tools. The objective of this study was to develop an in situ noninvasive analytical method to measure dissolution and solubility. Different techniques were evaluated and the most promising one was a light scattering technique. A method based on the measurement of light scattering intensities for the determination of solid/dissolved fractions was tested, developed and applied to different samples.

- Evaluation of the best suitable experimental setup to measure drug substance permeability across Caco-2 monolayers, when nanocrystal formulations are employed.

- Design and realization of an *in vivo* pharmacokinetic study in rats.

- Analysis of particle size, solubility, dissolution, permeation and pharmacokinetic data with the focus on *in vitro-in vivo* relations.

- Testing of the predictivity of *in silico* modeling to simulate *in vivo* absorption and pharmacokinetics.

2

Materials and Methods

2.1 Materials

2.1.1 Model compounds

Fenofibrate (FF) and the Merck Serono compound AS (AS) were used as poorly water soluble model compounds. Table 2.1 lists their physicochemical properties. The chemical structures of fenofibrate and its metabolite fenofibric acid (FFA) are given in Figure 2.1.

Fenofibrate is the isopropyl ester prodrug of its active metabolite fenofibric acid (2-[4-(4-chloro-benzoyl) phenoxy]-2-methylpropanoic acid). Fenofibrate is a well known poorly water soluble model compound with a high permeability and is classified as a BCS II drug (Granero et al. 2005). Fibric acid derivatives (fibrates) are a class of compounds which play an important role in the management of hypercholesterolaemia, mixed dyslipidaemia, hypertriglyceridaemia and diabetic dyslipidemia. The lipid-modifying effects of fenofibrate are mostly mediated by its ability to activate peroxisome proliferator activated receptor α receptor (Steinhilber et al. 2007). After oral administration fenofibrate is rapidly converted
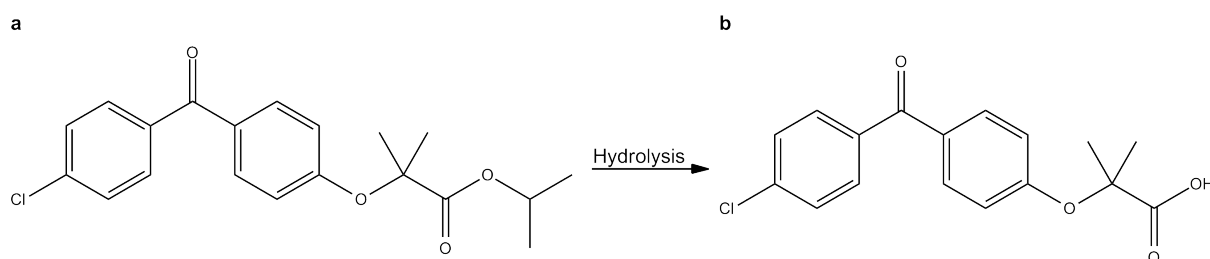
Figure 2.1: Chemical structures of fenofibrate (a) and its active metabolite fenofibric acid (b)

Table 2.1: Model compounds.

	Fenofibrate	Fenofibric acid	Compound AS
Molecular formula	$C_{20}H_{21}ClO_4$	$C_{17}H_{15}ClO_4$	
Molecular weight [g/mol]	360.8	318.8	
Physiocochemical properties			
Solubility in water [μg/ml]	< 0.3 [1]	70 [2]	< 10 [5]
log P	5.24 [3]	3.99 [2]	2.17 [4]
pKa	-	3.1 [2]	6.2 [4]
Melting point T_m [°C]	80 − 81 [3]	179 − 183 [2]	210 [4]
Density [g/cm^3]	1.18 ± 0.06 [5]	-	1.42 ± 0.10 [5]

    logP: octanol-water partition coefficient.

[1] Granero et al. (2005).

[2] Linn et al. (2012).

[3] Albinus (1993).

[4] Merck internal data.

[5] predicted by I-lab 2.0 software, ACD/labs, Toronto, Canada (ilab.acdlabs.com).

through hydrolysis of its ester bond to fenofibric acid. Hydrolysis is catalyzed by both tissue and plasma esterases and begins concomitantly with absorption. Only fenofibric acid and no unchanged fenofibrate can be detected in the blood after an oral dose (Keating and Croom 2007; Chapman 1987; Yun et al. 2006; Buch 2010).

The Merck Serono compound AS (AS) was synthesized in the laboratories of Merck Serono. It is a phosphoinositide 3-kinase-δ inhibitor intended for the treatment of rheumatoid arthritis (Rommel et al. 2007). It is no longer part of the Merck Serono development pipeline. Since it is, like fenofibrate, a poorly water soluble and highly permeable compound, it was selected for this study. The same stabilizers were applicable for the production of compound AS and fenofibrate micro- and nanosuspensions which offered a good comparability of the formulations.

2.1.2   Chemicals and reagents

Table 2.2 provides a list of various chemicals, reagents and drug products used in this work. All other chemicals were purchased from the usual commercial sources in highest available quality. Water was of Milli Q grade with 0.055 μS/cm, 5ppb TOC (Merck Millipore, Billerica, MA, USA).

2.1.3   Instruments and equipment

Tables 2.3 and 2.4 provide a list of the most important instruments used in this work. All other materials were standard laboratory equipment and were purchased from the usual commercial sources.

Table 2.2: Chemicals and reagents.

Name	Abbreviation	Quality / Product number	Supplier
fenofibrate	FF		Smruthi Organics Ltd, Solapur, India
fenofibric acid	FFA	Ph. Eur. grade	Laboratorio Chimico Internazionale S.p.a., Segrate, Italy
griseofulvin	GF		Sigma-Aldrich Co. LLC., St. Louis, MO, USA
ketoconazole	KC		Sigma-Aldrich Co. LLC., St. Louis, MO, USA
Lucifer Yellow CH dipotassium salt			Sigma-Aldrich Co. LLC., St. Louis, MO, USA
hydroxypropylmethylcellulose	HPMC		Pharmacoat® 603, Shin-Etsu Chemical Co., Ltd., Tokyo, Japan
dioctyl sulfosuccinate sodium salt	DOSS		MP Biomedicals LLC., Solon, OH, USA
acetonitril	AcN	LiChroSolv®, gradient grade	Merck KGaA, Darmstadt, Germany
trifluoroacetic acid	TFA	Uvasol®, spectroscpy grade	Merck KGaA, Darmstadt, Germany
polysorbate 80			Tween® 80, Sigma-Aldrich Co. LLC., St. Louis, MO, USA
SIF powder			Phares AG, Muttenz, Switzerland
EMEND® 80 mg capsule		PZN 2364367	MSD Sharp & Dohme Inc., Whitehouse Station, NJ, USA
Hanks´ balanced salts	HBSS	H4891	Sigma-Aldrich Co. LLC., St. Louis, MO, USA
Dulbecco´s phosphate buffered saline	PBS 10x	D1408	Sigma-Aldrich Co. LLC., St. Louis, MO, USA
Macrogol 15 hydroxystearate		Ph. Eur. grade	Solutol® HS 15, BASF SE, Ludwigshafen, Germany
Dulbecco´s modified Eagle´s medium	DMEM	FG0435	Biochrom AG, Berlin, Germany
Na-pyruvat 100 mM		L0473	Biochrom AG, Berlin, Germany
non-essential amino acids 100x		K0293	Biochrom AG, Berlin, Germany
L-glutamin 200 mM		K0283	Biochrom AG, Berlin, Germany
penicillin/streptomycin 10.000U/10.000µg/ml		A2212	Biochrom AG, Berlin, Germany
ciprofloxacin 2 mg/ml		PZN 3229861	Ciprobay® 200 mg infusion, Bayer Vital GmbH, Leverkusen, Germany
Gibco® TrypLE™ Express cell detachment		12605	Life Technologies corp., Carlsbad, CA, USA

Table 2.3: Instruments and equipment. Part 1.

Name	Description, Product number	Manufacturer
Wet media milling		
Dyno® Mill Research Lab	agitator ball mill	WAB, Muttenz, Switzerland
SiLibeads® ZY Premium 0.2-0.3mm	yttrium-stabilized zirconium oxide beads	Sigmund Lindner GmbH, Warmsteinbach, Germany
Milling beads 5mm	zirconium oxide balls	Fritsch GmbH, Idar-Oberstein, Germany
Grinding bowl	zirconium oxide bowl 12ml	Fritsch GmbH, Idar-Oberstein, Germany
IKA® rct basic stirrer	magnetic stirrer	IKA-Werke GmbH & CO.KG, Staufen, Germany
Stirring bar	20mm x 6mm	VWR International, LLC, Vienna, Austria
High pressure liquid chromatography		
Zorbax Eclipse Plus C18, 4.6 x 50mm, 3.5μm	reverse phase column # 959943-902	Agilent Technologies Inc., Santa Clara, CA, USA
Zorbax Eclipse Plus C18, 2.1 x 50mm, 3.5μm	reverse phase column # 959743-902	Agilent Technologies Inc., Santa Clara, CA, USA
Merck Hitachi LaChrom system	L-7100 pump, L-7360 column oven, L-7250 autosampler, L-7400 UV detector	Merck KGaA, Darmstadt, Germany
Dionex UltiMate® 3000 system		Dionex, Idstein, Germany
Particle size analytics		
Zetasizer Nano ZS™	Dynamic light scattering	Malvern Instruments Ltd, Worcestershire, UK
HORIBA LA-950	Static light scattering	Retsch Technology GmbH, Haan, Germany
Nanosphere™ Size Standards 3150A	polystyrene nanoparticle size standard 150nm	Thermo Fisher Scientific Inc., Waltham, MA, USA
polystyrene cuvettes with lids	disposable semi-micro cuvette	VWR International, LLC, Vienna, Austria
quartz glass cuvettes with lids	Hellma® Suprasil®, semi micro, 104B-QS	Hellma GmbH, Müllheim, Germany
optical glass cuvettes with lids	Hellma®, semi micro, 104-OS	Hellma GmbH, Müllheim, Germany
LEO 1530 Gemini	Scanning electron microscope	Carl Zeiss SMT GmbH, Oberkochen, Germany

Table 2.4: Instruments and equipment. Part 2.

Name	Description, Product number	Manufacturer
Cell culture and permeability assays		
75 cm² cell culture flask	430641	Corning Inc., NY, USA
12mm Transwell® insert with 0.4µm pore polyester membrane	3460	Corning Inc., NY, USA
12mm Snapwell™ insert with 0.4µm pore polyester membrane	3801	Corning Inc., NY, USA
vertical diffusion chamber system	Snapwell™ diffusion chambers, gas manifold, heater block	Harvard Apparatus, Holliston, MA, USA
Millicell®-ERS	chopstick device for TEER measurement	Merck Millipore, Billerica, MA, USA
cellZscope®	automated cell monitoring system	nanoAnalytics GmbH, Münster, Germany
Titramax 101	horizontal orbital shaker	Heidolph Instruments GmbH & Co.KG, Schwabach, Germany
Miscellaneous		
pH-meter 780		Metrohm AG, Herisau, Switzerland
DR201-95	Digital refractometery	A. Krüss Optotronic, Hamburg, Germany
Fluoroskan Ascent microplate fluorometer	Fluorescence spectroscopy	Thermo Fisher Scientific Inc., Waltham, MA, USA
Erweka DT80	Dissolution testing: USP II paddle apparatus	Erweka GmbH, Heusenstamm, Germany
DSC821e	Differential scanning calorimetry	Mettler-Toledo, Greifensee, Switzerland
Senterra Raman Microscope	Raman spectroscopy	Bruker Optics GmbH, Ettlingen, Germany
Oxford NMR 500MHz	Nuclear magnetic resonance spectroscopy	Oxford Instruments, Abingdon, UK
MicroCal VP-ITC microcalorimeter	Isothermal titration calorimetry	GE Healthcare, Buckinghamshire, UK
NanoSight LM20	Nanoparticle tracking analysis	NanoSight Ltd., Amesbury, UK
Heraeus Biofuge fresco	bench top centrifuge	Thermo Fisher Scientific Inc., Waltham, MA, USA
Whatman Anotop 10 0.1µm and 0.02µm	syringe filter	GE Healthcare, Buckinghamshire, UK
Whatman Spartan 30 0.45µm RC	syringe filter	GE Healthcare, Buckinghamshire, UK
Slide-A-Lyzer dialysis cassettes RC 10K MWCO, Volume 0.5 − 3 ml		Thermo Fisher Scientific Inc., Waltham, MA, USA
LASQCdiet® Rod16-A		LASvendi, Soest, Germany
Microvette® 200	blood collection tubes	Sarstedt AG & Co., Nümbrecht, Germany

2.2 Manufacturing of micro- and nanosuspensions

All formulations used in this study were aqueous suspensions of an API stabilized by HPMC (steric stabilizer) and DOSS (electrostatic stabilizer). They were composed of API / HPMC / DOSS at the ratio of 20 / 2.5 / 0.1 by total suspension weight, which corresponds to a API concentration of 200 mg/ml. The actual API concentration was determined for each formulation after manufacturing. Micro- and nanosuspensions were prepared by wet media milling. Prior to milling a slurry was prepared by dispersing the API in the aqueous stabilizer solution and homogenization by magnetic stirring. This slurry was used as a coarse suspension and was named raw nanosuspension (raw NS).

Two different kinds of milling equipment were used to enable the production of suspensions with different particle sizes. A high energy process was based on an agitator ball mill with yttrium-stabilized zirconium oxide beads ($0.2 - 0.3$ mm). By variation of the process parameters milling speed ($2000 / 3000 / 4000$ rpm), bead fill level ($50 / 70$ %) and process duration ($1 - 120$ min) distinct particle sizes could be generated. A low energy process was designed using a ball milling setup with zirconium oxide balls (5 mm) agitated in a 12 ml zirconium oxide grinding bowl by magnetic stirring. With the low energy process and with process durations of only 1 min suspensions of wide particle size distributions were obtained and further steps were performed to create suspensions of defined size with narrow size distribution. The post milling processes covered sedimentation, centrifugation and isolation of different supernatant/sediment layers. For example, microparticles were separated off by sedimentation and sampling of the topmost supernatant layer. On the contrary for the production of bigger sized suspensions the supernated was discarded and the sediment was redispersed in water. The manufacturing details for all suspensions are summarized in Table 2.5. All formulations were stored at $4 - 8°$C.

2.3 Physical state characterization

2.3.1 Differential scanning calorimetry

By differential scanning calorimetry (DSC) the physical state of drug substances and formulations was characterized. DSC measurements were conducted with a DSC821e instrument (Tab. 2.4). 10 ± 1 mg of drug substances were weighted into $100 \, \mu$l aluminum pans and the pans were sealed with a perforated lid. In the case of micro- and nanosuspensions the weighted crucibles were filled with approximately $100 \, \mu$l of suspension and the water was allowed to completely evaporate at room temperature (approximately 72 h). Depending on the suspension concentration this process was repeated to yield a total amount of solids of 10 ± 1 mg. Thermograms showing the heat flux versus temperature with endothermic reactions displayed in positive direction were recorded with following method: Heating from $25 - 250°$C at a rate of 10 K/min. From the thermograms the enthalpies of transition ΔH [J/g] were calculated via peak integration with StarSoftware (Mettler-Toledo, Greifensee, Switzerland). For each sample three repetitions were made.

Table 2.5: Manufacturing of suspensions.

Formulation	Milling equipment	Batch size [ml]	Bead fill level	Speed [rpm]	Milling time	Post milling processing
Fenofibrate suspensions						
NS 120nm	DM	100	70 %	4000	120 min	
NS 140nm	DM	100	50 %	2000	120 min	
NS 160nm	DM	100	50 %	2000	50 min	
NS 180nm	DM	100	70 %	4000	1 min	[1]
NS 270nm	DM	100	70 %	4000	1 min	[1]
NS 650nm	DM	100	50 %	2000	15 min	
NS 800nm	LE	4	10 pcs	250	18 h	[2]
NS 1070nm	LE	4	10 pcs	250	17 h	[2]
MS 7.9μm	LE	4	10 pcs	250	3.5 h	[3]
Compound AS suspensions						
NS 100nm	DM	100	70 %	2000	40 min	
NS 130nm	LE	4	10 pcs	500	4 h	[4]
NS 150nm	LE	4	10 pcs	500	5 h	[4]
NS 860nm	LE	4	10 pcs	250	26 h	[5]
NS 1020nm	LE	4	10 pcs	250	24 h	[5]
NS 1320nm	LE	4	10 pcs	50	5 h	[5]
MS 3.4μm	LE	4	10 pcs	250	22 h	[6]
MS 6.8μm	LE	4	10 pcs	250	3 h	

DM: agitator ball mill Dyno® Mill ResearchLab. LE: low energy ball milling by magnetic stirring. pcs: pieces.

[1] 4 weeks sedimentation - sampling of supernatant layers
[2] 72 h sedimentation - sampling of supernatant layers
[3] 72 h sedimentation - discard of supernatant layers
[4] 3-5 days sedimentation - supernatant centrifugation - supernatant sampling
[5] 3-5 days sedimentation - supernatant centrifugation - sediment redispersion
[6] 72 h sedimentation - sediment redispersion

2.4   Light scattering measurements

A Zetasizer instrument with Zetasizer software 6.20 (Tab. 2.3) was used for various purposes. The instrument and software are designed to perform dynamic light scattering (DLS) measurements for the determination of particle sizes (section 2.5.1). For this purpose light scattering intensity fluctuations are recorded and analyzed (Brittain 2003). In addition the instrument was used to measure absolute light scattering intensities, which can be read out as mean count rate in kilo counts per second (kcps). The mean count rate gives the arithmetic mean of the scattering signal (count rate) detected during a measurement run. The number and duration of measurement runs can be varied in the measurement settings. The Zetasizer instrument was equipped with a He-Ne laser (wavelength 633 nm, 4.0 mW) and an avalanche photodiode served as a detector at a detection angle of 173° (backscatter mode). In the measurement settings the attenuator and the measurement position can be varied. Since both have an influence on the intensity of scattered light it is crucial to keep them constant, when it is intended to compare absolute scattering intensities of different measurements. The incident laser light is varied by the attenuator, which can be set from 0 (total laser block) to 11 (full laser power). In this study a fixed attenuator of 10 (30 % of laser light enters the sample cuvette, data provided by Malvern) was used for all determinations of absolute light scattering intensities. The measurement position was fixed at 4.65 mm (distance from cuvette wall) to ensure a constant scattering volume. The scattering volume is the area of the laser beam crossing the detection window and has a volume in the order of magnitude of $0.01\,\mu$l (data supplied by Malvern). Both, attenuator and position settings, were chosen to give scattering intensity values in the range of $100 - 2000$ kcps. All measurements were performed at $25\,°$C in disposable semi-micro polystyrene cuvettes with lids (Tab. 2.3).

2.4.1   Validation

It was validated that the laser and detector of the Zetasizer instrument function in a constant and linear mode for the considered scattering intensities, since the instrument is calibrated for measurement and analysis of intensity fluctuations, but not for recording absolute intensity data. For that purpose the correlation between particle concentration and scattering intensity of spherical polystyrene nanoparticles (Nanosphere[TM] Size Standards 3150A, Z average 147 ± 3 nm, Tab. 2.3) was evaluated. The particle suspension with a concentration of 1% solids (data provided by Thermo Scientific) was diluted in 0.06% sodium chloride solution according to the dilution protocol for calibration (protocol provided by Malvern). Dilutions of $0.01 - 0.22 * 10^{-3}$ % solids were prepared and immediately the absolute scattering intensities were determined (Three measurements with 10 runs at 10 s on three independently prepared samples).

Furthermore the correlation of scattering intensity and particle concentration was explored for the FF suspension NS 1070nm. Seven different dilutions in water were prepared with FF concentrations ranging from $0 - 5.5\,\mu$g/ml. The solubility was exceeded at least twofold in the prepared samples and stability of particle size throughout the measurement was assured. (Three measurements with 10 runs at 10 s on three independently prepared samples).

2.5   Determination of particle size and morphology

2.5.1   Dynamic light scattering

Dynamic light scattering (DLS) measurements were conducted for the determination of submicron particle sizes using a Zetasizer instrument. Nanosuspensions were diluted with water to concentrations of typically $20-200\,\mu g/ml$. At these concentrations the drug substance solubility is exceeded by at least factor twenty, which prevents particle dissolution and ensures stable particle size. The effect of nanosuspension ingredients on the dispersion medium viscosity could be neglected due to the high dilutions (HPMC concentration $< 0.0025\,\%$). Threefold size measurements at position $4.65\,mm$ with automated attenuator settings at $25\,°C$ were performed. Micelle size in the dissolution media was determined likewise. Particle size is reported as intensity weighted mean hydrodynamic size (Z average) and the polydispersity index (PDI) provides a measure of distribution width.

2.5.2   Static light scattering

Static light scattering (SLS) measurements were performed using a Horiba LA-950 instrument for the determination of particle sizes. The concentration of nanosuspensions used was adjusted to meet the optimum condition of 80 - $90\,\%$ transmission for the red laser and a 70 - $90\,\%$ transmission for the blue laser. In the software settings the refractive indices of FF and AS were set to 1.51 and 1.60 respectively. The refractive indices of APIs were determined by refractive index measurements of API solutions in ethanol and extrapolation to $0\,\%$ solvent (Saveyn et al. 2002).
Size distributions measured by SLS are reported on a volume fraction basis calculated by using 15 iterations. A minimum of three repetitions was performed for each size determination.

2.5.3   Scanning electron microscopy

Scanning electron microscope (SEM) images were taken to gain insight into the morphology of suspension particles. A few microliters of suspension were put onto a glass specimen holder and were dried at room temperature. Subsequently an ultrathin coating of the specimen was applied by depositing $10\,nm$ of platinum on the sample by low-vacuum sputter coating. SEM images were taken with a LEO 1530 Gemini instrument (Tab. 2.3). The instrument was equipped with a field emission gun, which was used at acceleration voltage $5\,kV$, and detection was conducted with an inlens detector.

2.6   Concentration determination

2.6.1   Fluorescence spectroscopy

Fluorometric quantification of the fluorescent dye Lucifer Yellow was conducted with a Fluoroscan Ascent microplate reader in 96-well plates (Tab. 2.4). Extinction and emission wavelengths were $485\,nm$ and $538\,nm$. A calibration with a minimum of six data points covering the measurement range was repeated with every series of fluorescence measurements. A calibration was accepted as valid, if it resulted

Table 2.6: Methods for high pressure liquid chromatography (HPLC).

	Fenofibrate and fenofibric acid[1]	Compound AS
Mobile phase		
Eluent A	H_2O/AcN: 95/5 + 0.01% TFA	H_2O/AcN: 95/5 + 0.1% TFA
Eluent B	H_2O/AcN: 5/95 + 0.01% TFA	H_2O/AcN: 5/95 + 0.1% TFA
Extraction medium	H_2O/AcN: 20/80	H_2O/AcN: 20/80
Column	Zorbax Eclipse Plus C18 4.6 x 50mm 3.5μm	Zorbax Eclipse Plus C18 2.1 x 50mm 3.5μm
Column temperature	30 °C	50 °C
Flow	2 ml/min	1.8 ml/min
Gradient	0 min A/B 100/0 3 min A/B 80/20 6.8 min A/B 30/70 8.3 min A/B 0/100 11 min A/B 0/100 12 min A/B 100/0	0 min A/B 100/0 3 min A/B 75/25 6 min A/B 70/30 10 min A/B 20/80 10.1 min A/B 0/100 12 min A/B 0/100 12.1 min A/B 100/0 14 min A/B 100/0
Injection volume	20 μl	10 μl
Sample temperature	20 °C	10 °C
Detection wavelength	288 nm[1]	268 nm

[1] Ketoconazole and griseofulvin were determined with the same method, however, with other detection wavelengths: 210 nm (KC) and 293 nm (GF).

in coefficients of determination $R^2 > 0.995$.

2.6.2 High pressure liquid chromatography

Fenofibrate, fenofibric acid, compound AS, ketoconazole (KC) and griseofulvin (GF) concentrations were determined by high performance liquid chromatography (HPLC). Two different HPLC systems (Merck Hitachi LaChrom and Dionex 3000, Tab. 2.3) were used and the detailed methods can be found in Table 2.6. All samples were diluted in HPLC vials with the extraction medium 1:1. Three independant dilutions of each sample were prepared and two injections were performed from each vial. A complete calibration of the method was repeated every three months and control standards were run with each sequence. Calibration standards were prepared in extraction medium at concentrations of $1 - 100\,\mu$g/ml.

2.6.3 Plasma extraction

To determine concentrations of fenofibric acid in rat plasma samples it was necessary to extract the API from the plasma by a protein precipitation protocol. Plasma samples were thawed at room temperature, homogenized via vortexing, and centrifuged to separate off the cryoprecipitate. 100 μl of plasma

were then transfered to a 1.5 ml micro tube, acidified with $20\,\mu$l of 1 M hydrochloric acid, and vortexed. The protein precipitation step was carried out by adding $380\,\mu$l of ice cold acetonitrile, vortexing and subsequent storage of samples for 10 min at room temperature. Via centrifugation the precipitate was separated off and the supernatant was quantitatively transfered to a clean tube. Under vacuum the samples were evaporated to dryness (approximately 20 h). The residue was reconstituted in $200\,\mu$l mobile phase eluent B (H_2O / AcN: 5 / 95 + 0.01 % TFA). Therefore the sealed tubes were put into a ultrasonic bath for 10 min. In most samples a small undissolvable fraction remained and was centrifuged off. The clear supernatant was transfered into a HPLC vial with micro volume insert ($250\,\mu$l, pulled point glass inserts) and HPLC analysis was performed using the standard protocol for fenofibric acid quantification (Tab. 2.6). All centrifugation steps were carried out at 15700 g for $5-10$ min.

2.7 Solubility

2.7.1 Drug substance solubility

An excess amount of API (10 mg/ml) was dispersed in the test medium and stirred for 24 h at $25 \pm 1°$C. To separate off undissolved material samples were centrifuged at 16060 g for 30 min and subsequently the supernatant was filtered (Whatman Anotop 10 $0.1\,\mu$m). Control DLS measurements were performed on the filtrates and absence of undissolved material was assumed if no particles apart from polysorbate micelles could be detected. The concentration of dissolved drug was quantified by HPLC. Three independent experimental series with triplicates were performed.

2.7.2 Nanosuspension solubility by light scattering method

To determine the solubility of nanosuspensions an approach of monitoring the presence of solid nanoparticles by light scattering (instead of determining concentrations of dissolved material) was introduced by Lindfors et al. (2006) and taken up by Van Eerdenbrugh et al. (2010). In the presented study this method was modified and a Zetasizer instrument was used to measure the scattering intensity.
At the time zero nanosuspension dilutions of $0-14\,\mu$g/ml (FF) and $0-9.5\,\mu$g/ml (AS) in the test medium were prepared and stored in sealed cuvettes at $25 \pm 1°$C. At distinct time points the samples were homogenized via shaking and absolute scattering intensities were measured (section 2.4, settings: one measurement with 8 runs at 8 s). The resulting data were plotted in a scattering intensity vs concentration graph and two linear segments could be identified: The first one represents completely dissolved concentrations with scattering intensities equal to blank medium and the second one represents partially dissolved concentrations with a slope corresponding to an increasing solid fraction. To a minimum of seven data points of each branch a linear function was fitted. Their intersection point was calculated and interpreted as the nanosuspension solubility. For all dilutions the concentration of the nanosuspension excipient DOSS was below the critical micelle concentration of 1.2 mg/ml (Chatterjee et al. 2001) and hence it was avoided that solubilization influences solubility. Each experiment was performed in triplicate.

Table 2.7: Dissolution media.

Simulated gastric fluid supplemented with 0.1% Tween 80 (SGF + Tween)		
NaCl	2.00 g	34.2 mM
HCl 1N	80 ml	
Tween 80	0.94 ml	0.76 mM
Milli Q water	ad 1000 ml	
pH	adjusted to 1.2 ± 0.05	
Fasted state simulated intestinal fluid (FaSSIF)		
NaCl	6.19 g	106 mM
NaOH	0.42 g	34.2 mM
NaH_2PO_4	3.44 g	28.7 mM
sodium taurocholate[*]		3.00 mM
lecithin[*]		0.75 mM
Milli Q water	ad 1000 ml	
pH	adjusted to 6.5 ± 0.05	

[*] contained in 2.24 g SIF powder

2.8 Dissolution

2.8.1 Dissolution media

Two kinds of dissolution media were used: Simulated gastric fluid (SGF) without pepsin according to United States Pharmacopeia (USP34-NF29 S1) supplemented with 0.1% (w/V) polysorbate 80 (Tween® 80) and fasted state simulated intestinal fluid (FaSSIF). The use of the compendial medium SGF is widespread and a supplementation with surfactants is often done in dissolution testing of poorly water soluble drugs (Lee et al. 2008). The use of biorelevant media like FaSSIF has emerged in the last decade and it has nowadays developed to a standard medium in pharmaceutical dissolutin testing, especially if an *in vitro-in vivo* correlation is intented (Galia et al. 1998; Lee et al. 2008). FaSSIF was prepared with SIF powder (Tab. 2.2) according the protocol provided by Phares. The compositions of dissolution media are given in Table 2.7. SGF + Tween was stored at $4 - 8°C$ and used within seven days. FaSSIF prepared from SIF powder is stable for two days at room temperature (data provided by Phares). The refractive indices of dissolution media were determined with a digital refractometer (Tab. 2.4).

2.8.2 Conventional method: Sampling and separation

Conventional dissolution tests were performed with a USP II paddle apparatus at 25 ± 1°C at 100 rpm rotation speed and a medium volume of 500 ml. After 2.5 min, 5 min, 10 min, 15 min, 20 min, 30 min, 45 min, 60 min, 90 min and 120 min 1 ml samples were withdrawn and filtered (Whatman Anotop 10 0.02μm). The first 0.5 ml of filtrate was discarded. The filtrate was analyzed for undissolved material by a DLS measurement. Absence of drug crystals was assumed if no particles apart from polysorbate 80 micelles could be detected. Shorter sampling intervals (0.3, 0.7, 1.0, 1.3, 1.7, 2.0, 2.3, 2.7, 5.0 min) were chosen for the dissolution experiment with a nanosuspension.

Concentrations of the filtrates were determined by HPLC and represent the dissolved concentration. The undissolved fraction was calculated by subtraction of the dissolved concentration from the total drug concentration. The fraction dissolved was calculated as percentage of dissolved concentration of total API concentration.

2.8.3 Dialysis method: Continuous separation

The conventional sampling and separation experiment was modified by using a dialysis setup. A nanosuspension was injected into a dialysis cassette floating in the dissolution medium in a paddle apparatus dissolution vessel. The idea was that dissolved API will diffuse across the dialysis membrane whereas nanoparticles will be retained in the dialysis cassette. Slide-A-Lyzer dialysis cassettes with a molecular weight cut off of 10kD were used and filled with 3 ml of prediluted formulations ($207\,\mu$g/ml). A fenofibrate nanosuspension (NS 120nm) was compared to a coarse suspension (raw NS, section 2.2). The dissolution medium was SGF + Tween. The dissolution vessels were filled with 900 ml and the rotation speed was 100 rpm. The experiment was performed at 37 °C. $100\,\mu$l samples were withdrawn through the injection ports of the dialysis cassettes (donor compartment) with a Hamilton microsyringe.
Concentrations of fenofibrate in the donor samples were determined by HPLC. The concentrations in the receiver compartment were calculated by subtracting the donor concentrations from the total API concentration.

2.8.4 Noninvasive analytical techniques

The feasibility of noninvasive analytical techniques for the purpose of nanocrystal dissolution monitoring was evaluated. The focus was set on a noninvasive light scattering technique which will be described in a separate section (section 2.9).

Nuclear magnetic resonance spectroscopy and Raman spectroscopy

The idea to use spectroscopic techniques was to follow the transition of physical state of an API molecule during dissolution. The API concentrations employed in nanocrystal dissolution experiments are in the lower μg/ml range, due to poor solubility of APIs. Consequently the sensitivity of the analytical technique to detect and quantify the API was the critical point about the applicability of spectroscopic techniques. Since nanocrystal dissolution experiments were conducted at concentrations below the saturation solubility, a saturated solution displayed the maximal relevant API concentration. The sensitivity of spectroscopic techniques was evaluated by measurement of a saturated API solution. Saturated solution of fenofibrate in SGF + Tween were prepared like described in section 2.7.1.
For the evaluation of nuclear magnetic resonance spectroscopy (NMR), the medium was prepared with DCl and D_2O. NMR measurements with respect to ^{1}H nuclei (Proton NMR) were performed with a Oxford NMR instrument (Tab. 2.4). Raman spectra of a saturated solution were recorded with a Raman microscope at a laser wavelength of 532 nm (Tab. 2.4).

Nanoparticle tracking analysis

Nanoparticle tracking analysis (NTA) is a technique combining laser light scattering microscopy with a charge-coupled device (CCD) camera which enables the visualization and recording of nanoparticles in solution. Individual particles can be tracked by the software. Their particle size is calculated from the particle movement by applying the Stokes-Einstein equation (Filipe et al. 2010). The size and scattering intensity of particles can be determined simultaneously on a particle-by-particle basis. In addition the particles are counted.

Feasibility studies were carried out with a fenofibrate nanosuspension NS 140nm, which was diluted with SGF + Tween to concentrations of $5-20\,\mu$g/ml. Immediately after dilution a NTA video was recorded and sequentially analyzed in steps of $15-60$ s to follow the process of particle dissolution. Measurements were performed with a NanoSight LM20 instrument and analyzed with NTA 2.0 Analytical Software (Tab. 2.4).

Isothermal titration calorimetry

Isothermal titration calorimetry (ITC) is a thermodynamic method and measures the heat released or absorbed during various interactions or reactions. Calorimetric effects are associated with particle dissolution and it was evaluated, if this effect was measurable for nanocrystal dissolution with a VP-ITC instrument (Tab. 2.4). The sample cell was filled with 1.4 ml of SGF + Tween and the system temperature was set to 25°C. The fenofibrate nanosuspension NS 140nm was diluted with SGF + Tween (1:1000) and was stepwise injected into the sample cell with an injection speed of 0.5 ml/s. As a negative control sample an aqueous solution of the nanosuspension stabilizers HPMC and DOSS was prepared at equal concentrations as in the nanosuspension (2.5 % HPMC, 0.1 % DOSS). This solution was likewise diluted and injected into the sample cell.

2.9   Dissolution by light scattering

Nanocrystal dissolution was followed by monitoring changes of light scattering intensity with a Zetasizer instrument (section 2.4). The method will be described in the following and Figure 2.2 provides an overview of experimental setup and data evaluation method.

2.9.1   Experimental setup

The dissolution experiments were conducted at concentrations below the nanosuspension solubility after 24 h ($S_{NS\,24h}$) and nanosuspensions were diluted with the test medium in two steps. In the predilution step $1-10\,\mu$l of nanosuspension were added to $5-10$ ml of medium under magnetic stirring to a concentration $8-10$ fold above the solubility $S_{NS\,24h}$. Within 30 s the final dilution step was performed directly in the cuvette by adding $20-100\,\mu$l of prediluted nanosuspension to a total volume of 1 ml and this time was defined as zero. Gentle mixing was performed by four 180°-turnings of the cuvette taking care of no air bubbles to occur. A series of measurements was started subsequent to placing the cuvette in the sample cell. Measurement parameters were: 2 runs at 2 s, measurement position 4.65 mm, attenuator 10 and

Materials	Dilution	Quantification
Nanosuspension 20% Fenofibrate (BCS II) 0.1% DOSS 2.5% HPMC	Predilution: $C \gg C_S$	**Zetasizer Nano™** series of measurements $\rightarrow$ scattering intensity recorded continuously
+		**Laser** **Detector** $173°$
Medium Simulated Gastric Fluid (pH 1.2) + 0.1% Tween 80	Final dilution $C < C_S$ cuvette Mix	

Dissolution graph	Data Evaluation

Model fitting: (bi-)exponential functions

$$f(t) = M * e^{(-t/c)} + y_0$$

$$f(t) = M_1 * e^{(-t/c_1)} + M_2 * e^{(-t/c_2)} + y_0$$

First data point:
25s

Measurement duration:
10s

Calculation of dissolution time (DT)

$$f(DT) = 0.01 * M$$
$$f(DT) = 0.01 * (M_1 + M_2)$$

1% of initial scattering intensity is reached

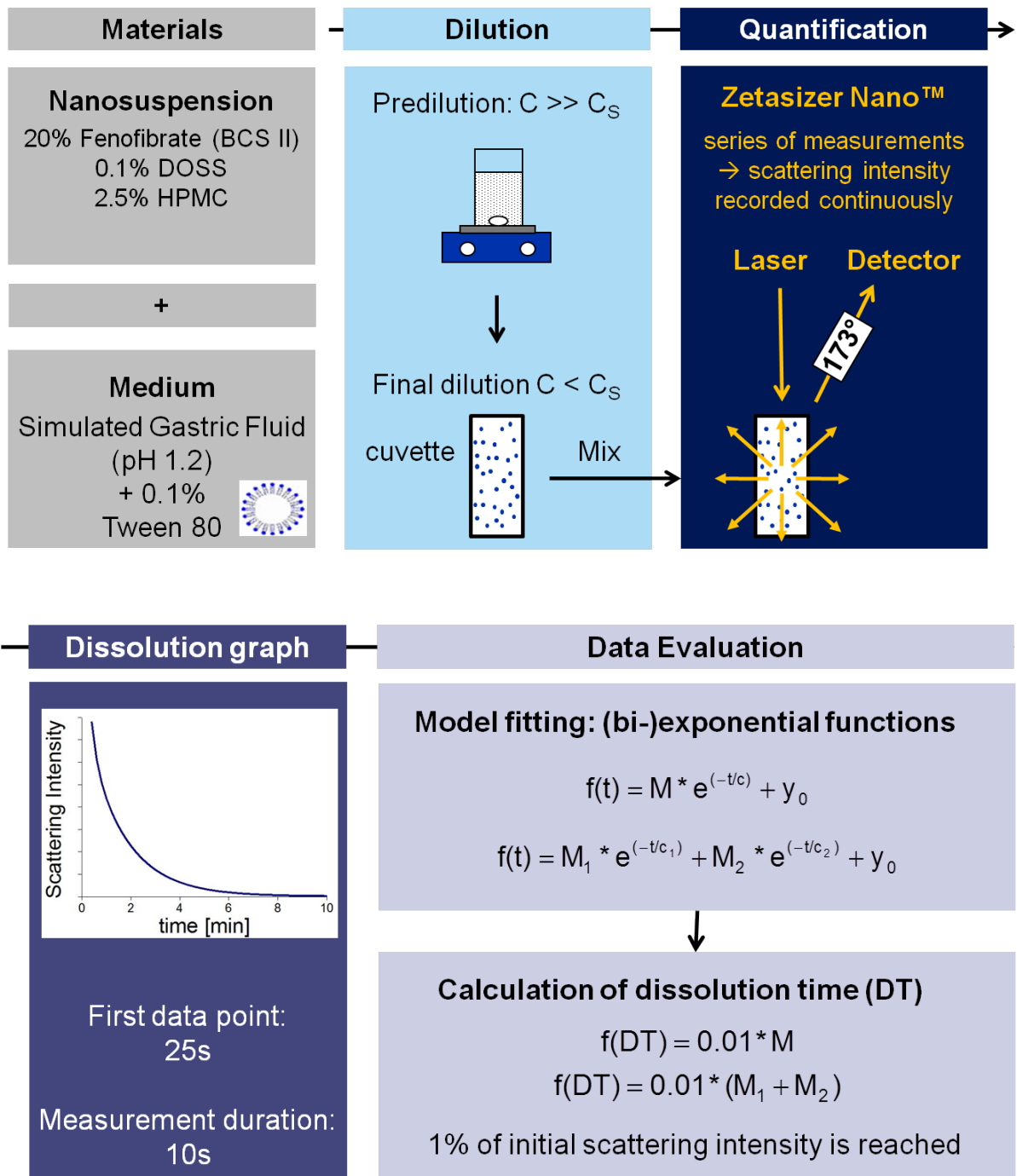Figure 2.2: Nanocrystal dissolution by light scattering: Schematic representation of experimental setup (upper panel), resulting dissolution graph and data evaluation method (lower panel). C is the concentration and C_S is the saturation solubility. $f(t)$ is the scattering intensity, t is the time after dilution and M, c and y_0 are the unknown function parameters. DT is the dissolution time.

25°C. Before each dissolution experiment a blank medium measurement was conducted in the identical cuvette already containing the respective volume of medium for the final dilution step. The final result is reported as Δ Mean Count Rate, which is the mean count rate of each dissolution measurement reduced by the mean count rate of the blank measurement.

2.9.2   Method development

In light scattering dissolution experiments a decreasing scattering intensity signal was observed, which might not only be due to particle dissolution but also due to particle adsorption onto cuvette walls. The extent of API adsorption, the influence of cuvette material and fluid flow were evaluated.

Adsorption

To evaluate the extent of adsorption API recovery studies were performed. The fenofibrate nanosuspension NS 120nm was used as a model formulation. It was dispersed in two different media (SGF + Tween and FaSSIF) at two concentration levels ($5\,\mu$g/ml and $10\,\mu$g/ml) in two different cuvette types (polystyrene disposable cuvettes (PS) and quartz glass cuvettes (QS), Tab. 2.3). After 1, 5 and 10 min samples were withdrawn and subjected to HPLC concentration determination.

Cuvettes

To evaluate the effect of cuvette material dissolution experiments with NS 120nm at a concentration of $5.5\,\mu$g/ml in SGF + Tween or FaSSIF were performed in three different cuvette types: polystyrene disposable (PS), quartz glass (QS) and optical glass (OS) cuvettes (Tab. 2.3). PS and QS cuvettes were used in two different conditions: (1) after thorough cleaning and drying and (2) reuse after a dissolution experiment (the cuvette was emptied after the first experiment and reused as is for a second identical experiment). The idea of the reuse experiments was to evaluate possible adsorption effects. If adsorption of particles or API onto cuvette walls influenced dissolution relevantly, it would be expected that an influence on dissolution profiles in reused cuvettes would be seen, since cuvette wall surfaces would already be coated during the first experiment.

Fluid flow

To evaluate whether the mixing step of the dissolution experiments and the resulting fluid flow in the sample effects the measured light scattering signal, a rested sample was compared to a just mixed sample. For that purpose spherical polystyrene nanoparticles (Nanosphere[TM] Size Standards 3150A, Z average 147±3 nm, Tab. 2.3) were dispersed in SGF + Tween at a concentration of $0.5 * 10^{-3}\,\%$ solids. For the mixed sample the time flow and mixing procedure of a dissolution experiment was followed. For the rested sample a resting step of 10 min was included between mixing and starting the measurement. A series of 15 measurements was performed with the parameters: measurement position 4.65 mm and attenuator 6, 10 runs at 10 s.

2.9.3 Data evaluation

Exponential models were chosen to describe the dissolution curves in an empirical and pragmatic way and to enable the calculation of characteristic data points to improve the comparability of different dissolution profiles. Selection of functions for data fitting was governed by the intention of introducing only a low level of complexity. Exponential (Eq. 2.1) and biexponential (Eq. 2.2) functions have been described to model dissolution data previously (Costa and Sousa Lobo 2001; Langguth et al. 2004; Laakso et al. 1984). Especially biexponential models have been successfully fitted to dissolution profiles of micron and submicron particle size distributions (Tsinman et al. 2009; Galli 2006; Tinke et al. 2005; Tay et al. 2011). In this study simple exponential function fitting was not sufficient in all cases so that biexponential function fitting was applied for all tests.

$$f(t) = Me^{-t/c} + y_0 \tag{2.1}$$

$$f(t) = M_1 e^{-t/c_1} + M_2 e^{-t/c_2} + y_0 \tag{2.2}$$

$f(t)$ is the scattering intensity (Δ Mean Count Rate) in kcps, t is the time after dilution in minutes and M, c and y_0 are the unknown function parameters. To compare the goodness of fit for both models not the coefficient of determination R^2, but the adjusted coefficient of determination $R^2_{adjusted}$ was used. $R^2_{adjusted}$ is more meaningful, when comparing models with different numbers of parameters (Costa and Sousa Lobo 2001) and is calculated as

$$R^2_{adjusted} = 1 - \frac{(n-1)}{(n-p)}(1 - R^2) \tag{2.3}$$

where n is the number of dissolution data points and p is the number of parameters in the model. The fitted functions were further analyzed by calculating the time, when only 1% of the initial scattering intensity (fitted parameter M or $M_1 + M_2$) remains. This time is defined as the total dissolution time DT. For exponential and biexponential functions DT was calculated according to Eq. 2.4 and Eq. 2.5 respectively.

$$f(DT) = 0.01M \tag{2.4}$$

$$f(DT) = 0.01(M_1 + M_2) \tag{2.5}$$

By applying these equations the function offset y_0 was neglected. This was possible, since y_0 was very small compared to M or $M_1 + M_2$, respectively ($< 10\,\text{kcps}$). The function fitting and determination of DT was performed for each repetition of a dissolution experiment. Subsequently arithmetic means and standard deviations of DT were calculated.

2.9.4 Application to a market drug product

EMEND® 80 mg capsule (Tab. 2.2) is a market product of the API aprepitant based on nanocrystals. The feasibility of the light scattering dissolution method to monitor dissolution of aprepitant nanocrystals released from EMEND® was tested. Since the formulation contains undissolvable excipients which disturb light scattering measurements, a filtration step was added to the dissolution protocol.

The total number of pellets contained in a single EMEND® capsule and individual pellet weight was determined. This allowed the calculation of API content of single pellets. Pellets were then dispersed in SGF + Tween by magnetic stirring. By this process nanocrsystals were released from the pellets and their dissolution was prevented by choice of a concentration above the aprepitant solubility. In the predilution step (Fig. 2.2) undissolvable excipients were removed by filtration through a $0.45\,\mu$m filter (Spartan 30, Whatman). The particle size of the filtrate was measured. The final dilution step and the light scattering measurement were carried out according to the standard protocol (section 2.9.1). The experiment was performed at 37°C.

2.10 In vitro permeability studies

2.10.1 Cell culture

Caco-2 cells (DSMZ no. ACC 169) were supplied by Leibniz-Institut DSMZ - Deutsche Sammlung von Mikroorganismen und Zellkulturen GmbH, Braunschweig, Germany. The cells were grown in cell culture flasks in Dulbecco´s modified Eagle´s medium (DMEM) with supplements (Tab 2.8). The cells were kept at $37\,°$C in an atmosphere with 5% CO_2 and in equilibrium with distilled water. The medium was changed every other day. The cells were subcultured at 80% confluency. Therefore the feeding medium was removed, the cells were washed with HBSS^{--}, and TrypLE^{TM} Express was used to detach the cells. Cells were used in the experiments at passage number $17-38$.

For the permeability studies the Caco-2 cells were seeded on permeable filter supports (Tab. 2.4) at a density of $65000\,$cells/cm^2. No additional coating of the filter supports was required. The cells were grown in feeding medium with 1.5 ml on the basolateral and 0.5 ml on the apical side. Every other day the medium was exchanged by performing the following steps: removing apical medium, removing basolateral medium, adding basolateral medium, adding apical medium. After 21 ± 7 days the cells formed a confluent monolayer (verified microscopically) and were ready to be used in permeability experiments.

2.10.2 Transport media for permeability studies

Hank´s balances salt solution (Hanks and Wallace 1949) supplemented with bivalent cations of magnesium and calcium (HBSS^{++}) was used as transport medium. The pH was adjusted to 6.5 ± 0.05 for the apical medium and to 7.4 ± 0.05 for the basolateral medium. HBSS^{++} was prepared on the basis of premixed salts (Tab. 2.2). In the apical compartment as alternative medium transport-FaSSIF (tFaSSIF) was used, which was composed of HBSS^{++} with addition of sodium taurocholate and lecithin. SIF powder was used for preparation (Tab. 2.2). Table 2.9 provides the compositions of all transport media.

Table 2.8: Cell culture media and buffers

Feeding media: Dulbecco´s modified Eagle´s medium (DMEM) with supplements		
fetal bovine serum	10 % (V/V)	
Na-pyruvat 100 mM	1 % (V/V)	
non-essential amino acids 100x	1 % (V/V)	
L-glutamin 200 mM	1 % (V/V)	
pencicillin	100 U	
streptomycin	100 μg/ml	
ciprofloxacin	20 μg/ml	
Hanks´ balanced salt solution (HBSS^{--})		
KCl	0.4 g	5.37 mM
KH$_2$PO$_4$	0.4 g	0.44 mM
NaCl	8.0 g	137 mM
Na$_2$HPO$_4$	0.048 g	3.38 mM
NaHCO$_3$	0.35 g	4.16 mM
Milli Q water	ad 1000 ml	

Table 2.9: Transport media.

Hanks´ balanced salt solution (HBSS^{++})		
KCl	0.4 g	5.37 mM
KH$_2$PO$_4$	0.4 g	0.44 mM
NaCl	8.0 g	137 mM
Na$_2$HPO$_4$	0.048 g	3.38 mM
NaHCO$_3$	0.35 g	4.16 mM
CaCl$_2$*2H$_2$O	0.185 g	1.26 mM
MgSO$_4$*7H$_2$O	0.1 g	0.41 mM
MgCl$_2$*6H$_2$O	0.1 g	0.49 mM
D-Glucose	3.5 g	19.4 mM
HEPES	2.38 g	10.0 mM
Milli Q water	ad 1000 ml	
pH (apical medium)	adjusted to 6.5 ± 0.05	
pH (basolateral medium)	adjusted to 7.4 ± 0.05	
Transport-FaSSIF (tFaSSIF)		
HBSS^{++} pH 6.5	1000 ml	
sodium taurocholate[*]		3.00 mM
lecithin [*]		0.75 mM

[*] contained in 2.24 g SIF powder

2.10.3   Monolayer characterization and validation of transport study protocol

The transepithelial electrical resistance ($TEER$) of monolayers was monitored prior to and during transport studies. It was measured in transport media at 37 °C. To obtain the resistance of the cell monolayer itself the background resistance of the filter and medium needs to be subtracted. The background resistance was determined by $TEER$ measurements of empty filters under the same conditions as during transport experiments. Background values of 164 Ωcm^2 (measured in cell culture plate) and 125 Ωcm^2 (measured in side-by-side diffusion chambers) were determined. By multiplying with the filter surface area [cm^2] the monolayer resistances [Ω] were converted to the resistance of unit area [Ωcm^2] (Tavelin et al. 2002). Monolayers with $TEER > 250$ Ωcm^2 were used for transport studies.

Experiments with the solutions of the paracellular marker Lucifer Yellow (0.5 mmol/l) and suspensions of the BCS II drugs ketoconazole and griseofulvin (0.5 mmol/l) were performed to validate the permeability assays. The experimental protocols were the same as will be described in the following.

2.10.4   Horizontal permeability assay

In the horizontal permeabilty assay the cell monolayer, grown on a permeable filter support, was positioned horizontally, which is the standard experimental setup for permeability experiments. As filter supports Transwell® inserts were used (polyester membrane, 0.4 μm pore size, $4*10^6$ pores/cm^2, 1.1 cm^2 growth area, Tab. 2.4). The permeability assays were performed in a cellZscope® instrument, which offered automated monitoring of the transepithelial electrical resistance ($TEER$) and the cell capacitance (C_{Cl}) by measuring the frequency-dependent impedance of the cell layer. A background correction of measured $TEER$ values is not necessary with the cellZscope® device and conversion to the resistance of unit area is done automatically by the software. Wegener et al. (2004) described the cellZscope® device and the theoretical background of impedance measurements.

24 h prior to the experiment the cells were put on serum-free feeding medium. All transport media and the cellZscope® instrument were prewarmed to 37 °C. Prior to the experiment the cells were washed twice with transport medium. Subsequently the filter inserts were transfered from the cell culture plate into the cellZscope® instrument and the cell monolayers were allowed to equilibrate for 2 h. During the equilibration and the experiment the instrument was located in a climate chamber at 37 °C and was subjected to gentle horizontal shaking (150 rpm). 1 ml of transport medium with pH 7.4 was used on the basolateral side and 0.5 ml of transport medium with pH 6.5 was used on the apical side.

Meanwhile predilutions of the formulations or solutions to be used in the transport experiment were prepared in apical medium. The concentrations were adjusted so that addition of 200 μl of predilution into 500 μl of apical medium resulted in the concentration desired for the transport experiment. All transport assays were performed in apical to basolateral (A to B) direction. Fenofibrate concentrations of 181 μg/ml (0.5 mmol/l) were used. This concentration is in accordance with Kataoka et al. (2006), who suggested to use 1% of the clinical dose in about 1/100 of the physiological volume of the human GI tract (1.45 mg FF in 8 ml). Compound AS was applied in equimolar dose.

The transport experiment was started by addition of 200 μl of prediluted formulation or solution into the apical compartment. Mixing was performed by gentle up- and down pipetting. Directly after addition

(a) Vertical diffusion chamber system.

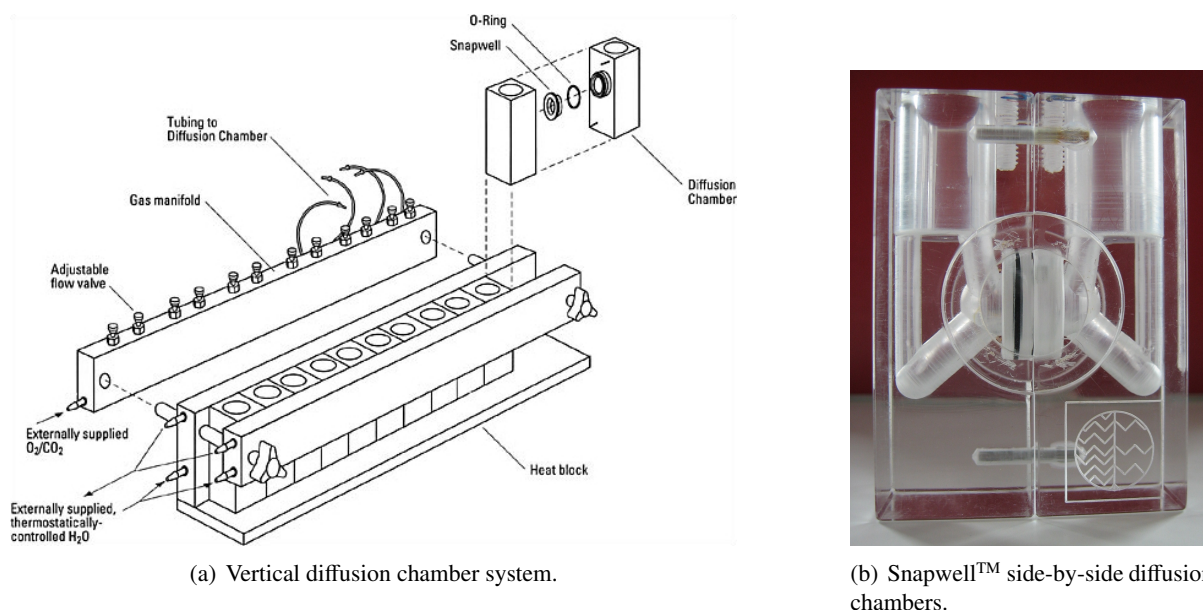(b) Snapwell™ side-by-side diffusion chambers.

Figure 2.3: The vertical diffusion chamber system. Reprint from Warner's Guide to Ussing Chamber Systems; Warner Instruments, LLC, Hamden, CT, USA with kind permission.

and at the end of the experiment a apical sample of $100\,\mu$l was withdrawn. Basolateral sampling was performed after 30, 60, 90 and 120 min. The sample size was $200\,\mu$l and was replaced by fresh transport medium. Samples were stored at -20 °C until concentration determination by HPLC.

2.10.5 Vertical permeability assay

In the vertical permeability assay the cell monolayer was positioned vertically in side-by-side diffusion chambers (Tab. 2.4 and Fig. 2.3). Cells were grown on Snapwell™ inserts (polyester membrane, $0.4\,\mu$m pore size, $4*10^6$ pores/cm^2, 1.1 cm^2 growth area) and the filter supports were mounted in vertical Snapwell™ diffusion chambers. A heater block, designed to hold six diffusion chambers, provided a regulation of temperature by use of an external circulating water bath. A gas manifold distributed carbogen gas to the chambers and media circulation was generated by a gas-lift process. A gas flow meter (rotameter) was used to control the gas flow rate ($80-100$ ml/min) into the gas manifold and via the flow valves the flow into each chamber was fine tuned ($4-6$ bubbles/s).

The transport experiments were carried out at 37 °C. After mounting the filter supports in the diffusion chambers the apical and basolateral chambers were filled with 6 ml of prewarmed transport media. All steps of cell washing, equilibration, preparation of prediluted formulations and sampling were carried out like described for the horizontal permeability assay. Transepithelial electrical resistances were measured at distinct time points with a so-called 'chopstick' device (Millicell®-ERS).

2.10.6 Data evaluation

The determined mass of substrate [μg] appearing in the receiver compartment (corrected for dilutions due to sampling and medium replacement) was plotted against sampling time [s]. Curve fitting using

standard linear regression parameters (coefficient of determination $R^2 > 0.90$) was used to give the rate of drug transport dQ/dt [$\mu g/s$]. The apparent permeation coefficient P_{app} was calculated according to the following equation (Balimane and Chong 2008):

$$P_{app}[cm/s] = \frac{dQ}{dt}\frac{1}{C_0 A} \tag{2.6}$$

C_0 is the initial apical drug concentration [$\mu g/ml$] and A is the surface area of the filter [cm^2].
The recovery of API from transport experiments was calculated by taking into account the amount of API in the apical compartment $Q_{A120min}$ and in the basolateral compartment $Q_{B120min}$ (corrected for dilutions due to sampling and medium replacement) and relating it to the total initial API amount in the apical compartment $Q_{A0min} = C_0 V_A$, with V_A being the volume of apical medium.

$$Recovery[\%] = \frac{Q_{A120min} + Q_{B120min}}{Q_{A0min}} * 100\% \tag{2.7}$$

In the case of fenofibrate its metabolite fenofibric acid occured in donor and receiver compartments during transport studies. For the calculation of API recovery the total amounts of FF and FFA were taken into account.

2.11   In vivo pharmacokinetics

2.11.1   Study setup

Pharmacokinetical (PK) studies on rats were performed for orally (p.o.) administered suspensions of FF and AS with varying particle sizes and for intravenously (i.v.) administered API solutions.
Healty, male Wistar rats with approximately 250 g weight (Charles River, Sulzfeld, Germany) were housed in cages for a minimum of three days prior to administration. Holding and study areas had automatic control of light cycles (12 h light / 12 h dark), temperature ($23 \pm 1°C$) and humidity ($60 \pm 10\%$). Tap water and food (Tab. 2.4) were offered *ad libitum*. Food was removed at least 10 h prior to administration and replaced 3 h after dosing. The animals were uniquely identified by ear marks. Prior to administration animals were weighted and body weights of $200 - 290$ g were registerd.
The intravenous formulations were injected into the tail vein and oral formulations were administered by gastric gavage. Details about the formulations and administration are given below and in Table 2.10. The exact administration volume was adjusted according to the individual animal weight to ensure dose consistency. The dose of fenofibrate was 2.1 mg/kg in accordance with the clinical dose (145 mg for a 70 kg adult) (Buch et al. 2009; Zhu et al. 2010). The dose of compound AS was selected to be equimolar to the fenofibrate dose.
Each study group consisted of six animals and received one of the formulations. Two subgroups with three animals were formed and at four time points blood samples were taken from each animal. The sampling times after administration were: 10 min, 1 h, 3 h and 8 h for group A and 30 min, 2 h, 5 h, 25 h for group B. Data of subgroups were pooled to yield PK profiles with eight data points for each formulation. Blood samples of 200 μl were collected from the tail vein in Li-Heparin coated blood collection tubes

Table 2.10: Summary of *in vivo* pharmacokinetic experiments.

Formulation	administration route	administration volume [μl / 250 g body weight]	dose [mg/kg]	dose [mmol/kg]
Fenofibrate				
FFA solution	intravenous	250	2.1	0.006
NS 140nm	oral	900	2.1	0.006
NS 270nm	oral	900	2.1	0.006
NS 1070nm	oral	900	2.1	0.006
MS 7.9μm	oral	900	2.1	0.006
Compound AS				
AS solution	intravenous	500	1.0	0.002
NS 100nm	oral	800	2.7	0.006
NS 150nm	oral	800	2.7	0.006
NS 860nm	oral	800	2.7	0.006
NS 1320nm	oral	800	2.7	0.006
MS 6.8μm	oral	800	2.7	0.006

Microvette® 200, (Tab. 2.4). Via centrifugation the blood cells were separated off to gain the blood plasma. Plasma samples were stored at -20°C and analyzed within 21 days (section 2.6). After the last sampling time the rats were sacrificed by CO_2 - asphyxia.

2.11.2 Intravenous formulations

The objective of i.v. formulation development was to yield clear solutions with a sufficiently high API concentration to achieve an administration volume of maximal 500 μl. For that purpose various compositions of solubilizers and cosolvents in phosphate buffered saline (PBS, Table 2.11) were screened with the intention of keeping the percentage of additives low. The formulations which resulted in stable particle free solutions were chosen as i.v. formulations. Visual inspection was performed to control for absence of particles.

Fenofibric acid was selected for i.v. administration instead of fenofibrate, since very high percentages of additives were necessary to generate a solution of fenofibrate with the desired concentration. *In vivo* a very rapid and complete metabolization of fenofibrate takes place during oral absorption and only fenofibric acid can be found in the blood compartment. This offers the possibility of comparing intravenous fenofibric acid administration to oral fenofibrate administration (Zhu et al. 2010). Solutions of fenofibric acid (2 mg/ml) were obtained by adding fenofibric acid to a solution of 5 % macrogol-15-hydroxystearate in PBS and stirring for 5 h. A filtration step (Anotop 10 syringe filter, 0.1 μm) was performed to guarantee particle freeness.

The i.v. vehicle for AS consisted of 10 % macrogol-15-hydroxystearate and 5 % of ethanol in PBS. By stirring of an excess amount of the API (1 mg/ml) for 20 h and susbsequent filtration (Anotop 10 syringe filter, 0.1 μm) it was possible to obtain a solution of compound AS with 0.5 mg/ml.

Table 2.11: PBS.

Dulbecco´s phosphate buffered saline (PBS)		
KCl	0.2 g	2.68 mM
KH_2PO_4	0.2 g	1.47 mM
NaCl	8.0 g	137 mM
Na_2HPO_4	1.15 g	8.10 mM
Milli Q water	ad 1000 ml	
pH	adjusted to 7.4 ± 0.05	

2.11.3   Oral formulations

Micro- and nanosuspensions were orally administered. Their API concentration was adjusted to $0.6 - 0.8$ mg/ml by dilution in Milli Q water to yield an administration volume of $800 - 900 \, \mu$l for a rat of 250 g weight. The diluted suspensions were stirred during withdrawal of the appropriate volumes into syringes to guarantee administration of homogeneous suspensions and administration to animals was performed immediately. The stability of particle size in the diluted suspensions was assured.

2.11.4   Data evaluation

Complete plasma concentration-time profiles for each formulation / study group were obtained by pooling the data points of subgroups A and B. Plasma concentration-time profiles with eight data points from a total number of six animals were obtained, in which each data point was taken from three animals.

The pharmacokinetic parameters C_{max} and T_{max} were directly taken from the plasma concentration-time profiles. C_{max} is the maximum observed plasma concentration and T_{max} is the time at which C_{max} is observed. The area under the concentration-time curve $AUC_{0 \to 25h}$ expresses the bioavailability F and was calculated by integration of the concentration-time curve data points from 0 to 25 h.

The absolute bioavailability F_{abs} of an API is defined to be 100 % for i.v. administration of the API. The absolute bioavailabilitiy of an orally administed suspension is calculated as:

$$F_{abs} = \frac{AUC_{p.o.} * dose_{i.v.}}{AUC_{i.v.} * dose_{p.o.}} * 100\% \tag{2.8}$$

The relative bioavailability F_{rel} of the nanosuspensions (NS) was calculated with reference to the $AUC_{0 \to 25h}$ of the microsuspensions (MS):

$$F_{rel} = \frac{AUC_{NS}}{AUC_{MS}} * 100\% \tag{2.9}$$

2.11.5   Pharmacokinetic modeling & simulation

The Advanced Compartmental Absorption and Transit (ACAT) Simulation Model was used to analyze and to model the pharmacokinetics of micro- and nanoparticulate formulations. The ACAT model is implemented in the GastroPlus^{TM} software (version 8.0, Simulations Plus, Inc., Lancaster, CA, USA).

2.12   Statistics

All values are presented as arithmetic means ± standard deviation if not otherwise stated. Statistical significance was tested by the two-tailed Student´s *t*-test (Microsoft Excel software).

Results and Discussion

3.1 Micro- and nanosuspensions

3.1.1 Particle size and morphology

Table 3.1 summarizes the results of SLS and DLS measurements and in Figure 3.1 the particle size distributions are illustrated. Since all suspensions employed in this study have the same composition ($API / HPMC / DOSS / H_2O = 20 / 2.5 / 0.1 / 77.4$) the most distinctive feature was their particle size.

The SEM images of selected nanosuspensions displayed in Figure 3.2 provide information about the particle morphology. It can be seen that harsher milling conditions applied to FF NS 140nm and AS NS 100nm lead to smoother particles with a shape closer to ideal sphericity (see section 2.2 for manufacturing details). The formulation AS NS 860nm, which was produced by a low energy process, does not only comprise bigger particles with a wider particle size distribution, but also more irregularly shaped particles with sharp edges.

3.1.2 Suspension production process

The agitator ball milling process is very efficient in terms of particle size reduction. Figure 3.3(a) gives an example of how compound AS particle size developed during the milling process. It can be seen that within only a few minutes nanoparticles were generated. However, particle size distributions at short process times were wide and bimodal . After 10 min only a very small fraction of micron sized particles remained and in the continuation of the process this fraction disappeared, while the percentage of small particles increased. However, an only marginal further decrease of the minimum particle size was observed for longer milling times. The fenofibrate particle size reduction by agitation ball milling

(a) Fenofibrate suspensions.
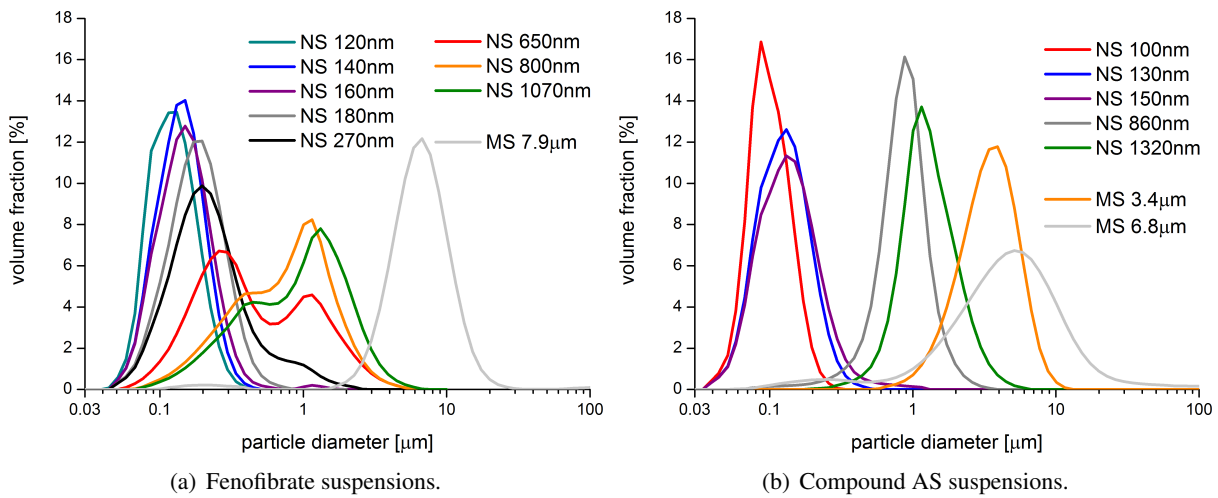
(b) Compound AS suspensions.

Figure 3.1: Particle size distributions of FF and AS micro- and nanosuspensions measured by SLS.

Table 3.1: Particle size of of FF and AS micro- and nanosuspensions.

Formulation	SLS diameter				DLS diameter	
[nm]	Mean	D10	D50	D90	Z-Average	PDI
Fenofibrate						
NS 120nm	123 ± 4	72 ± 1	113 ± 3	188 ± 7	219 ± 2	0.204 ± 0.005
NS 140nm	138 ± 2	79 ± 1	130 ± 2	210 ± 4	215 ± 4	0.184 ± 0.013
NS 160nm	156 ± 12	80 ± 2	138 ± 5	237 ± 13	280 ± 5	0.189 ± 0.024
NS 180nm	184 ± 5	92 ± 2	168 ± 5	293 ± 9	296 ± 3	0.183 ± 0.021
NS 270nm	266 ± 3	97 ± 1	193 ± 3	501 ± 10	381 ± 10	0.265 ± 0.041
NS 650nm	645 ± 79	142 ± 29	365 ± 89	1491 ± 100	618 ± 25	0.207 ± 0.036
NS 800nm	797 ± 109	155 ± 64	647 ± 214	1630 ± 53	714 ± 79	0.566 ± 0.444
NS 1070nm	1068 ± 44	247 ± 40	918 ± 42	2099 ± 73		
MS 7.9μm	7900 ± 1780	3357 ± 202	6118 ± 318	10979 ± 919		
Compound AS						
NS 100nm	98 ± 1	61 ± 1	91 ± 1	144 ± 3	215 ± 8	0.183 ± 0.017
NS 130nm	126 ± 2	68 ± 0	116 ± 2	196 ± 4	261 ± 5	0.127 ± 0.018
NS 150nm	145 ± 8	69 ± 0	124 ± 3	232 ± 18	270 ± 5	0.128 ± 0.025
NS 860nm	855 ± 52	475 ± 71	811 ± 34	1275 ± 74	588 ± 78	0.161 ± 0.089
NS 1320nm	1321 ± 80	700 ± 47	1164 ± 54	2142 ± 150		
MS 3.4μm	3432 ± 102	1649 ± 95	3207 ± 117	5513 ± 125		
MS 6.8μm	6827 ± 840	1162 ± 188	4295 ± 421	11728 ± 1400		

(a) Fenofibrate: NS 140nm   (b) Compound AS: NS 100nm   (c) Compound AS: NS 860nm
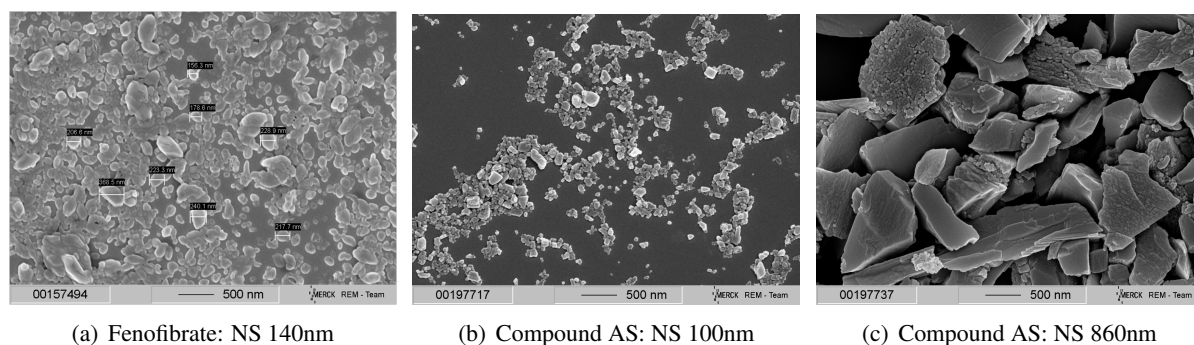
Figure 3.2: Scanning electron microscopy micrographs of different nanosuspensions.

proceeded in a very similar way (data not shown).

The agitator ball milling process was very well suitable for the production a nanosuspensions with a very small particle size. However, the milling conditions were to harsh to generate larger sized suspensions. Therefore a low energy ball milling process was developed. With this process the particle size reduction was much slower and easier to control. However, it followed a similar scheme than the agitator ball milling with the generation of bimodal size distributions. The implementation of post milling process steps helped to gain suspensions with monomodal size distribution out of bimodal milling products. Figure 3.3(b) gives an example.

The development of particle size during the milling process and the SEM images (Fig. 3.2) give indications on the mechanism of particle size reduction for the applied systems. Rather crystal breaking than crystal friction can be assumed to be the main mechanism, since friction would lead to a more continuous size reduction. The particle shape of NS 860nm suggests that particles have been formed by breaking or splitting of bigger sized API crystals. Since the smaller suspensions have a smoother surface and a more roundish shape, friction seems to become more important for the shaping of small API crystal fragments.

3.1.3 Physical state

To investigate the physical state of the APIs in nanosuspensions a DSC analysis was performed for selected formulations of fenofibrate and compound AS. Thermograms are exemplarily shown for compound AS in Figure 3.4. Endothermic peaks indicate melting of API crystals and no other thermic events were observed. By peak integration the enthalpies of fusion were determined to be 129 ± 5 J/g for compound AS and 149 ± 6 J/g for fenofibrate (data not shown). Melting points were determined to be $213°C$ for compound AS and $83°C$ for fenofibrate. Both are in good accordance with previously reported data (Tab. 2.1). Relative enthalpies of fusion (API in suspensions / pure API) were calculated to be $80 - 100\,\%$, indicating that no relevant transformation of physical state appeared during milling (Fig. 3.5). All suspensions contained crystalline API. A slight decrease in melting temperature with decreasing particle size can be observed and has been reported and discussed previously.

(a) NS 100nm: Production process

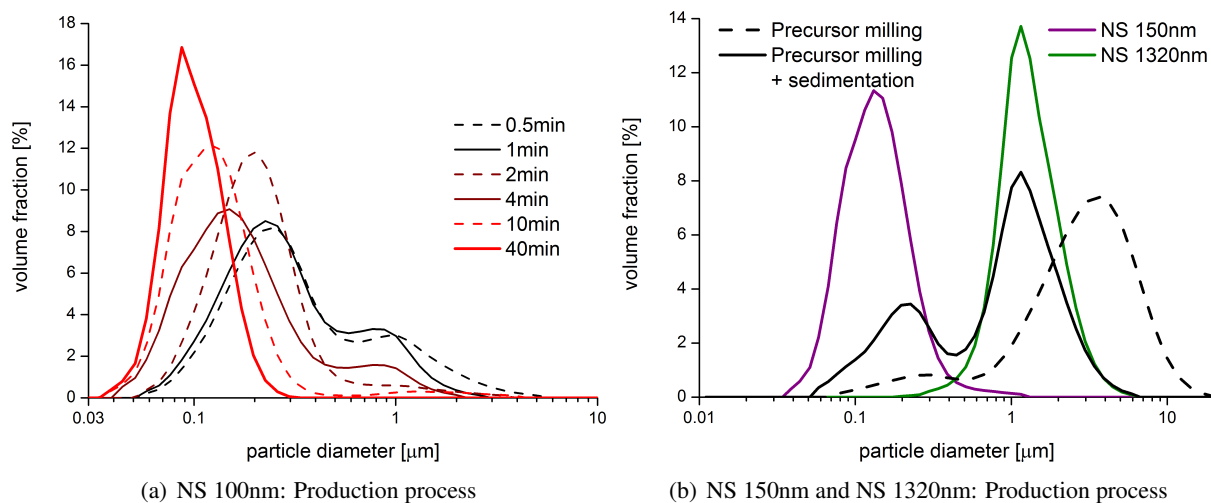(b) NS 150nm and NS 1320nm: Production process

Figure 3.3: Examples for compound AS suspension production. Particle size distributions of final products and precursors measured by SLS. (a) Production of NS 100nm by agitator ball milling and in-process controls at different milling time points. (b) Production of NS 150nm and NS 1320nm by low energy ball milling and two post milling process steps. (1) Milling product of low energy process at 500 rpm and 5 h milling time (dashed black line). (2) Supernatant of the milling product taken after 5 days of sedimentation (black line). (3) 1.5 ml of the supernatant were centrifuged (4000 g, 10 min). Sampling of the uppermost 0.8 ml of supernatant resulted in NS 150nm (purple line). The middle supernatant layer 0.2 ml was discarded. The lowermost 0.5 ml were redispersed in 1 ml of water and this resulted in NS 1320nm (green line).
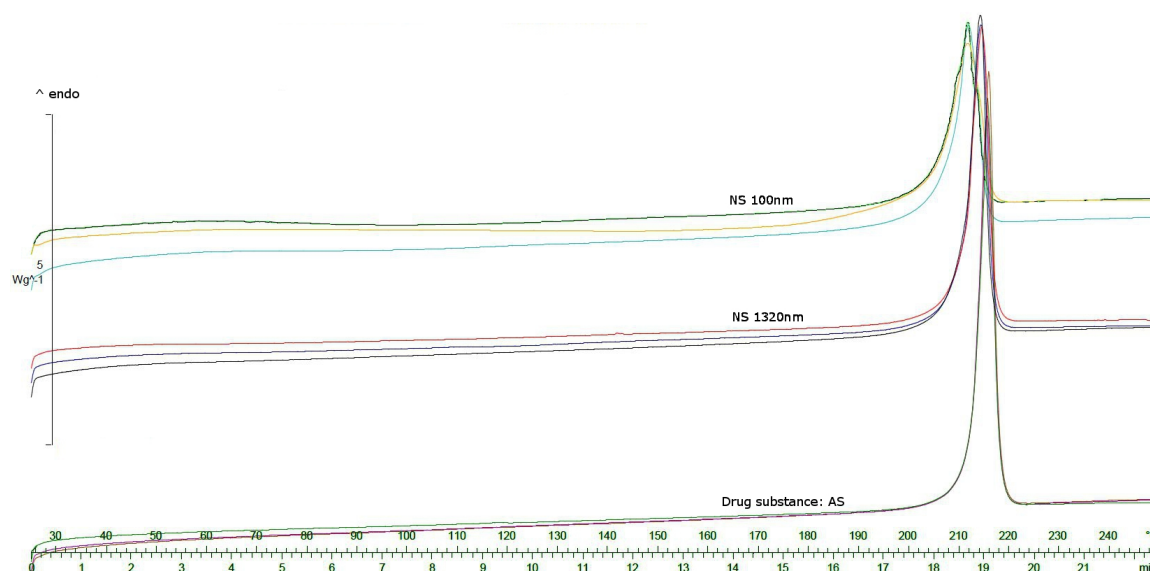

Figure 3.4: DSC thermograms of compound AS drug substance and selected AS formulations. Thermograms show the heat flux versus temperature with endothermic reactions displayed in positive direction ($n = 3$).

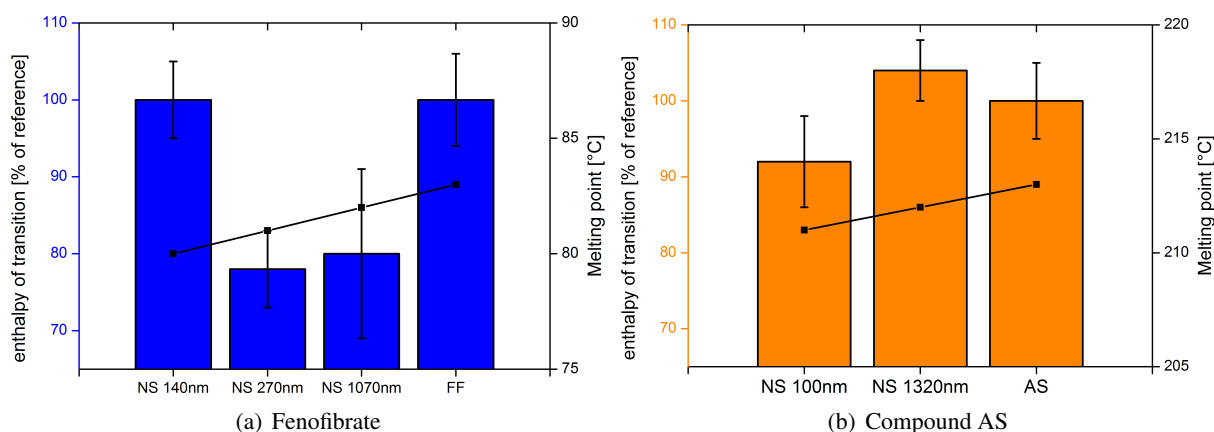(a) Fenofibrate   (b) Compound AS

Figure 3.5: Relative enthalpies of fusion (API in suspensions / pure API) (columns) and melting points (lines) of APIs and selected formulations determined by differential scanning calorimetry.

3.1.4 Stability

Formulations were stable for a minimum of four weeks at $4 - 8°C$ in terms of particle size and physical state (data not shown). For bigger sized nanosuspensions and microsuspensions particle sedimentation occurred. However, the particles were completely redispersable by stirring or vortex mixing.

3.2   Dissolution media

Simulated gastric fluid supplemented with 0.1% of Tween® 80 (SGF + Tween) was mainly used as dissolution medium. It was characterized by DLS measurements on eight batches. The size of polysorbate 80 (Tween® 80) micelles was 10.6 ± 0.9 nm with a polydispersity index of 0.112 ± 0.040. Blank medium measurements for dissolution experiments gave scattering intensities of 82 ± 5 kcps at attenuator setting 10. The refractive index was determined to be 1.334 ($n = 3$) and hence did not relevantly deviate from the refractive index of water (1.333). That the viscosity of SGF + Tween does not change sigificantly compared to the viscosity of water was reported elswhere (Lange 2009). Stability of SGF + Tween at $4 - 8°C$ was demonstrated for seven days in terms of micelle size, absolute scattering intensity and pH (data not shown).

Fasted-state simulated intestinal fluid (FaSSIF) was evaluated as an alternative dissolution medium. It was characterized by DLS measurements on seven batches. The size of micelles was 43.6 ± 8.2 nm with a polydispersity index of 0.027 ± 0.011. Blank medium measurements for dissolution experiments gave scattering intensities of 196 ± 91 kcps at attenuator setting 7.

(a) Polystyrene nanoparticles.
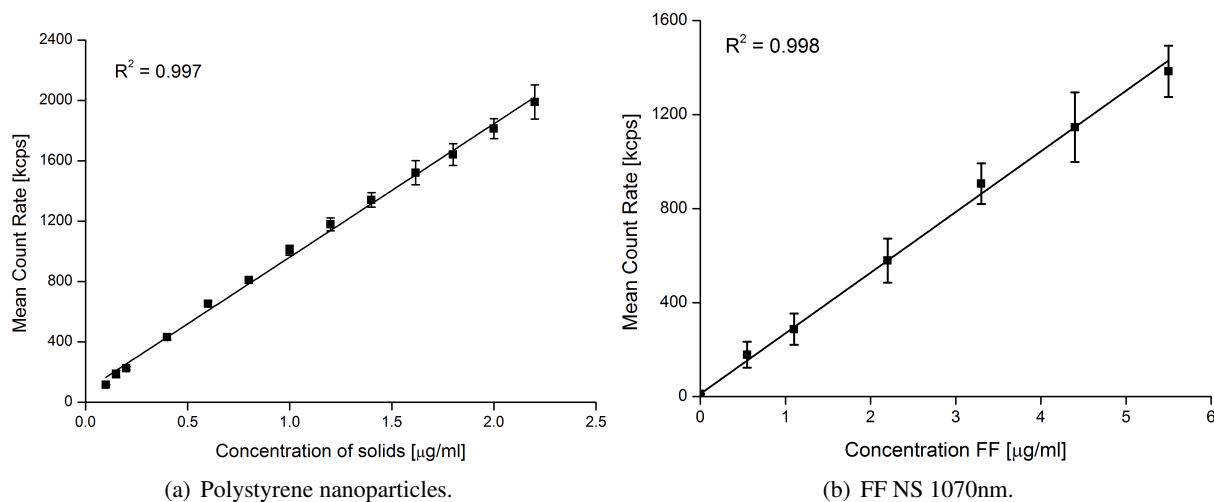
(b) FF NS 1070nm.

Figure 3.6: Correlation of particle concentration and scattering intensity. Scattering intensities were measured with a Zetasizer instrument and are expressed as mean count rate.

3.3   Light scattering measurements

3.3.1   Validation

Figure 3.6 shows the results of the light scattering intensity validation experiments. For the spherical polystyrene nanoparticles a linear correlation between particle concentration and scattering intensity prevailed in the range of 100-2000 kcps (R^2 = 0.997). This linear correlation is in accordance with theory (van de Hulst 1957; Elsayed and Cevc 2011) and consequently this experiment served as a proof for linear functionality of the laser and detector for the considered instrument settings and measured scattering intensities. For higher particle concentrations and therefore higher scattering intensities a deviation from linearity was observed. In the second experiment the investigation of dependence of scattering intensity on concentration was extended to the suspension NS 1070nm. In contrast to the Nanosphere[TM] Size Standard this system is polydisperse with particles in the nano- to micrometer range and particle shape deviates from ideal sphericity. Nevertheless a linear correlation of scattering intensity and particle concentration was observed (R^2 = 0.998).

3.4 Solubility

Parts of this section are published in Anhalt et al. (2012)

The solubilities of drug substances and nanosuspensions in different media were determined. The conventional setup applied for drug substance solubility measurement is a separation based technique: API is dispersed and after an equilibration time the solid material is separated to quantify the concentration of dissolved API. For the nanosuspensions not a separation based technique, but a light scattering approach was evaluated to determine solubilities.

3.4.1 Drug substances

Table 3.2 summarizes the solubilities of APIs. The solubility of fenofibrate was determined in SGF supplemented with Tween® 80 at various concentrations. A linear correlation of the Tween® 80 concentration and solubility was demonstrated ($R^2 = 0.995$):

$$\text{solubility } [\mu g/ml] = 83.90 \, [\mu g/ml/\%] \times \text{concentration Tween® 80 } [\%] + 0.16 \, [\mu g/ml]$$

Table 3.2: Solubility of APIs in different media after 24 h of equilibration at 25°C.

Medium	API solubility [μg/ml]	
	Fenofibrate	**Compound AS**
H$_2$O	0.10 ± 0.07	
SGF	0.12 ± 0.08	
SGF + 0.01%[*]Tween 80	1.17 ± 0.30	
SGF + 0.05% Tween 80	4.04 ± 0.19	
SGF + 0.1% Tween 80	8.69 ± 0.78	11.92 ± 0.87
FaSSIF	11.26 ± 1.47	9.27 ± 1.42

[*] mass %

3.4.2 Nanosuspensions

The solubilities of nanosuspensions were determined in SGF + 0.1% Tween 80 by a light scattering approach. Figures 3.7 and 3.8 present the scattering intensity vs concentration graphs. In Table 3.3 all parameters of the curve analysis and resulting calculated solubilities are listed.

For the linear function fitting data points at concentrations c with $8.0 < c < 10.5 \, \mu g/ml$ (FF) and with $4.5 < c < 6.0 \, \mu g/ml$ (AS) were excluded. They are close to the solubility limit and have a high uncertainty of data interpretation (Van Eerdenbrugh et al. 2010). For the horizontal branches, which correspond to dissolved samples, coefficients of correlation are low. This can be explained by a low signal-to-noise ratio for the measured scattering intensities of $75 - 90 \, kcps$. Nevertheless low coefficients of correlation do not alter the data analysis essentially, since the horizontal and ascending branches can be clearly distinguished regarding slope and intercept.
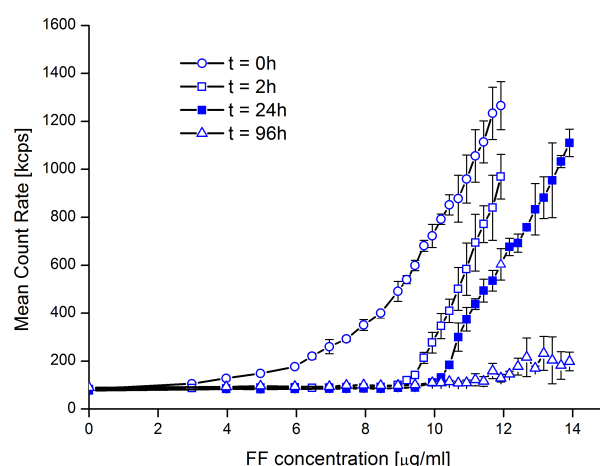
Figure 3.7: Solubility of fenofibrate nanosuspension NS 140nm determined by light scattering method with variation of equilibration time. Measured scattering intensity vs total FF concentration ($n = 3$).

Evaluation of a suitable equilibration time

The fenofibrate formulation NS 140nm was used to evaluate the effect of equilibration time on the determination of nanosuspension solubility (Fig 3.7). The aim was to identify the time necessary to reach an equilibrated system (stable dissolved and solid concentration over time) for the determination of equilibrium solubility.

The 0 h-graph shows the scattering data recorded 10 s after dilution and it exhibits a curved shape. However, for stable particles a linear increase of scattering intensity with increasing particle concentration would be expected. The deviation from linearity indicates that particles are not stable and that the particle dissolution process has already started. After 2 h the two-branched shape becomes visible, in which the horizontal branch corresponds to completely dissolved samples and the rising branch to partially dissolved samples. After 24 h the picture is the same with a shift to higher concentrations. After 96 h the rising branch flattens and it is not possible to clearly identify a linear progression due to signal fluctuations.

It was not possible to identify the time to reach a completely equilibrated system, in which the solubility would correspond to saturation solubility. It seems that after 96 h the solubility further increased. However, data interpretation from the 96h-graph is subject to statistical shortcomings: The fluctuations of the scattering signal can be explained by number fluctuations in the scattering volume. The term number fluctuation describes the effect of a very low number of particles in the scattering volume, which results in poor statistical validity of the measurement. Data interpretation of the 96h-graph is further challenged by possible changes in particle size distribution and therefore light scattering properties of the system, since not only dissolution, but also aggregation or Ostwald ripening might have been occurred. Furthermore, adsorption of API or particles onto the plastic cuvettes might be a potential source of error and might be responsible for the shift of scattering graphs towards higher concentrations for longer equilibration times.

As a conclusion of the described results, the equilibration time of 24 h was selected for further experiments, because on the one hand the particle dissolution process is in an advanced state and on the other
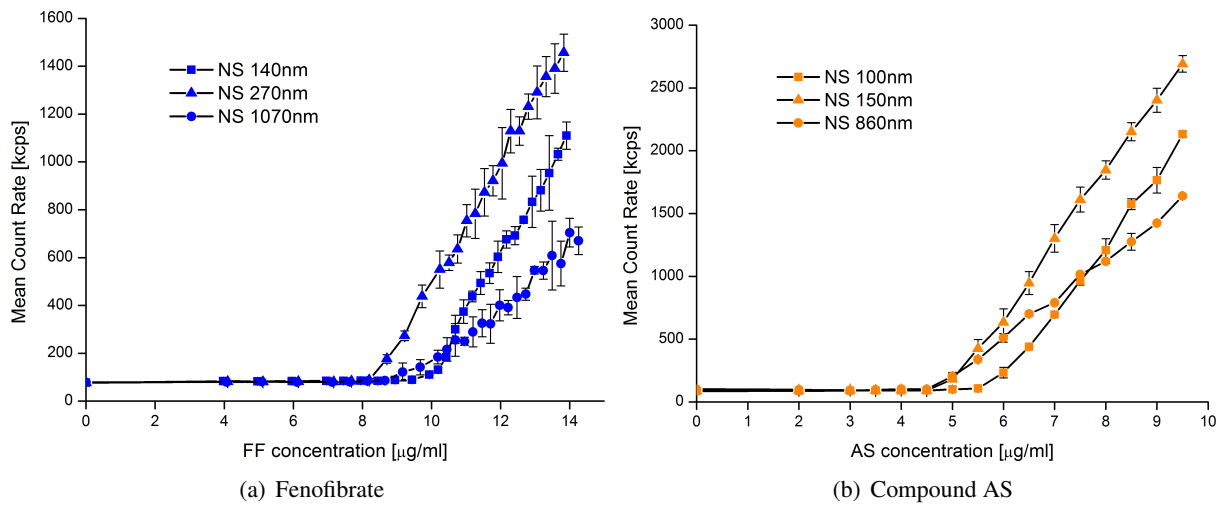
(a) Fenofibrate

(b) Compound AS

Figure 3.8: Solubility of FF and AS nanosuspensions determined by light scattering method with an equilibration time of 24 h. Measured scattering intensity vs total concentration ($n = 3$).

hand data interpretation is still possible with adequate statistical quality. Following the definitions given by Sugano et al. (2007) the measured solubilities (S_{NS}) are apparent solubilities, meaning that reasonable long incubation times were chosen without the confirmation of stable dissolved and solid concentration over time.

Solubility of fenofibrate nanosuspensions

Figure 3.8(a) and Table 3.3 present the solubilities (S_{NS}) determined for fenofibrate suspensions with varying particle size.

For NS 140nm a significantly higher solubility was determined than for NS 270nm (9.86 ± 0.02 vs 8.70 ± 0.24 µg/ml). This finding is consistent with the Ostwald-Freundlich equation (Eq. 1.1) in terms of an expected higher solubility for the smaller sized nanosuspension. However, the solubility of NS 1070nm was calculated to be 9.62 ± 0.50. µg/ml and hence higher than for the suspensions NS 270nm with smaller particle size. This result can be interpreted as a lack of suitability of the scattering method for NS 1070nm, which is due to the suspensions large particle size and therefore low particle number density (number of particles per volume). At concentrations just above the solubility limit only few undissolved particles remain, which are not detectable with the optical configuration of the Zetasizer^{TM}. This provokes the misleading interpretation of these samples as dissolved, where there might indeed be particles left, and consequently leads to an overestimation of solubility. Another effect, which amplifies the shortcomings of the scattering method for this suspension, is that smaller particles dissolve preferentially and the size distribution is altered towards bigger particles, that are more difficult to be detected (Van Eerdenbrugh et al. 2010). Furthermore, instabilities like aggregation and Ostwald ripening can also lead to larger particles and thus increase the error. Even though samples are shaken up directly before each measurement, settling of particles during the measurement might contribute to the high standard deviations as well.

Table 3.3: The solubilities of pure crystalline APIs and nanosuspensions in SGF + 0.1 % Tween at 25°C. The solubilities of APIs S_{API} were determined by conventional method. The solubilities of nanosuspensions S_{NS} were determined by light scattering method and the results of the linear function fitting are presented as well as the thereof derived solubilities.

	time [h]		Linear function fitting[*]			Solubility	
			Slope [kcps/μg/ml]	Intercept [kcps]	R^2	absolute [μg/ml]	relative[**] [% S_{API}]
Fenofibrate							
NS 140nm	2	dissolved	0.9	82.9	0.752	9.57 ± 0.17	110.1 ± 9.1
		undissolved	365.8	-3408.4	0.995		
	24	dissolved	1.0	77.5	0.910	9.86 ± 0.02	113.4 ± 9.0
		undissolved	246.4	-2340.8	0.994		
	96	dissolved	1.1	88.7	0.683	10.38 ± 0.01	119.5 ± 9.0
		undissolved	32.7	-239.7	0.751		
NS 270nm	24	dissolved	1.0	76.2	0.661	8.70 ± 0.24	100.1 ± 9.4
		undissolved	276.2	-2318.4	0.992		
NS 1070nm	24	dissolved	0.4	78.3	0.392	9.62 ± 0.50	110.7 ± 10.4
		undissolved	129.3	-1162.5	0.964		
FF	24					8.69 ± 0.78	100.0 ± 12.7
Compound AS							
NS 100nm	24	dissolved	1.0	85.8	0.464	5.78 ± 0.13	48.5 ± 7.7
		undissolved	516.1	-2896.2	0.997		
NS 150nm	24	dissolved	0.6	90.4	0.343	5.05 ± 0.21	42.3 ± 8.4
		undissolved	590.0	-2884.8	0.994		
NS 860nm	24	dissolved	-0.1	98.4	0.002	4.59 ± 0.02	38.5 ± 7.3
		undissolved	301.5	-1284.8	0.989		
AS	24					11.92 ± 0.87	100.0 ± 10.4

[*] For FF linear functions were fitted to data points at concentrations c with $c \leq 8.0\,\mu$g/ml representing dissolved samples and with $c \geq 10.5\,\mu$g/ml representing undissolved samples. For AS the respective concentrations were $c \leq 4.5\,\mu$g/ml and $c \geq 6.0\,\mu$g/ml.

[**] Relative solubility values are calculated as $S_{NS}/S_{API} * 100\%$.

Solubility of compound AS nanosuspensions

Figure 3.8(b) and Table 3.3 present the solubilities (S_{NS}) determined for compound AS suspensions with varying particle size.

For NS 100nm a higher solubility was determined than for NS 150nm and for NS 860nm (5.78 ± 0.13 vs 5.05 ± 0.21 vs $4.59 \pm 0.02\,\mu$g/ml). This finding is consistent with the Ostwald-Freundlich equation (Eq. 1.1). The nanosuspension NS 860nm (SLS $D90 = 1.3\,\mu$m) is better suitable for a solubility determination by the scattering method than the fenofibrate suspension NS 1070nm (SLS $D90 = 2.1\,\mu$m), due to its lower particle size and narrower size distribution. The potential sources of error in the solubility determination, which are discussed above for FF NS 1070nm, are less likely to occur for NS 860nm.

However, one major difference for both APIs was observed. Lower solubilities of AS nanosuspensions were determined than for the pure crystalline AS drug substance. On the contrary for fenofibrate the opposite effect, which is consistent with the Ostwald-Freundlich theory, was observed.

The different methods used for nanosuspension and API solubility determination might be the reason. The methodical differences are the mode of sample agitation and the concentration gradient of solid vs dissolved API during the 24 h equilibration period. In the standard light scattering setup samples are equilibrated in rested cuvettes. To evaluate the influence of sample agitation on solubility the nanosuspension NS 100nm was diluted to concentrations of $0 - 16\,\mu$g/ml and in accordance to the drug substance solubility method samples were stirred during equilibration. Subsequently the sample was transferred to a cuvette and the scattering intensity was determined. No major differences could be identified between rested and stirred samples (Fig 3.9(a)).

To evaluate the effect of concentration gradient the nanosuspension solubility was determined according to the drug substance solubility determination protocol: nanosuspension dilution, 24 h stirring, filtration (Whatman Anotop 10 0.02μm) and HPLC quantification of dissolved API. Figure 3.9(b) shows that indeed an increasing fraction of dissolved API was seen when the total nanosuspension concentration during equilibration was increased. It appears that for AS the concentration gradient and therefore solution pressure is one determining parameter of the solubility measured after 24 h. This assumption is supported by a comparison of API and nanosuspension solubilities determined by using a similar gradient: For the determination of AS drug substance solubility a high excess of API ($10000\,\mu$g/ml) was used and the API solubility was $11.26 \pm 1.47\,\mu$g/ml. For the highest tested nanosuspension concentration ($2000\,\mu$g/ml) a similar value was determined: $12.77\,\mu$g/ml.

It can be concluded that a 1000 times higher concentration gradient in the protocol to measure the drug substance solubility than in the protocol to measure the nanosuspension solubility could explain higher solubilities determined for pure AS drug substance.

Nanosuspension solubility determination by the light scattering method: Discussion

The light scattering based determination of nanosuspension solubility proved to be a reproducible, sensitive and experimentally convenient approach. The suitability of the Zetasizer® instrument for this application was demonstrated.

Limitations of the applied method became apparent for samples with mainly micron sized particles.

(a) Stirring vs resting
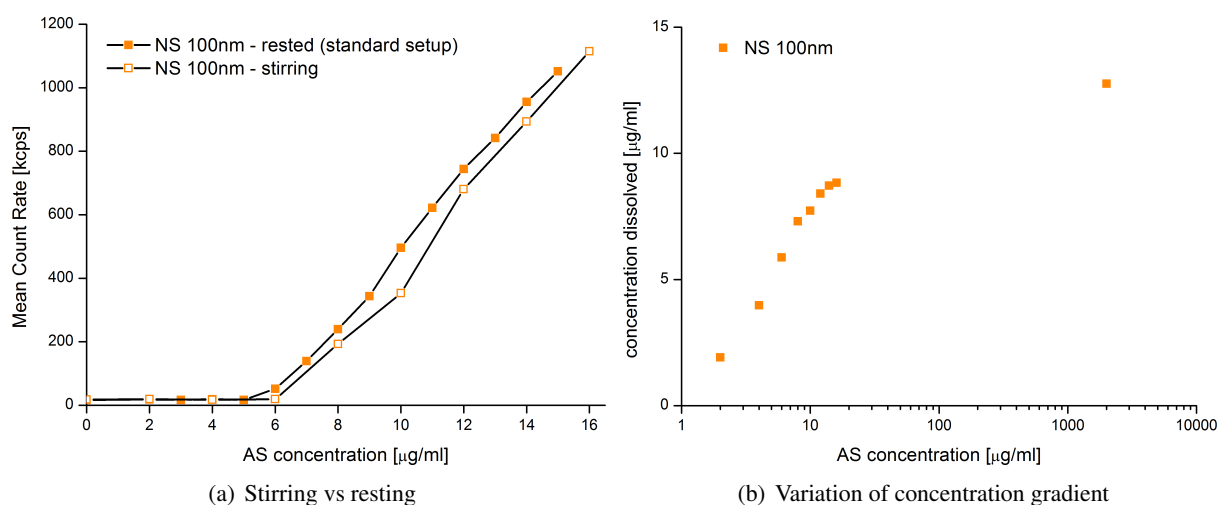
(b) Variation of concentration gradient

Figure 3.9: Methodical variations for the determination of AS nanosuspension solubility. (a) The standard setup with rested cuvettes during equilibration period was varied by applying agitation by magnetic stirring. Scattering intensities were subsequently measured at attenuator 8 ($n = 1$). (b) Nanosuspension solubility determination according to the drug substance solubility method (Stirring, filtration, quantification of dissolved API) with varying concentration gradients ($n = 1$).

Their reduced particle number density and the sedimentation tendency of microparticles negatively affect data quality. Additionally it was seen that the amount of excess API during equilibration, resulting in differences in concentration gradient of solid vs dissolved API, can be a critical parameter.

Previously relative solubilities of 114.5 ± 2.1% for a itraconazole nanosuspension (Z average 220 ± 4 nm), 106.7 ± 1.0% for a phenytoin nanosuspension (Z average 406 ± 17 nm) and 97.0 ± 1.4% for a naproxen nanosuspension (Z average 288 ± 4 nm) have been reported (Van Eerdenbrugh et al. 2010). We determined relative solubilities of 113.4 ± 9.0% for NS 140nm (Z average 215 ± 4 nm) and of 100.1 ± 9.4% for NS 270nm (Z average 381 ± 10 nm). These results are in accordance with published and theoretically predicted values ((Van Eerdenbrugh et al. 2010; Kesisoglou and Wu 2008) and hence confirm the adequacy of the proposed method to determine nanocrystal solubility.

Unlike in previous publications (Van Eerdenbrugh et al. 2010; Lindfors et al. 2006) all dilutions were prepared in one step and were not gradually increased by stepwise addition of suspensions to the cuvette. This approach was chosen to be in close analogy to the standard procedure, in which an excess drug amount is added at the beginning. Due to preferential dissolution of smaller size fractions and Ostwald ripening, a one step dilution might lead to different size distributions and scattering properties among the samples and could influence results. We demonstrated that this effect was not relevant for the determination of solubilities of the smaller sized suspensions. Linearity of the ascending branch and reasonable results confirm the suitability of the presented method. However, a gradual increase of concentration might improve the suitability of the method for the determination of bigger sizes suspensions (like for example NS 1070nm).

The experimental error of the solubility determination by light scattering is small compared to the uncertainty of the drug substance solubility determination (Tab. 3.3). Relative standard deviations of S_{NS}

for FF NS 140nm and 270nm are 0.3% and 2.8% compared to 9.0% for the drug substance solubility S_{FF}. Therefore, most of the variability in the calculated relative solubilities (S_{NS}/S_{API}) originates from S_{FF}. This highlights the potential of the proposed method to determine relevant solubility differences of nanocrystal formulations with good precision.

3.4.3 Summary and conclusions

Solubilities of APIs and nanosuspensions in different media were determined. A light scattering based determination of nanosuspension solubility proved to be a reproducible, sensitive and experimentally convenient approach. The advantages over separation based techniques and the good agreement of measured with estimated solubilities based on Ostwald-Freundlich equation were summarized by Van Eerdenbrugh et al. (2010). It was seen that the applicability of the light scattering method for particle suspensions with micron sized particles is limited and that the concentration gradient during equilibration could influence results. Experiments on a greater number of APIs and formulations will help to better characterize the strengths and limitations of the new method.

Previous investigators (Van Eerdenbrugh et al. 2010; Lindfors et al. 2006) focused on the solubility increase by nanosuspensions but not on the kinetic nature of the dissolution process. From the findings of the here presented experiment dealing with time variations (Fig. 3.7) the importance of the time factor becomes obvious. The nanocrystal dissolution experiments presented in section 3.6 can be regarded as a consistent continuation of the solubility experiments with a shift of the timescale from hours to minutes.

3.5   Dissolution

Different techniques were evaluated to measure nanocrystal dissolution profiles. The results are summarized in this section. The benchmark methods for dissolution testing are the compendial methods of the pharmacopoeias, which follow the steps of dilution, sampling, separation and quantification. A compendial dissolution setup with a USP II (paddle) apparatus and sample filtration was used in this study for microparticle dissolution measurements. Furthermore its applicability for nanosuspensions was evaluated. As an alternative to the sample filtration step in the compendial setup a separation by a dialysis membrane was tested. Finally noninvasive in-situ analytical techniques were evaluated for their suitability to measure nanocrystal dissolution. A light scattering method was the most promising approach and the development and use of this novel setup will be presented in a separate section (section 3.6).

3.5.1   Conventional method: Sampling and separation

The dissolution profiles of selected suspensions of fenofibrate and compound AS were measured using the conventional dissolution setup (Fig. 3.10). The dissolution of a FF nanosuspension was tested as well (Fig. 3.11(a)). Even though sampling intervals as short as 20 s were applied only few data points were collected during the short dissolution time (100 % of API were released after 2 min). In addition high standard deviations were observed and make it difficult to discriminate between similar nanoscalic formulations. Xia et al. (2010) and Quinn et al. (2012) used comparable methods to measure nanocrystal dissolution and report very similar dissolution profiles with 100 % of API released after 5 min.
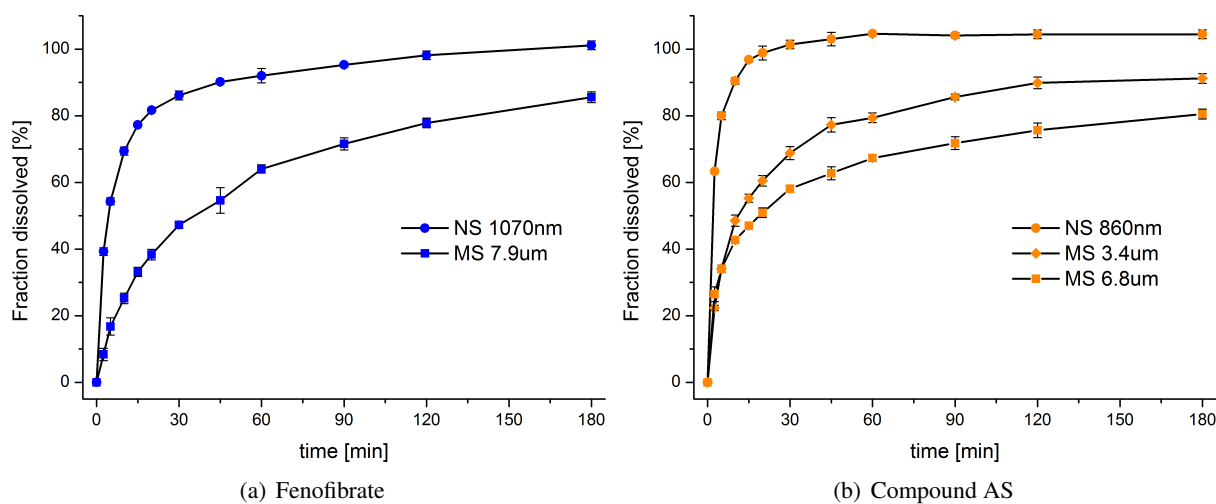

Figure 3.10: Conventional dissolution of FF and AS suspensions in SGF + 0.1 % Tween 80. (a) FF concentration 5.5 μg/ml. (b) AS concentration 2.7 μg/ml ($n = 3$).

3.5.2   Dialysis method: Continuous separation

The conventional sampling and separation experiment was modified by using a dialysis setup. A nanosuspension was injected into a dialysis cassette (donor) floating in the dissolution medium in a paddle

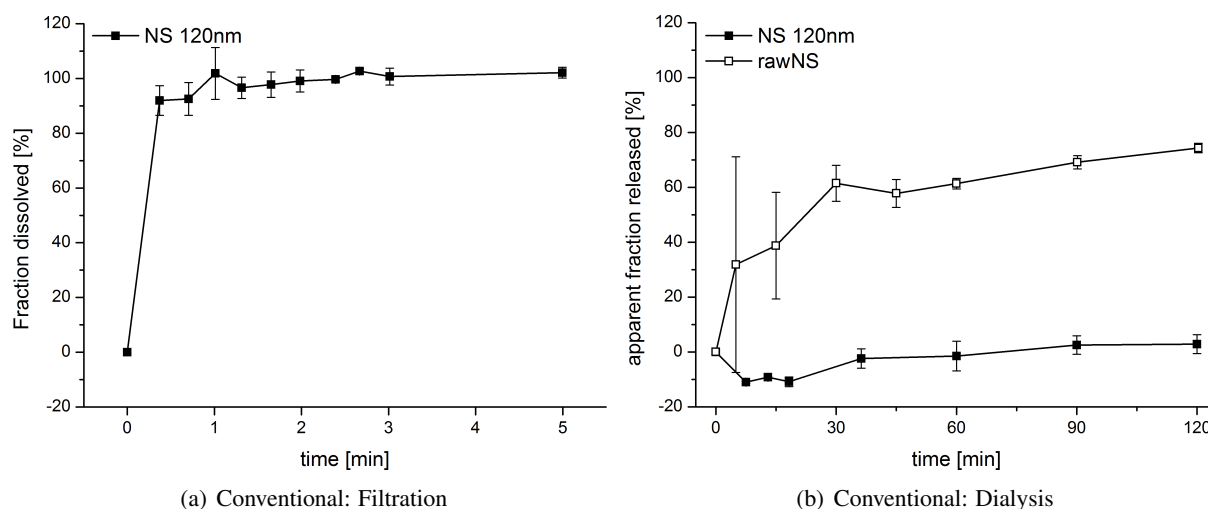(a) Conventional: Filtration   (b) Conventional: Dialysis

Figure 3.11: Dissolution of fenofibrate formulations in SGF + 0.1 % Tween 80 with conventional filtration and dialysis method. (a) Method: Paddle apparatus + sampling + filtration. FF concentration 5.5 µg/ml (n = 5). (b) Method: Paddle apparatus + dialysis membrane. NS 120nm vs coarse FF suspension (raw NS). FF concentration 207 µg/ml in the donor compartment (n = 3). The apparent fraction released is displayed, since the calculation of the fraction released is subject to various shortcomings as explained in section 3.5.2.

apparatus dissolution vessel (receiver). The idea was to quantify the undissolved fraction (donor) by withdrawal of samples from the donor compartment and to use this to calculate the dissolved fraction (receiver). This method would lead to correct estimates of the fraction dissolved under the assumption that the diffusion of dissolved API molecules across the dialysis membrane is fast and complete.

The fenofibrate nanosuspension NS 120nm and the coarse suspension raw NS were compared and the results can be found in Figure 3.11(b). The dissolution curves suggest that almost no API is released from NS 120nm whereas almost 60 % of API are released from the coarse suspension (raw NS) after 120 min. However, results should be interpreted very carefully, since the used setup has several shortcomings. Sampling from the donor compartment with a Hamilton syringe is difficult and especially for the suspension with larger particles no homogenious particle dispersion can be guaranteed during sampling. Consequently it is likely that erroneous concentrations are determinated from the donor compartment. Furthermore adsorption of particles or API to the dialysis cassette is likely and was not quantified. That almost no release from NS 120nm was seen could be attributed to an API membrane diffusion kinetics being much slower than the dissolution kinetics of the nanocrystals. Furthermore an API concentration manifold higher than the saturation concentration was used in the donor compartment. If a slow membrane diffusion of drug molecules is assumed, the sink condition in the donor compartment is likely to be violated.

Even though the experimental setup might be improved by applying a lower concentration in the donor compartment or by sampling from the receiver compartment, the problems of slow membrane diffusion kinetics and adsorption to the dialysis cassette would remain and heavily distort results. The dialysis setup was not further evaluated in this study. Similar results were reported by Heng et al. (2008).
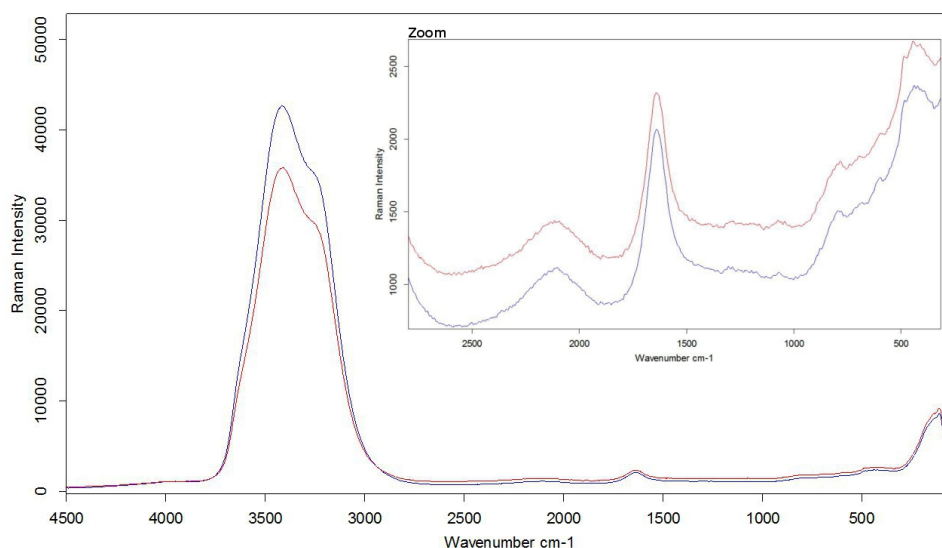
Figure 3.12: Raman spectra of dissolution medium SGF + 0.1 % Tween (red) and dissolution medium saturated with fenofibrate (black/blue). 3150-3640 cm^{-1}: O-H stretch band of water. 1150 cm^{-1}: C16-O3 stretching vibration, expected for fenofibrate but not detectable with the applied FF concentration $c = 8.7\mu g/ml$.

3.5.3 Noninvasive analytical techniques

Different noninvasive analytical techniques were evaluated for their feasibility to measure the dissolution of the fenofibrate nanosuspension NS 140nm in SGF + 0.1 % Tween 80.

Nuclear magnetic resonance spectroscopy and Raman spectroscopy

The idea to use spectroscopic techniques was to follow the transition of physical state of an API molecule during dissolution. The sensitivity of the analytical technique was the critical point about the applicability of spectroscopic techniques. Therefore it was tested if a fenofibrate signal from a saturated solution in the dissolution medium ($c = 8.7\mu g/ml$) could be seen. However, under the applied conditions no NMR or Raman spectroscopic signal of fenofibrate was detectable. The Raman spectra are presented in Figure 3.12. For fenofibrate a band at 1150 cm^{-1} assigned to the C16-O3 stretching vibration would be expected (Heinz et al. 2009). However, it was not visible in the saturated solution.

Pure medium and FF saturated medium produced identical NMR or Raman spectra. It was concluded that the applied techniques are not suitable to measure fenofibrate release from nanocrystals due to their too low sensitivity.

Nanoparticle tracking analysis

Nanoparticle tracking analysis (NTA) is a technique combining laser light scattering microscopy with a charge-coupled device camera. Individual particles can be tracked by the software and their particle size is calculated from the particle movement. Filipe et al. (2010) used this technique to characterize nanoparticles and highlights a high size resolution and sample visualization as the main advantages over

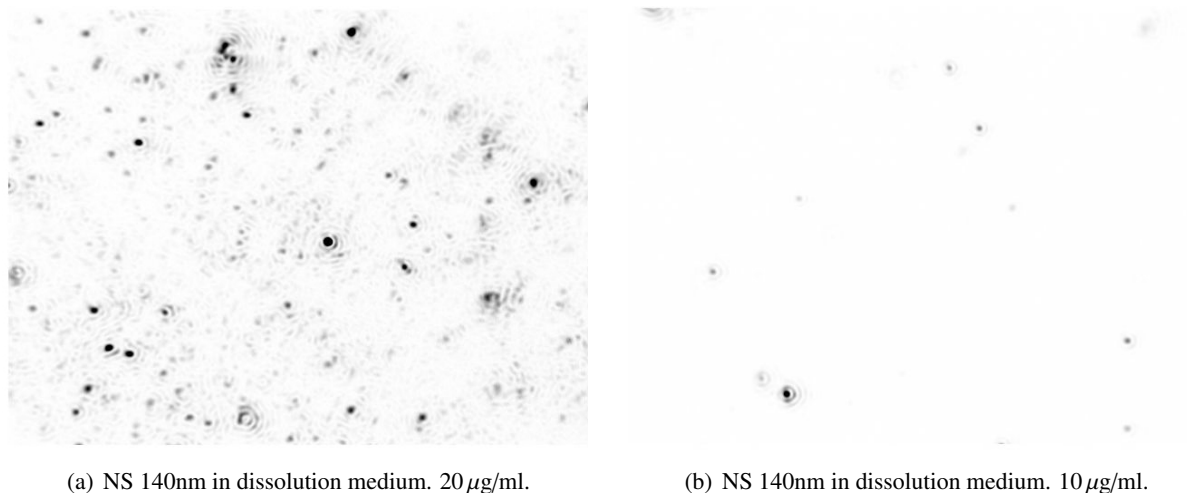(a) NS 140nm in dissolution medium. $20\,\mu g/ml$.   (b) NS 140nm in dissolution medium. $10\,\mu g/ml$.

Figure 3.13: Nanoparticle tracking analysis. Screen shots of videos of fenofibrate nanocrystals in dissolution medium. Original images were modified by inverting black/white color ($n = 1$).

dynamic light scattering. Drawbacks are a more difficult device handling requiring some operational skills and a high time-consumption.

At concentrations of $5 - 20\,\mu g/ml$ fenofibrate nanocrystals were visible and trackable. However, the characteristic particle number reduction during dissolution at concentrations $c < 8.7 \mu g/ml$ were not detectable with NTA, due to a too low particle number in the samples. Figure 3.13 gives an idea of the critically low particle numbers in these samples. In addition the filling and assembly of the sample chamber was too slow to enable a dissolution monitoring directly after sample dilution. A defined sample dilution directly in the assembled chamber was not possible. The applicability to a very narrow particle concentration range and a strong dependence of results on the applied measurement and analysis settings are inherent problems of the NTA technique. It was concluded that NTA is not suitable to measure nanocrystal dissolution within the requirements and conditions of this study.

Isothermal titration calorimetry

Isothermal titration calorimetry (ITC) is a thermodynamic method and measures the heat released or absorbed during various interactions or reactions. It is the method of choice for characterizing thermodynamics and stoichiometry of molecular interactions. In the pharmaceutical field it has been used to analyze cyclodextrin-guest interactions or micellar-based systems. The interested reader will find more examples reviewed by Bouchemal (2008). Calorimetric effects are also associated with particle dissolution and in this study it was evaluated whether ITC was capable of measuring this effect.

As a control experiment an aqueous stabilizer solution was injected into medium. No thermic reaction caused for example by mixing was observed. The injection of a nanosuspension into medium resulted in strong endothermic peaks (Fig 3.14). For subsequent injections the concentration gradient decreases and in parallel the heat absorbed (area under the peak) decreases. This is a promising result and a sound method development including thorough control measurements to account for phenomena like
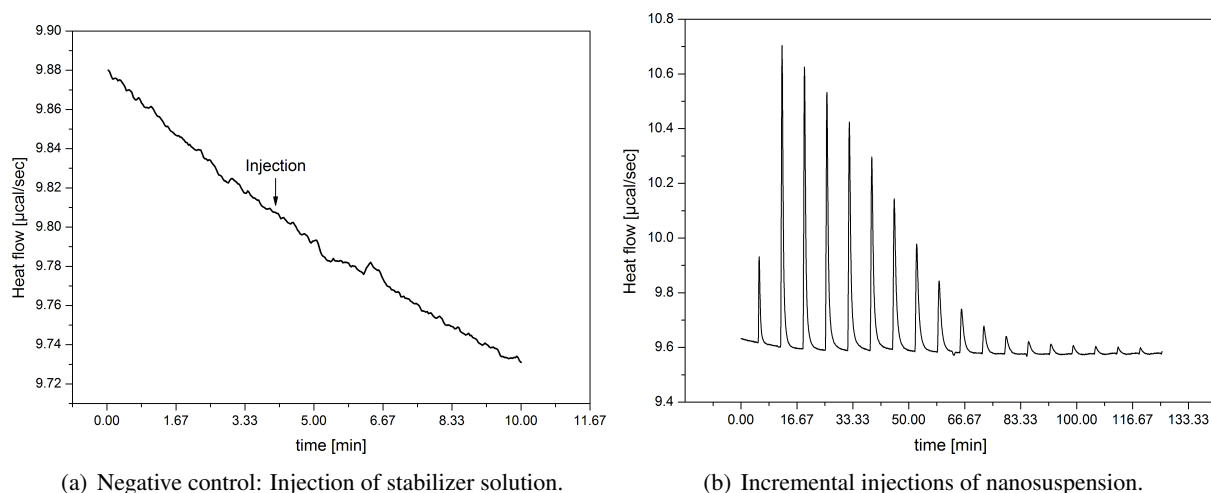
(a) Negative control: Injection of stabilizer solution.

(b) Incremental injections of nanosuspension.

Figure 3.14: Isothermal titration calorimetry. (a) Negative control: Injection of $35\,\mu$l of a diluted stabilizer solution into dissolution medium. (b) Injections of prediluted nanosuspension into dissolution medium. Preinjection of $3\,\mu$l followed by incremental injections of $10\,\mu$l. Each $10\,\mu$l injection corresponds to $2.4\,\mu$g FF and leads to incremental concentration increases of $1.7\,\mu$g/ml per injection ($n = 1$).

particle dilution/mixing, adsorption/desorption of surfactants/stabilizers to particles and micelle formation/reorganization could provide the basis to measure nanocrystal dissolution by ITC. However, in this study the focus was set on another approach, the light scattering dissolution assessment. The technical equipment was more simple and potentially offered a broader applicability than ITC.

3.5.4 Summary and conclusions

Conventional dissolution testing was successfully performed to measure fenofibrate and compound AS microsuspension dissolution. However, the conventional setup was not suitable to measure nanocrystal dissolution, neither with filtration nor with membrane diffusion applied for separation. Different non-invasive in situ analytical techniques avoiding the critical separation step were evaluated. Within the requirements and conditions of this study the spectroscopic methods and the nanoparticle tracking analysis were not suitable. The results of isothermal titration calorimetry applied to measure nanocrystal dissolution were promising. However, this technique was not further evaluated in favor of a light scattering approach, which is described in the next section.

3.6 Dissolution by light scattering

Parts of this section are published in Anhalt et al. (2012)

The measurement of nanocrystal dissolution by an approach of monitoring decreasing solid particle number and size based on light scattering allowed for a very fast data acquisition. The first data point was recorded 25 s after dilution and the interval of subsequent data points was 10 s. The scattering intensity, which is the primary measurement signal of each DLS measurement, was considered as readout parameter. The standard data output of DLS measurements, the hydrodynamic particle diameter, is derived from the intensity fluctuations by complex data analysis and exhibits a poor statistical quality for the extremely short measurement time of 2 s applied within this work (Brittain 2003).

Below an overview of important steps and control experiments leading to the final experimental setup will be presented (section 3.6.1). A comparative evaluation of the light scattering dissolution method to the conventional dissolution method was carried out (section 3.6.2 and 3.6.5). Subsequently the applicability of the new method will be demonstrated. For that purpose two sets of experiments were carried out to investigate suitability, reproducibility and sensitivity. In a first step the particle size was varied at a constant concentration; in a second step the concentration was varied keeping the particle size constant. All experiments were performed with FF and with AS nanosuspensions (sections 3.6.3 and 3.6.4). All results are summarized in Tables 3.4 and 3.5.

3.6.1 Method development

The mixing step directly before a measurement and the resulting fluid flow in the cuvette did not alter scattering intensity measurements (Fig. 3.15(a)).

The fenofibrate recovery from polystyrene and quartz glass cuvettes was determined in order to evaluate whether particle adsorption onto the cuvette walls appears. Particle adsorption would be critical, since adsorbed particles are not detected in scattering intensity measurements leading to incorrect estimates of solid/dissolved particle fractions. SGF + 0.1 % Tween 80 or FaSSIF were used as media and the fenofibrate nanosuspension NS 120nm was added at two concentration levels. Results are exemplarily displayed for SGF + 0.1 % Tween 80 (Fig 3.15(b)). API recoveries of $85 - 90$ % were determined under all tested conditions. In addition it was tested whether the cuvette material influences the dissolution profile and API recovery. No effect of cuvette material was observed (Fig. 3.15(b-d)). The use of a new cuvette compared to a reused cuvette did not make a difference (Fig. 3.15(d)). However, a difference would be expected in the case of relevant adsorption taking place, since the surfaces of used cuvettes would already be coated.

Good API recoveries and a no influence of cuvette material or reuse on dissolution curves disprove the assumption that particle adsorption might be responsible for the observed decreasing scattering profiles. It can be concluded that measured profiles can truly be attributed to particle dissolution characterized by a decreasing particle number and size. Disposable polystyrene cuvettes were selected for all further experiments.

(a) Fluid Flow

(b) FF recovery from cuvettes

(c) Influence of cuvette material on dissolution profile

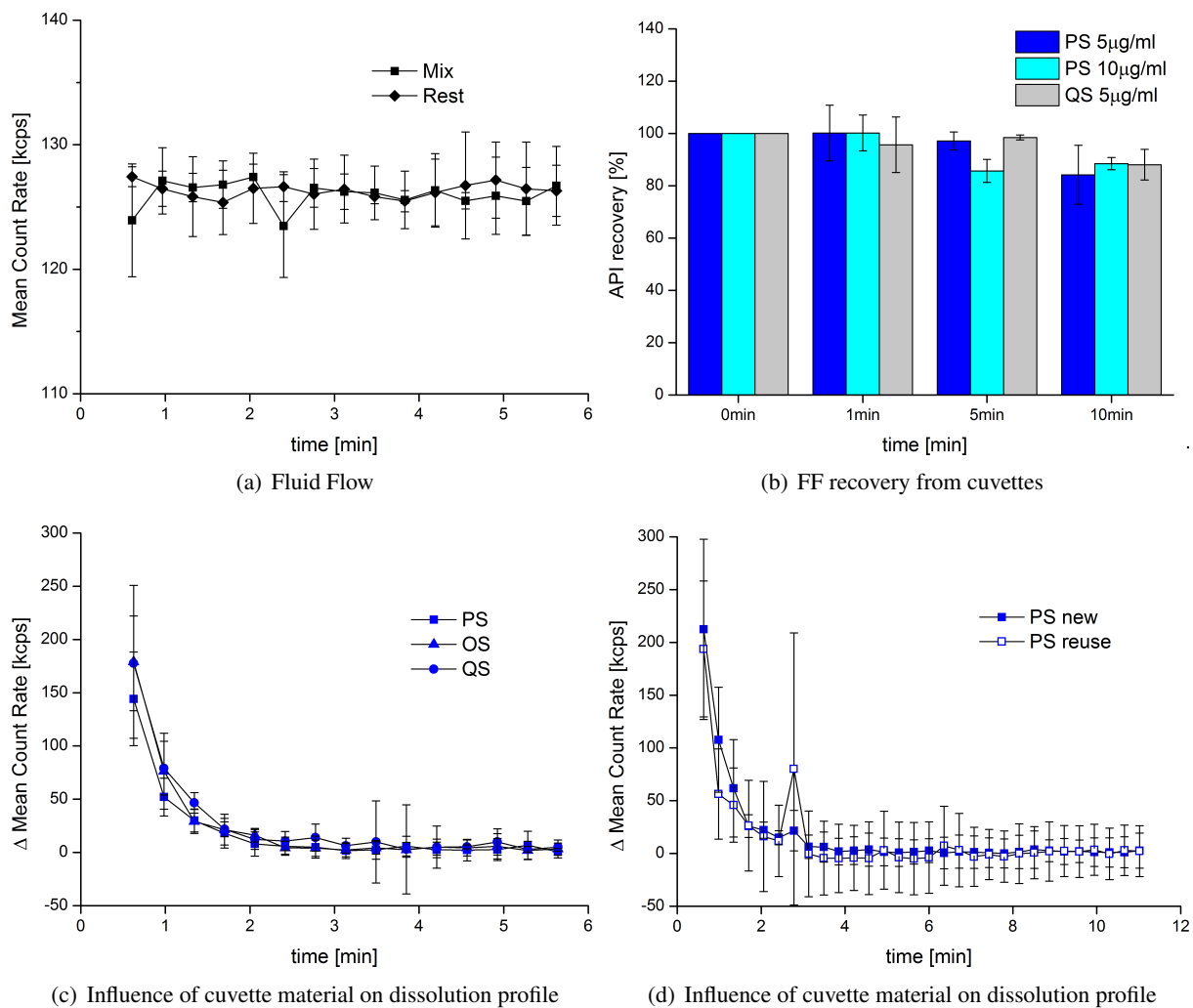(d) Influence of cuvette material on dissolution profile

Figure 3.15: Control tests during development of the light scattering dissolution setup. (a) Influence of fluid flow on light scattering measurement. (b) FF recovery under different conditions. (c,d) Dissolution of NS 120nm in SGF + 0.1 % Tween 80 under different conditions: (c) influence of cuvette material and (d) cuvette reuse. Cuvette types: PS = polystyrene disposable (standard equipment), OS = optical glass, QS = quarz glass ($n = 3$).

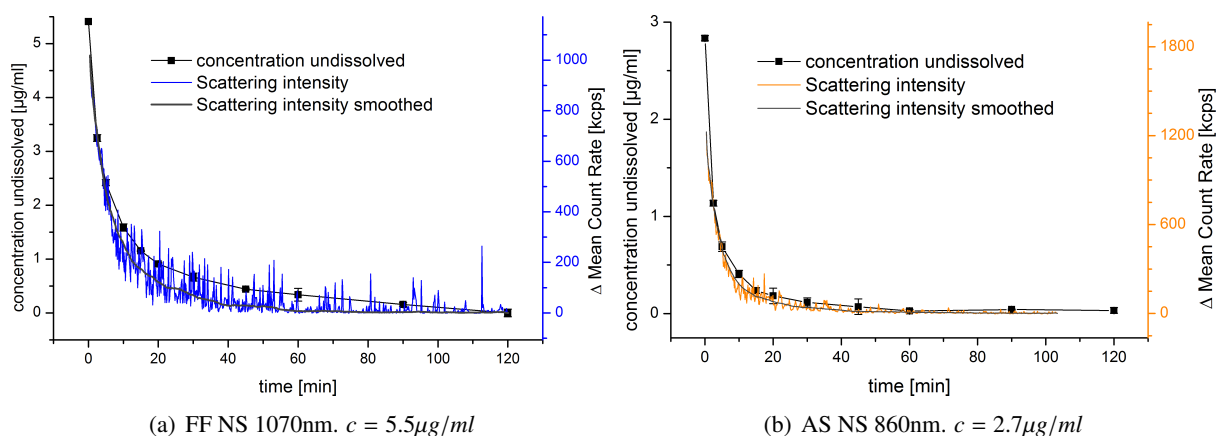(a) FF NS 1070nm. $c = 5.5 \mu g/ml$ (b) AS NS 860nm. $c = 2.7 \mu g/ml$

Figure 3.16: The dissolution of FF NS 1070nm and AS NS 860nm in simulated gastric fluid supplemented with 0.1% polysorbate 80. Black line: conventional method ($n = 3$). Blue and orange line: light scattering method ($n = 6$). Standard deviations not shown for clarity reasons. Grey lines: smoothed light scattering signal (running mean, 75 data points).

3.6.2 Comparison of light scattering and conventional dissolution method

For two nanosuspension a direct comparison of both techniques was made (Fig. 3.16). Overlays of both dissolution diagrams were designed by plotting the undissolved concentration determined by conventional paddle dissolution and the recorded scattering intensity determined by the scattering method. The resulting dissolution curves share the first data point at 2.5 min and the last data point at 120 min. The Y-axes were scaled so that the diagrams overlap at 2.5 min and 120 min. The values at time point 0 min could not be used to adjust the scales, because it was not possible to measure the scattering intensity at time 0 min.

The overlays illustrate a good correlation of both techniques. For FF NS 1070nm especially the initial high dissolution rate ($0 - 10$ min) is correlated very well (Fig. 3.16(a)). In the middle part ($10 - 60$ min) the dissolution process is slowed down and the scattering result has a decreasing tendency with many spikes. In the conventional experiment 92 % are dissolved after 60 min and the dissolution curve slowly approaches the level of complete dissolution. In the scattering result this process is indicated by a continuous reduction in the number of intensity spikes. The fluctuations of the scattering signal and the intensity spikes can be explained by number fluctuations in the scattering volume. Due to the small scattering volume and the decrease in particle concentration, when the dissolution process reaches its end, the probability of remaining particles to be detected is low. The spikes represent remaining undissolved particles passing the scattering volume, which probably belong to micron sized particle fractions. To optimize the comparability of both dissolution graphs a further step of data analysis was performed on the scattering diagram. The scattering intensity data were smoothed by the running mean algorithm with 75 data points.

For AS NS 860nm an overall good correlation of both techniques and a smoother scattering graph with less intensity spikes was observed (Fig. 3.16(b)). The nanosuspension NS 860nm (SLS $D90 = 1.3 \mu m$) is better suitable for a dissolution determination by the scattering method than the fenofibrate suspension

(a) Variation of size. $c = 5.5 \mu g/ml$.

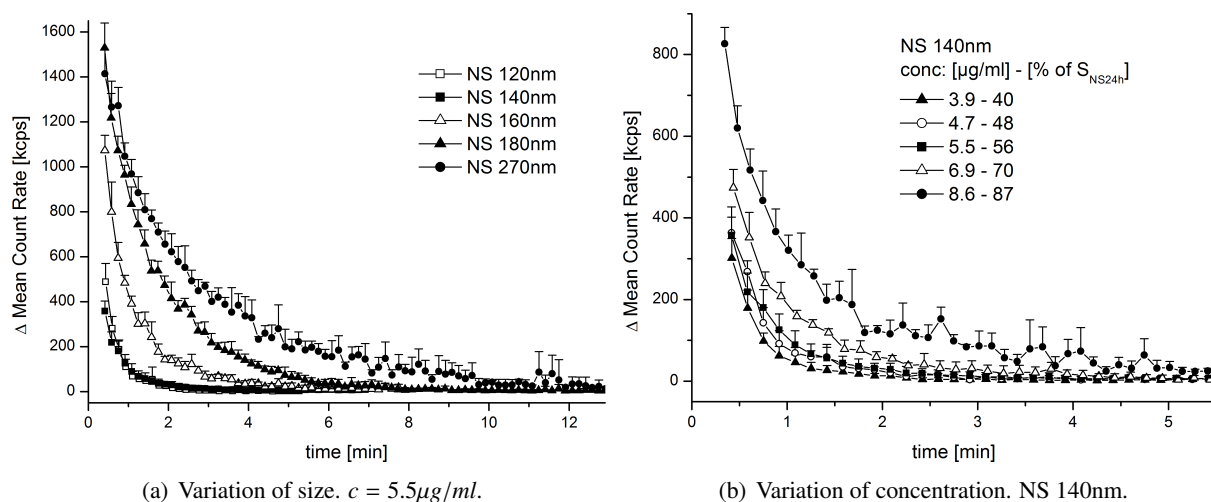(b) Variation of concentration. NS 140nm.

Figure 3.17: Fenofibrate nanocrystal dissolution measured by light scattering method. (a) Variation of particle size at fixed concentration. (b) Variation of concentration of NS 140nm. Concentrations given in $\mu g/ml$ and in % of the apparent solubility $S_{NS 140nm}$ ($n = 4$).

NS 1070nm (SLS $D90 = 2.1 \mu m$), due to its lower particle size and narrower size distribution. The applicability of the light scattering method and the preferred particle size range of suspensions will be discussed below (section 3.6.5).

Analysis of the FF and AS dissolution graphs by (bi-)exponential function fitting and calculation of DT (Table 3.4 and 3.5) shows a very good fit of the biexponential model ($R^2_{adjusted} = 0.995$ and 0.998) to the conventional dissolution graph compared to the exponential model ($R^2_{adjusted} = 0.930$ and 0.971).

For FF NS 1070nm a shorter dissolution time was derived from the scattering method as from the conventional method ($DT = 76 \pm 21$ min (scattering) and $DT = 132 \pm 8$ min (conventional)). This discrepancy is probably attributed to an inappropriate representation of the intensity spikes at advanced dissolution state by the applied evaluation method. For AS NS 860nm a smaller discrepancy in dissolution times was observed ($DT = 57 \pm 13$ min (scattering) and $DT = 40 \pm 6$ min (conventional)). The scattering method is more suitable for the smoother dissolution profiles of smaller particles and more appropriate dissolution times are calculated.

3.6.3 Fenofibrate nanocrystal dissolution

Figure 3.17(a) presents the experimental dissolution curves for NS 120nm to NS 270nm. From the Noyes-Whitney equation (Eq. 1.2) it is predicted that the smaller nanosuspensions with their higher surface area exhibit higher dissolution rates and therefore shorter dissolution times. In Figure 3.17(a) this dissolution time *vs* particle size ranking can be seen. For the sake of clarity results for bigger sized suspensions NS 650nm to NS 1070nm are not included in Figure 3.17(a). However, Figure 3.16(a) shows the dissolution curve of NS 1070nm. Table 3.4 summarizes the dissolution times for all formulations. The slower dissolution rates of NS 650nm to NS 1070nm can be explained by micron sized particle fractions present in this formulations ($D90 > 1 \mu m$, Tab. 3.1).

Table 3.4: Fenofibrate dissolution: Fitting of exponential (ExpDec1) and biexponential (ExpDec2) functions to dissolution curves and calculation of dissolution time (DT).

Experimental parameters			ExpDec 1 fitting		ExpDec 2 fitting	
Formulation	Concentration		$R^2_{adjusted}$	DT	$R^2_{adjusted}$	DT
	[$\mu g/ml$]	[$\%S_{NS}$]		[min]		[min]
Scattering method						
NS 140nm	3.9	40	0.975	1.5 ± 0.4	0.985	1.7 ± 0.3
	4.7	48	0.976	1.8 ± 0.3	0.981	2.2 ± 0.4
	5.5	56	0.983	2.2 ± 0.5	0.990	2.9 ± 1.1
	6.9	70	0.968	3.1 ± 0.3	0.977	3.4 ± 1.0
	8.6	87	0.932	5.1 ± 0.7	0.943	6.8 ± 0.6
NS 120nm	5.5		0.990	1.6 ± 0.1	0.993	1.9 ± 0.3
NS 140nm	5.5	56	0.983	2.2 ± 0.5	0.990	2.9 ± 1.7
NS 160nm	5.5		0.978	3.3 ± 0.3	0.984	4.7 ± 1.0
NS 180nm	5.5		0.987	6.3 ± 0.4	0.995	7.1 ± 0.7
NS 270nm	5.5		0.969	10.5 ± 0.6	0.974	12.3 ± 0.3
NS 650nm	5.5		0.827	15.3 ± 3.6	0.861	18.2 ± 1.2
NS 800nm	5.5		0.675	31.0 ± 5.4	0.698	60.3 ± 11.8
NS 1070nm	5.5		0.600	36.6 ± 6.2	0.623	76.4 ± 21.2
Conventional method						
NS 1070nm	5.5		0.930	43.3 ± 1.0	0.995	132.2 ± 8.4
MS 7.9μm	5.5		0.955	274.5 ± 6.6	0.996	439.0 ± 42.6

Figure 3.17(b) presents the experimentally obtained dissolution curves for different particle concentrations. For steeper concentration gradients higher dissolution rates and therefore shorter dissolution times are observed, which corresponds to the ranking as expected from the Noyes-Whitney equation. In pharmaceutical dissolution testing it is favored to minimize the concentration gradient effect by choosing sink conditions, which means that the total drug concentration C_0 is less than $10-30\%$ of saturation solubility C_S (Dressman et al. 1998; Jamzad and Fassihi 2006). For sink conditions the decrease in concentration gradient with increasing dissolved concentration can be neglected and the process can be regarded as only dependent on the constant C_S. However, in the presented experiment concentrations above 30% of apparent nanosuspension solubility are analyzed. Due to the rapid process of nanocrystal dissolution, too few data points for dissolution under sink conditions were obtained for a satisfying data interpretation. Table 3.4 summarizes the results of the fitting of (bi-)exponential models to experimental dissolution graphs and the calculated dissolution times. In general the tendency for a slightly better fit of ExpDec2 (Eq. 2.2) was observed. The function fitting to dissolution curves of bigger sized suspensions (NS 650nm - NS 1070nm) and of higher concentrations ($8.6\,\mu g/ml$) resulted in lower coefficients of determination. However, this should not necessarily be interpreted as a poor correlation, since the relatively high noise of these dissolution curves (Fig. 3.16(a), blue line) inevitably results in high deviations between the measured signal and the fitted curve.
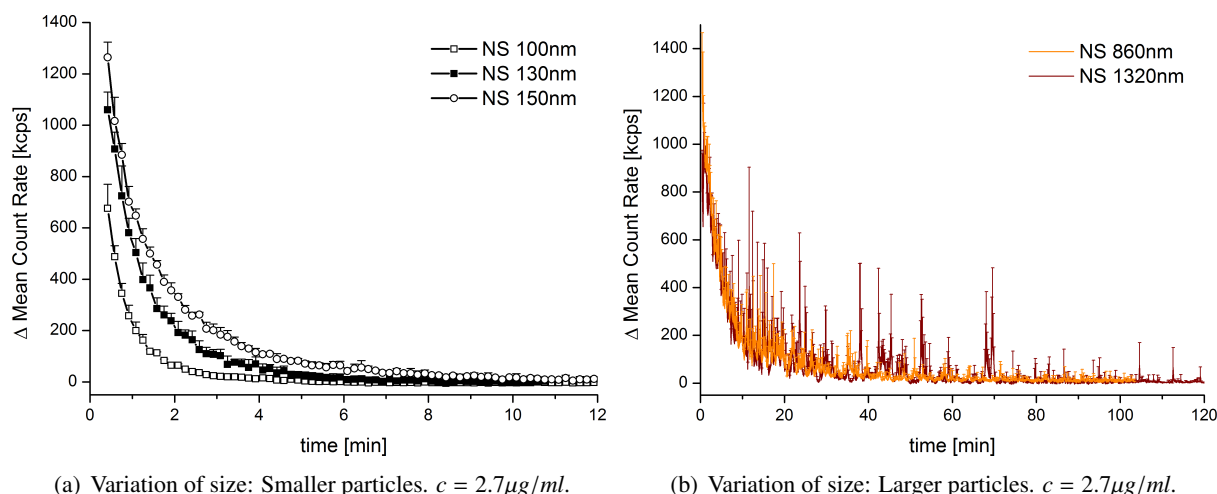
(a) Variation of size: Smaller particles. $c = 2.7 \mu g/ml$.

(b) Variation of size: Larger particles. $c = 2.7 \mu g/ml$.

Figure 3.18: Compound AS nanocrystal dissolution measured by light scattering method. Variation of particle size ($n = 4$).

3.6.4   Compound AS nanocrystal dissolution

Table 3.5 summarizes the results of the fitting of (bi-)exponential models to experimental dissolution graphs and the calculated dissolution times. All observations made for the dissolution of AS formulations are the same for the FF formulations: A clear ranking with the shortest dissolution times for the smallest particles and the lowest concentrations was observed. Smoother dissolution profiles are achieved for the smaller sized suspensions and the lower concentrations. All dissolution data are presented in Figure 3.18 and Figure 3.19.

3.6.5   Nanocrystal dissolution by light scattering method: Discussion

It was demonstrated that the light scattering method is applicable to measure the dissolution of nanosuspensions. The preferred nanocrystal size is in the lower nanometer range (mean particle size < 500 nm). For very short dissolution times (DT < 1.5 min) the 25 s interval between dilution and first data point might lead to a insufficient number of collected data points, which limits the applicability for extremely rapid processes. In the upper nanometer range (500 − 1000 nm) it was possible to measure dissolution with the applied setup although the method is less suitable with increasing particle size fractions in the lower micron scale.

Compared to the conventional method, in which dissolved concentrations are measured quantitatively, the light scattering setup primarily provides relative dissolution profiles. When the scattering intensity approaches a constant level, it can be concluded that the number and size of particles are at a constant level, but information about the amount of undissolved drug cannot be derived directly. In this study for all samples at the end of the dissolution process a $\Delta MeanCountRate$ of 0 ± 10 kcps was reached (Fig. 3.17). This indicates that light was scattered only by the micelles of the dissolution medium and not by nanocrystals. A DLS size measurement at the end of each dissolution experiment confirmed that apart from micelles no particles were detectable. Thus it was possible to add quantitative information

(a) NS 100nm: lower concentrations

(b) NS 100nm: higher concentrations

(c) NS 150nm: lower concentrations

(d) NS 150nm: higher concentrations

(e) NS 860nm: lower concentrations
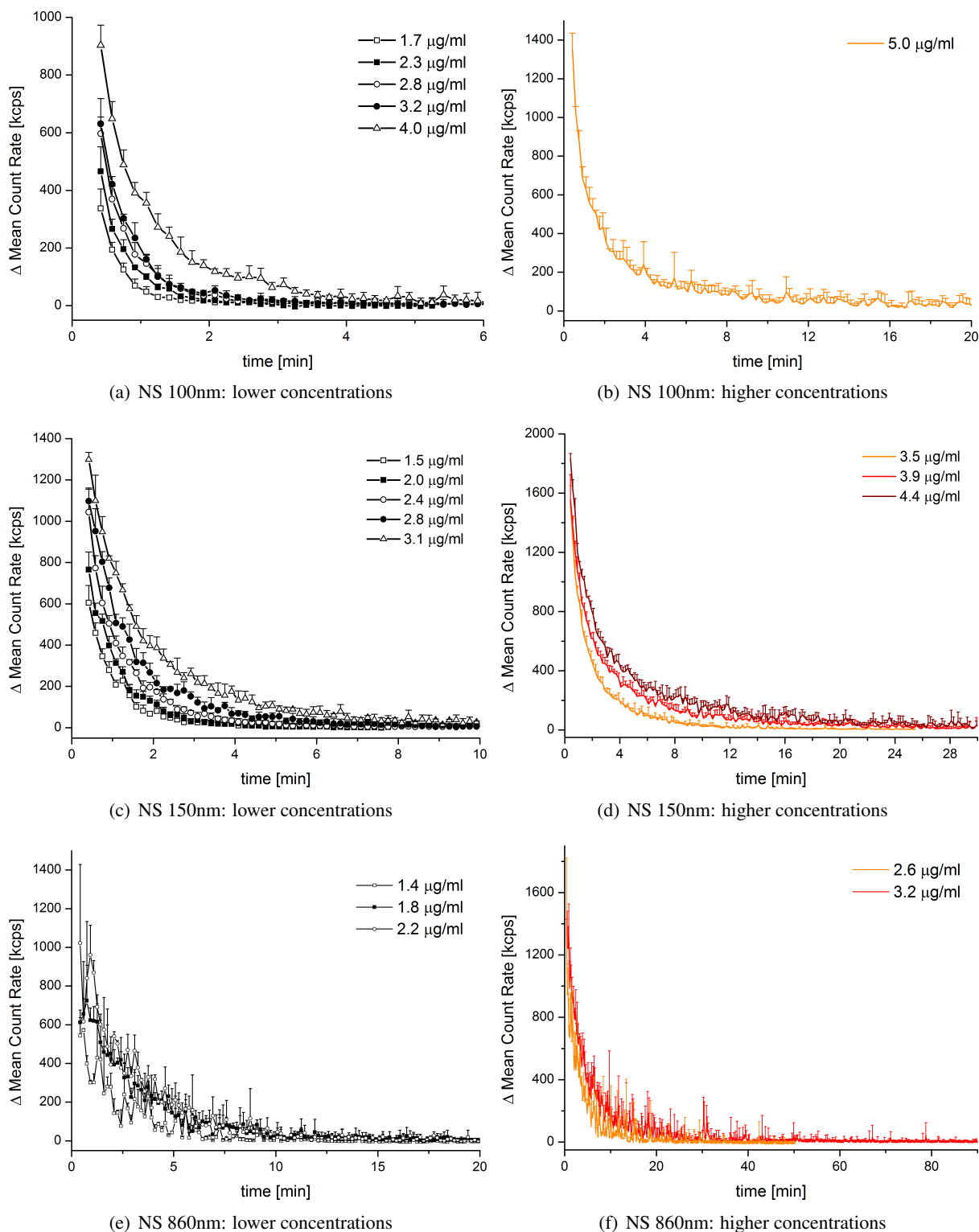
(f) NS 860nm: higher concentrations

Figure 3.19: Compound AS nanocrystal dissolution measured by light scattering method. Variation of concentration. The dissolution curves for each formulation are displayed in two separate panels to provide a better overview ($n = 4$).

Table 3.5: Compound AS dissolution: Fitting of exponential (ExpDec1) and biexponential (ExpDec2) functions to dissolution curves and calculation of dissolution time (DT).

Experimental parameters			ExpDec 1 fitting		ExpDec 2 fitting	
Formulation	Concentration		$R^2_{adjusted}$	DT	$R^2_{adjusted}$	DT
	$[\mu g/ml]$	$[\%S_{NS}]$		[min]		[min]
Scattering method						
NS 100nm	1.7	30	0.979	1.4 ± 0.1	0.983	1.4 ± 0.2
	2.3	40	0.978	2.0 ± 0.4	0.979	2.2 ± 0.4
	2.8	48	0.982	2.0 ± 0.2	0.990	2.4 ± 0.7
	3.2	56	0.986	2.2 ± 0.4	0.989	2.6 ± 0.4
	4.0	70	0.973	3.5 ± 0.4	0.987	4.5 ± 1.0
	5.0	87	0.922	7.2 ± 0.5	0.965	14.1 ± 4.5
NS 150nm	1.5	30	0.972	3.2 ± 0.4	0.980	3.0 ± 0.6
	2.0	40	0.988	3.6 ± 0.4	0.989	4.1 ± 0.1
	2.4	48	0.983	3.8 ± 0.3	0.990	3.9 ± 0.9
	2.8	56	0.984	4.9 ± 0.2	0.987	7.2 ± 1.6
	3.1		0.984	6.6 ± 0.6	0.991	9.2 ± 1.2
	3.5	70	0.973	6.5 ± 0.5	0.989	9.3 ± 2.4
	3.9		0.960	11.8 ± 1.2	0.987	18.9 ± 3.2
	4.4	87	0.949	13.2 ± 0.9	0.981	22.4 ± 3.1
NS 860nm	1.4	30	0.817	10.1 ± 1.1	0.842	10.7 ± 0.2
	1.8	40	0.928	13.4 ± 0.9	0.925	14.0 ± 0.9
	2.2	48	0.910	12.7 ± 1.2	0.903	12.9 ± 1.7
	2.6	56	0.894	14.6 ± 1.9	0.907	36.9 ± 10.5
	3.2	70	0.927	20.2 ± 1.1	0.937	36.9 ± 3.1
	4.0	87	0.673	68.1 ± 29.7	0.720	164.5 ± 15.4
NS 100nm	2.7	47	0.984	2.7 ± 0.3	0.995	3.0 ± 1.8
NS 130nm	2.7		0.984	4.4 ± 0.3	0.988	5.9 ± 0.8
NS 150nm	2.7	54	0.984	6.0 ± 0.1	0.996	7.8 ± 0.5
NS 860nm	2.7	59	0.898	23.7 ± 1.6	0.913	57.4 ± 13.0
NS 1320nm	2.7		0.755	29.6 ± 4.9	0.757	86.4 ± 30.6
Conventional method						
NS 860nm	2.7		0.971	15.1 ± 0.2	0.998	39.6 ± 5.7
MS 3.4μm	2.7		0.876	148.0 ± 9.6	0.988	369.7 ± 27.7
MS 6.8μm	2.7		0.745	340.5 ± 25.4	0.975	603.7 ± 74.7

regarding the end of the process.

In this study a linear correlation of scattering signal and particle concentration was shown exemplarily (section 3.3.1). This allowed the simplified assumption that during dissolution decreasing scattering intensity corresponds to decreasing particle concentration. However, scattering depends not only on particle concentration, but also on size (section 1.3). To deal with the effect of differences in scattering patterns of different sized nanocrystal formulations the comparison of their dissolution profiles was done on the basis of a relative dissolution endpoint (time when 1% of initial scattering intensity remains). The influence of absolute differences in scattering intensity between formulations on data interpretation was minimized by this approach. The applied interpretation is valid under the assumption that a change in scattering intensity during dissolution is dominated by the reduction in particle number. Consideration of particle shrinking or alterations in particle size distribution would require more complex data analysis. A similar method to assess small particle dissolution was introduced by Tucker (2002) and Crisp et al. (2007), who used turbidimetric measurements at an angle of 0° to monitor dissolution of particles with sizes of $0.24 - 5\,\mu$m. An interesting approach was chosen by starting the dissolution process by the addition of surfactants (and a resulting increase in solubility) during the measurement. This procedure enables a determination of the initial absorbance of undissolved particles. Crisp developed a model for the solid mass decay and regarded the particle dissolution process as the shrinking of a sphere. For the case of scattering intensity being proportional to the particle volume he modified his mass decay model towards a turbidity decay model. Both, the dissolution and turbidity based models fit experimental curves well and it is concluded, that 'the assumption that turbidity scales as particle volume fraction (concentration) produces reasonable accuracy' (Crisp et al. 2007).

Tucker (2002) reported dissolution times shorter than 60 s for naproxen nanosuspensions (266 nm and 656 nm; concentration of about 15 % of the equilibrium solubility). The same author described that danazol nanosuspensions (Mean 356 nm and 820 nm, 40 % of the equilibrium solubility) dissolve in aqueous sodium lauryl sulfate solution in about 150 s. Crisp came to a similar result (< 120 s) for danazol nanosuspensions (D50 300 nm and 400 nm, 10 % of the equilibrium solubility) in aqueous sodium lauryl sulfate solution (0.3 wt %) (Crisp et al. 2007). On the other hand the dissolution time for an itraconazole nanosuspension (D50 240 nm, 10 % of the equilibrium solubility) was found to be 60 min, which is explained by a lower micellar solubility and a lower rate constant of interfacial reaction for the bigger and more lipophilic itraconazole molecules. The dissolution time for the fenofibrate nanosuspension NS 140nm (D50 130 nm, 40 % of solubility $S_{NS\,24h}$) of 91 s / 101 s (ExpDec1 / ExpDec2) stated in this study fits well into the range given by Tucker and Crisp.

3.6.6 Data evaluation according to the Noyes-Whitney dissolution model

Theory

The Noyes-Whitney dissolution model describes the dissolution process as being determined by diffusion of dissolved molecules through the diffusion layer adjacent to the solid surface. In strict interpretation its validity is limited to a constant surface area, a bulk concentration being considerably lower than the solubility of the API and to surfactant free dissolution media. In practice the Noyes-Whitney model

has been successfully applied to model dissolution curves, which were obtained under experimental conditions where not all of the above mentioned criteria were fulfilled (Tinke et al. 2005; Gao 2011; Dokoumetzidis et al. 2006). This indicates the usefulness of the model even under non perfect conditions and motivated the use of the Noyes-Whitney equation as a first approach in this study. For that purpose the Hixson and Crowell equation was used, which is a transformation of the Noyes-Whitney equation Eq. 1.2 (Costa and Sousa Lobo 2001).

$$W_d = VC_S(1 - e^{-Kt}) \tag{3.1}$$

W_d is the mass dissolved, C_S the saturation solubility, V the volume of dissolution medium, t the time and K is a coefficient with

$$K = \frac{DA_0}{hV} \tag{3.2}$$

where D is the diffusion coefficient, A_0 is the total surface area and h is the effective boundary layer thickness. The total initial surface area A_0 of the suspensions is estimated with following assumptions: (1) Particles have a spherical shape and the radius r. (2) Particle size distributions are neglected. (3) Due to the extremely poor solubility of the considered APIs it is neglected that the aqueous medium is saturated with dissolved API. All drug substance is considered to be in the solid nanocrystalline state. (4) The densities ρ of crystalline drug substance was predicted by I-Lab 2.0 software (ACD/Labs, Toronto, Canada) (Tab. 2.1). (5) As an approximation the shrinking of particles and the change of surface area during the dissolution process were not taken into account.

$$A_0 = N * A_P = \frac{V_0 A_P}{V_P} = \frac{W_0}{\rho} \frac{3}{r} \tag{3.3}$$

N represents the number of particles, V_0 and W_0 the total volume and mass of particles and V_P and A_P the volume and surface area of an individual particle. Equation 3.1 is transformed by applying logarithms and by substituting $W_S = VC_S$ and $Wd = W_0 - W_u$ (W_0 is the total drug amount and W_u is the undissolved drug mass):

$$ln\frac{W_u + (W_S - W_0)}{W_S} = -Kt \tag{3.4}$$

$W_S - W_0$ is the gradient ΔW. The time, when dissolution terminates DT is characterized by $W_u = 0$. The total drug concentration is C_0 ($C_0 = W_0/V$). Eqs. 3.5 and 3.6 can be obtained by transformation of Eq. 3.4 and insertion of Eqs. 3.1, 3.2 and 3.3:

$$DT = -ln\frac{\Delta W}{W_S} \frac{1}{K} = -ln\frac{W_S - W_0}{W_S} \frac{hV}{DA_0} = -ln\frac{C_S - C_0}{C_S} \frac{h\rho r}{3DC_0} \tag{3.5}$$

$$-ln\frac{\Delta W}{W_S} \frac{V}{A_0} = kDT \tag{3.6}$$

Eq. 3.6 denotes that the $-ln(\Delta W/W_S) * V/A_0$ vs DT diagram has a slope of $k = D/h$, where k is the dissolution rate constant and where the y-intercept is zero.
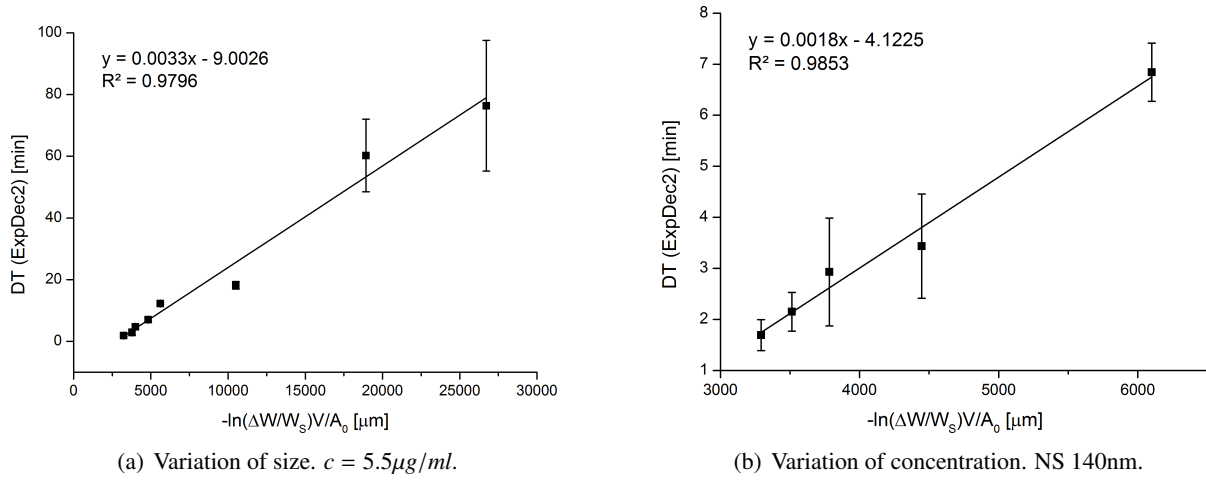
(a) Variation of size. $c = 5.5 \mu g/ml$.

(b) Variation of concentration. NS 140nm.

Figure 3.20: Fenofibrate: Plot of dissolution times $DT \; vs \; -ln(\Delta W/W_S) * V/A_0$. Dissolution times were experimentally determined by light scattering dissolution method and fitting of the biexponential model. (a) The data points (from left to right) denote dissolution results of NS 120nm, NS 140nm, NS 160nm, NS 180nm, NS 270nm, NS 650nm, NS 800nm and NS 1070nm. (b) The data points (from left to right) denote dissolution results of concentrations 40 %, 48 %, 56 %, 70 % and 87 % of $S_{NS\,140nm}$.

Application of the Noyes-Whitney dissolution model to experimental data

Figure 3.20(b) shows the $DT \; vs \; -ln(\Delta W/W_S) * V/A_0$ diagram for the dissolution of FF NS 140nm at different concentrations and the result of linear regression. From the reciprocal slope a dissolution rate constant of $9.4 * 10^{-4}$ cm/s is derived. For the experimental data an offset was observed, thus for the linear regression analysis the y-intercept was not forced to be zero (discussed in section 3.6.6).

Figure 3.20(a) shows the $DT \; vs \; -ln(\Delta W/W_S) * V/A_0$ diagram for the dissolution of different fenofibrate formulations at a constant concentration and the result of linear regression. Here for the calculation of the term $-ln(\Delta W/W_S) * V/A_0$ differences in the nanosuspension solubilities (S_{NS} or W_S) were not considered, since their contribution to the term $-ln(\Delta W/W_S) * V/A_0$ is small compared to the contribution of particle size. Instead as an approximation the value of $S_{NS\,24h}$ for NS 140nm (Tab. 3.3) was assumed for all calculations. From the reciprocal slope a dissolution rate constant of $5.1 * 10^{-4}$ cm/s is derived, which is in a similar range as determined by variation of concentration.

Figure 3.21 summarizes the application of the Noyes-Whitney model to the dissolution results of compound AS formulations. Again the particle size and the concentration gradient were varied. From the variation-of-size experiment a dissolution rate constant of $17.5 * 10^{-4}$ cm/s is derived. The variation-of-concentration experiment was performed for three formulations and the same result was found for all formulations: The dissolution rate constant is $5.3 * 10^{-4}$ cm/s.

Data evaluation according to the Noyes-Whitney dissolution model: Discussion

The Noyes-Whitney model describes the fundamental principles of diffusion controlled dissolution and has been applied for basic and advanced dissolution modeling extensively. In this work as a first approach it proved to be useful to check plausibility of experimental data and to gain some mechanistic insight.
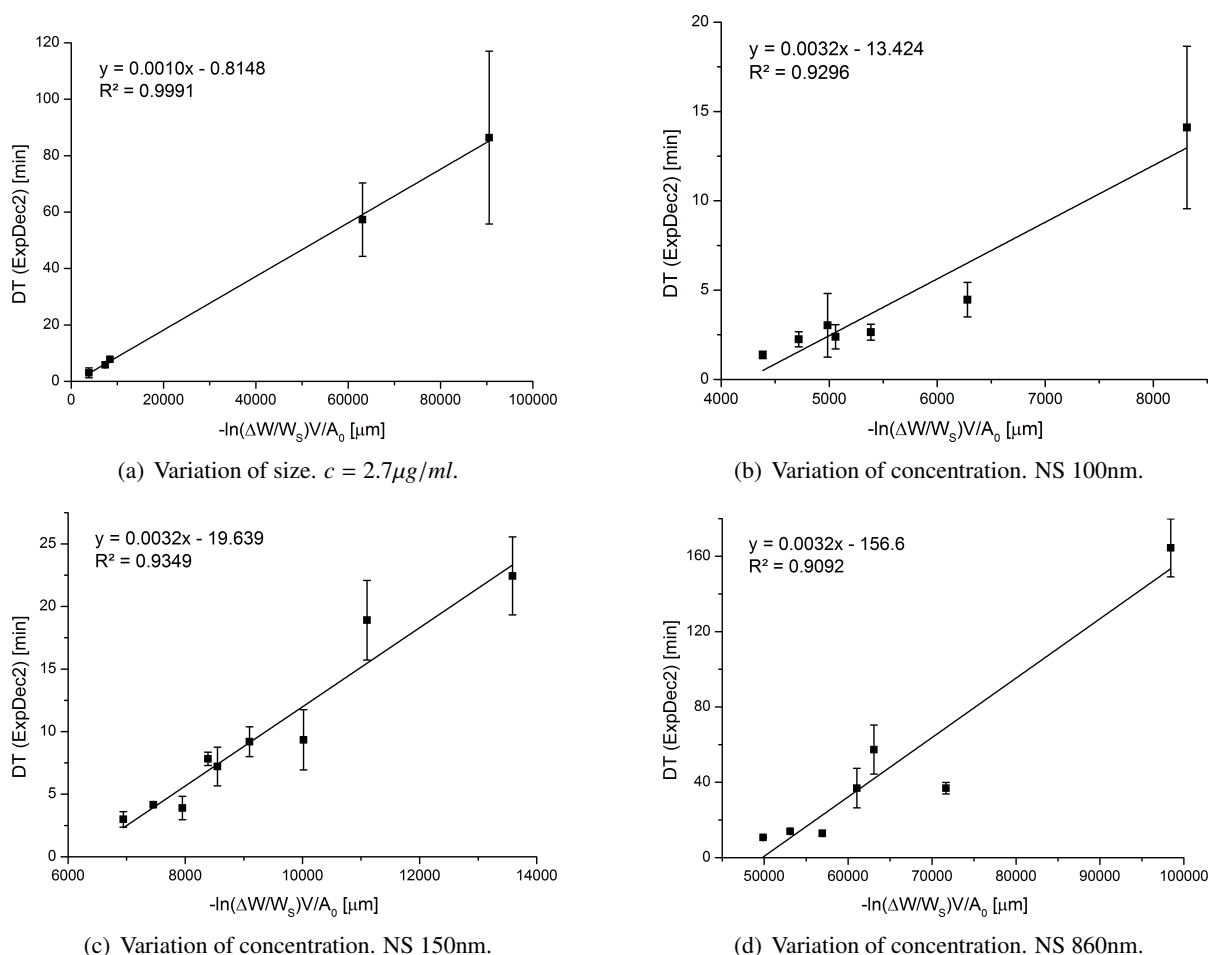
(a) Variation of size. $c = 2.7 \mu g/ml$.

(b) Variation of concentration. NS 100nm.

(c) Variation of concentration. NS 150nm.

(d) Variation of concentration. NS 860nm.

Figure 3.21: Compound AS: Plot of dissolution times DT vs $- ln(\Delta W/W_S) * V/A_0$. Dissolution times were experimentally determined by light scattering dissolution method and fitting of the biexponential model. (a) The data points (from left to right) denote dissolution results of NS 100nm, NS 130nm, NS 150nm, NS 860nm and NS 1320nm. (b) The data points (from left to right) denote dissolution results of concentrations 30 %, 40 %, 47 %, 48 %, 56 %, 70 % and 87 % of $S_{NS\,100nm}$. (c) The data points (from left to right) denote dissolution results of concentrations 30 %, 40 %, 48 %, 54 %, 56 %, 61 %, 70 %, 76 % and 87 % of $S_{NS\,150nm}$. (d) The data points (from left to right) denote dissolution results of concentrations 30 %, 40 %, 48 %, 56 %, 59 %, 70 % and 87 % of $S_{NS\,860nm}$.

By transformation of the Noyes-Whitney equation a linear relation between the dissolution time DT and the term $-ln(\Delta W/W_S) * V/A_0$ was obtained.

In accordance with the Noyes-Whitney model a linear relation DT vs $-ln(\Delta W/W_S) * V/A_0$ was observed for a wide concentration range of fenofibrate and compound AS dissolution – although nonsink conditions were applied. This observation suggests that the sink classification might be of minor relevance for the dissolution of crystalline nanosuspensions. Their outstanding characteristic, an enhanced surface area, appears to predominate over the influence of concentration gradient in the Noyes-Whitney model. A linear relationship could also be demonstrated for the variation of particle size, despite the assumptions made in the calculation of total initial surface area A_0 and despite the disregard of solubility dependence on particle size.

Fenofibrate dissolution rate constants of $9.4 * 10^{-4}$ cm/s (variation concentration) and of $5.1 * 10^{-4}$ cm/s (variation particle size) were calculated. Compound AS dissolution rate constants of $5.3 * 10^{-4}$ cm/s (variation concentration) and of $17.5 * 10^{-4}$ cm/s (variation particle size) were calculated respectively. We assume that the dissolution rate constants calculated from dissolution at different concentrations are more reliable, since assumptions are made for the calculation of the surface area (e.g. sphericity of particles and disregard of polydispersity). The error deriving from this is constant when a single suspensions is diluted to different concentrations but varies between different formulations (variation-of-particle-size experiments). Nevertheless all values are in a similar range, which means that the dissolution of the investigated systems seem to follow a similar mechanism regardless of changes in particle size or concentration. The determined dissolution rate constants fit well into the range given by Crisp et al. (2007), who calculated effective dissolution rate constants of $6 - 357 * 10^{-4}$ cm/s. This comparison confirms that the applied method and data evaluation lead to reliable results. However, for the interpretation of results it is important to mention that neither particle shrinking nor associated changes of effective boundary layer or solubility during dissolution are considered (Galli 2006; Judefeind and Villiers 2009). The applied method therefore yields an averaged value for the dissolution rate constant over the entire time of the process.

Shortcomings are associated with the determination of dissolution rate constants in this study and might explain the observed y-offset in our data (Fig. 3.20 and 3.21). From the experimental point of view two arguments could be stated. On the one hand for small particle sizes or low concentration gradients the loss of dissolution information during the first 25 s might influence data interpretation essentially. On the other hand for bigger particle sizes the applied data evaluation method might have the tendency to underestimate dissolution times (discussed in section 3.6.2). From the theoretical point of view the choice of the basic Noyes Whitney dissolution model could be discussed. The Noyes-Whitney equation neither takes into account particle size distributions, nor changes in particle size, surface area, diffusion layer thickness or particle solubility during the dissolution process. For that purposes more complex models of particle dissolution are available (Johnson 2012). Furthermore, the general suitability of diffusion controlled models (like the Noyes-Whitney model) for nanoparticle dissolution has been discussed in literature (Crisp et al. 2007; Judefeind and Villiers 2009). It has been proposed that for nanoparticle dissolution the rate limiting process is not diffusion of dissolved molecule into the bulk solution. Instead the prior solvation step at the solid-liquid interface (the dissociation of drug molecules from the solid)

Table 3.6: Prediction of dissolution data by extrapolation of the Noyes-Whitney evaluated nanocrystal dissolution data.

Formulation	Measured DT [min]	Predicted DT [min]	Deviation[*]
FF MS 7.9μm	439	588	+33 %
AS MS 3.4μm	370	236	−36 %
AS MS 6.8μm	604	316	−48 %

[*] $Deviation = (PredictedDT - MeasuredDT)/MeasuredDT * 100\%$

becomes more important for the dissolution process. However, in spite of various simplifications, an approach using the Noyes-Whitney model seems to enable a description of the dissolution process of nanocrystals in a meaningful way.

3.6.7 Are nanocrystal dissolution data recorded by the light scattering method predictive for microcrystal dissolution?

It was tested if the linear relations between term $-ln(\Delta W/W_S) * V/A_0$ and the dissolution time DT measured by light scattering of nanocrystals (Fig. 3.20 and 3.21) were predictive for the dissolution times of microcrystals (Fig. 3.5.1). However, the success of this approach was limited as can be seen in Table 3.6. The points discussed in section 3.6.6 regarding experimental and theoretical considerations might be reasons for the missing predictive strength of the applied approach. Shortly differences between the experimental method on the one hand and between the mechanism of dissolution on the other hand might be responsible.

3.6.8 Application to a market drug product

So far in this chapter dissolution measurements on nanosuspensions have been presented. However, in general nanosuspensions are further processed in order to yield a market product based on nanocrystals. EMEND® 80 mg capsules are one example of a nanocrystal based market product of the API aprepitant. Aprepitant nanosuspensions are manufactured by wet milling and by a column-coating process coated beads are generated. The pellets are then filled into a gelatin capsule (Olver et al. 2007).
The feasibility of the light scattering dissolution method to monitor dissolution of nanocrystals released from EMEND® pellets was evaluated. Since the formulation contains the undissolvable excipient microcrystalline cellulose, which disturbs light scattering measurements, a filtration step was added to the dissolution protocol. In the predilution step pellets were dispersed and after filtration a stable nanoparticulate dispersion resulted (DLS Z average 203nm, PDI 0.177). This dispersion was finally diluted to a concentration lower than saturation concentration and it was possible to monitor nanocrystal dissolution by the light scattering setup (Fig. 3.22). For aprepitant concentrations $45 - 50\,\mu$g/ml a complete nanocrystal dissolution was observed, with a dissolution time depending on concentration. For the concentration $55\,\mu$g/ml dissolution was much slower, which indicated that this concentration is close to the saturation level of aprepitant in the dissolution medium. The saturation concentration could not be measured, since
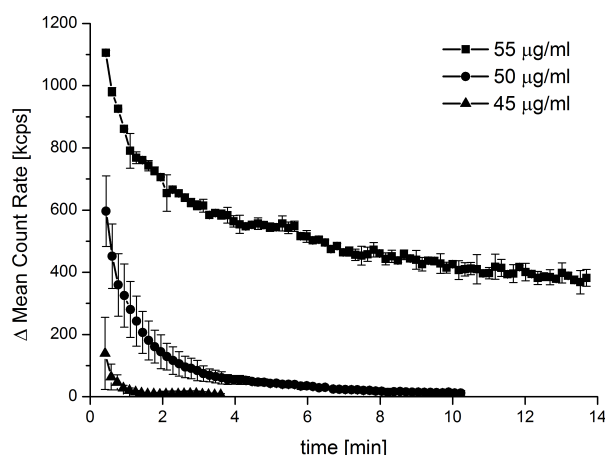
Figure 3.22: EMEND® nanocrystal dissolution in SGF + 0.1 %Tween 80 at different API concentrations followed by light scttering intensity measurements ($n = 3$).

the API aprepitant is not commercially available and is protected by a patent. However, the proposed estimate fits well into the range of aprepitant solubility published by Shono et al. (2010).

It was demonstrated that the light scattering based nanocrystal dissolution method was applicable to a market product. The removal of undissolvable excipients by filtration at the predilution level was a successful strategy to enable nanocrystal dissolution measurements by means of light scattering intensity monitoring. However, this experiment should merely be regarded as a preliminary study, since only one market formulation has been tested.

3.6.9   The use of the biorelevant dissolution medium FaSSIF

It was evaluated whether the use of the dissolution medium fasted-state simulated intestinal fluid (FaSSIF) was possible within the light scattering dissolution setup. The mixed micelles present in FaSSIF have clearly stronger light scattering properties than the Tween micelles in the standard medium SGF + Tween. At the standard attenuator setting 10 the scattering intensity of FaSSIF was approximately 4000 kcps. Since this is outside the linear range (section 3.3.1) the attenuator setting 7 was chosen. At attenuator 7 the scattering intensity of the used FaSSIF batch was 169 ± 5 kcps. It was possible to measure fenofibrate NS 140nm dissolution curves in FaSSIF (Fig. 3.23). Dissolution curves at different concentrations could be correctly ranked. The $\Delta MeanCountRate$ values were clearly lower compared to values measured with SGF + Tween as dissolution medium.

The dissolution times were calculated to be 3.0 min for $c = 55\% \; S_{API}$ ($R^2_{adjusted} = 0.982$, ExpDec1), 4.5 min for $c = 77\% \; S_{API}$ ($R^2_{adjusted} = 0.986$, ExpDec1) and 4.9 min for $c = 88\% \; S_{API}$ ($R^2_{adjusted} = 0.982$, ExpDec1). As can be seen from Table 3.4 the dissolution times for NS 140nm in SGF + Tween were in the same range for similar concentrations used ($2.2 - 5.1$ min). More data will be necessary to enable a general conculsion regarding differences and similiarities of fenofibrate nanocrystal dissolution in both dissolution media.
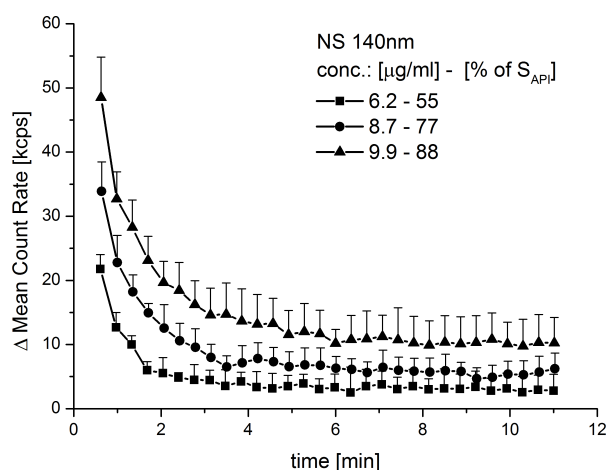
Figure 3.23: Fenofibrate NS 140nm dissolution in FaSSIF measured by light scattering. Measurement parameters: 2 runs at 10 s, measurement position 4.65 mm, attenuator 7, 25°C ($n = 4$).

3.6.10   Summary and conclusions

Manifold shortcomings are associated to conventional and published alternative dissolution methods to assess nanocrystal dissolution. This triggered the development of an alternative nanocrystal dissolution method. The approach to probe the presence of nanoparticles by monitoring light scattering intensities was followed and its applicability was demonstrated.

The new method can be described as a straightforward dilution and in situ-measurement technique. All sampling, separation and chromatographic quantification steps are avoided. The elimination of the separation step is especially favorable for nanocrystal dissolution due to its inefficiency, slowness and invasive character. A continuous and fast data acquisition offers a much higher information density as can be achieved with the conventional method. An additional feature of the presented method is its small scale setup. By operating with a nanosuspension volume of a few μl, dissolution experiments could easily be integrated in early formulation development studies with typically limited availability of API. In a direct comparison a light scattering dissolution curve matched a conventionally generated dissolution curve remarkably well, which demonstrates the eligibility of the alternative technique. The new approach was applicable to differentiate between different particle sizes and concentration gradients with a satisfying sensitivity and reproducibility. The nanocrystal size most suitable for the light scattering method is in the lower nanometer range (mean particle size < 500 nm).

So far only nanosuspensions, which are used in preformulation studies, were investigated. However, in market products the nanosuspensions are usually further processed and more excipients are added to the formulation. A transfer of the scattering dissolution method to later development phases would require an implementation of strategies to cope with undissolvable excipients due to their influence on light scattering measurements. For example prefiltration steps could be included, which we successfully applied to measure nanocrystal dissolution of the market product EMEND®. Finally it should be noted that the measurement of particle dissolution by light scattering techniques will only allow straightforward data interpretation, if no absorption of light occurs at the selected wavelength.

Experimentally determined dissolution times of nanosuspensions showed a linear correlation to concentration gradient and initial particle surface area as predicted by the Noyes-Whitney dissolution model. Despite being designed for constant particle surface area and sink conditions the Noyes-Whitney dissolution model was applicable for a wide concentration range in this study. Evaluation of results on the basis of advanced dissolution models, which consider further parameters relevant for particle dissolution, will help to gain further mechanistic insight from experimental data.

3.7 In vitro permeability

Many studies demonstrated that particle size reduction can be a successful strategy to increase the bioavailabiliy of poorly water soluble drugs. The main mechanisms are an enhancement in dissolution rate and solubility for small particles (Van Eerdenbrugh et al. 2010). After oral administration both lead to a steeper concentration gradient across the gastrointestinal epithelial barrier and if BCS class II drugs are considered, full advantage of their high drug permeability can be taken. A higher drug flux across the epithelial barrier is enabled. This permeation enhancing effect of particle size reduction was experimentally observed by Langguth et al. (2005); Buch et al. (2009); Wang et al. (2010); Rao et al. (2011) and others.

The aim of the presented permeability studies was to evaluate the effect of nanocrystal formulations with various particle sizes on the permeability of fenofibrate and compound AS. Nano to micron sized particles were used to cover a wide particle size range and the concentration of the stabilizers DOSS and HPMC was equal in all formulations.

The transport studies were conducted across confluent monolayers of Caco-2 cells in apical (pH 6.5) to basolateral (pH 7.4) direction. Transport-FaSSIF (tFaSSIF) was used as an alternative apical transport medium. tFaSSIF was prepared by supplementing HBSS^{++} with lecithin and sodium taurocholate to obtain a more physiologically relevant medium. The presented results subdivide into three parts: (I) an assay validation, (II) a comparison of permeability assays and (III) a permeability study with different sized crystalline micro- and nanosuspensions.

3.7.1 Validation

For permeabilities determined by Caco-2 transport studies a high variability is reported in literature. The heterogeneity of cell lines as well as varying culture conditions, passage numbers, seeding densities, filter supports and monolayer ages contribute to different transport and metabolic properties of the cells. During the transport experiment absorption properties can be influenced by the transport buffers (cosolvents/additives), substrate concentrations and the sampling protocol. Also differences in the calculation of P_{app} are reported (Volpe 2008).

In this study the permeabilities of reference substrates have been determined and are compared to literature. The aim was to improve the comparability of the presented data to published data. Lucifer Yellow is absorbed exclusively through a paracellular route and served as a marker of monolayer and tight junction integrity (Takahashi et al. 2002; Konishi et al. 2002). Griseofulvin (GF) and ketoconazole (KC) were used due to their BCS II classification and their low solubility, which provide a good comparability to fenofibrate. As apical medium HBSS^{++} was used.

Table 3.7 summarizes measured and previously published permeabilities of the reference substrates. P_{app} values determined for Lucifer Yellow (applied as solution) fit well into the range given in literature. The values for GF and KC (applied as coarse suspensions of pure crystalline API) seem to be lower than published values. However, a careful look into reported methods reveals that lower concentrations of APIs or the cosolvent DMSO were used in apical media. Whereas in the presented protocol API suspensions in cosolvent free medium at concentrations approximately $20 - 60$ fold above saturation concentration

Table 3.7: Validation of Caco-2 permeability assays by determination of apparent permeability coefficients (P_{app}) of reference substrates. For griseofulvin and ketoconazole an alternative calculation of P_{app} was applied by inserting the solubility in water C_S instead of the total initial donor concentration C_0.

	Horizontal assay	Vertical assay	Reference values
Substance		P_{app} [$* 10^{-6} cm/s$]	
Lucifer Yellow	0.27 ± 0.14	0.21 ± 0.03	0.22 [1]; 0.65 [2]
Griseofulvin	1.62 ± 0.20	2.53 ± 0.18	58 [2]; 37 [3]
Griseofulvin alternative P_{app}*	34 ± 4	51 ± 4	
Ketoconazole	0.51 ± 0.03	1.04 ± 0.40	66 [2]; 10 [4]; 15 [5]
Ketoconazole alternative P_{app}*	29 ± 2	59 ± 23	

* $C_S(GF) = 8.6 \mu g/ml$, $C_S(KC) = 4.7 \mu g/ml$ taken from DrugBank database (www.drugbank.ca)
[1] Takahashi et al. (2002)   [2] Takano et al. (2006)   [3] Yazdanian et al. (1998)   [4] Marino et al. (2005)
[5] Ingels et al. (2004)

were applied. In the literature protocols a higher amount or percentage of API is expected to be in solution and consequently to be available for absorption. The use of the total initial concentration C_0 in the calculation of P_{app} can lead to an underestimation of permeability, since only the dissolved fraction of API is absorbable. Therefore we used the solubility C_S of APIs instead of the total initial concentration C_0 in the calculation of P_{app}. C_S reflects a more realistic estimation of the API concentration available for permeation. P_{app} values calculated by this method are in good accordance with literature.

3.7.2 Comparison of permeability assays

The vertical permeability assay

A vertical permeability setup with Caco-2 monolayers grown on permeable Snapwell^{TM} filter supports mounted between side-by-side diffusion chambers was used (section 1.2.2).

The influence of gas flow on pH and TEER was evaluated in a placebo experiment with HBSS^{++} as apical transport medium (Fig. 3.24). All steps except the addition of a substrate to the apical chamber at time zero were performed according to the standard protocol. A moderate drop of pH was observed with gas flow, which was more pronounced for the basolateral medium. Carbonic acid formation out of CO_2 in the carbogen gas (5% CO_2/95% O_2) might be responsible. However, the TEER drop over time is a more relevant issue for transport studies, since it indicates a loss of integrity of cell monolayers. It was observed with and without gas flow. Most probably the reason for the TEER drop is the stressful transfer of the filter support with the monolayer from the cell culture plate into the diffusion chamber. It includes Snapwell^{TM} filter removal from the cell culture plate supports, assembly of chambers and filling of the chambers with medium. The monolayers are subjected to mechanical stress and are without medium for a few minutes. Sometimes medium leakage appears in the case of inappropriate O-ring seal attachment and the necessity of repeated chamber assembly was observed to adversely influence TEER values.

Additional drawbacks of the vertical permeability system are a lack of quantitative and reproducible gas flow adjustment, difficult control of temperature and a large inner device surface area. It was estimated
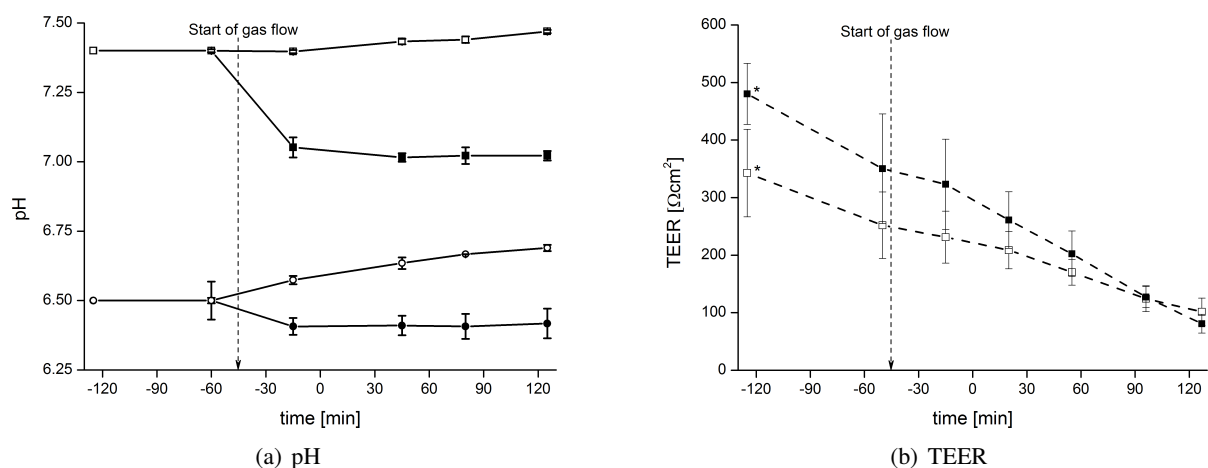
(a) pH

(b) TEER

Figure 3.24: Vertical permeability assay: Monitoring of pH (a) and TEER (b) during a placebo experiment in side-by-side diffusion chambers with gas flow (closed symbols) and without gas flow (open symbols). The chambers were assembled at the time -120 min. (a) Apical pH (circles), basolateral pH (squares). (b) Marked TEER values (*) were determined in Snapwell^{TM} cell culture plates prior to chamber assembly ($n = 3$).

to be $22\,cm^2$ for one chamber (acrylic glass) compared to an estimated inner surface area of $3\,cm^2$ (polystyrene) of the apical chamber in the horizontal permeability setup. Adsorption of large amounts of poorly water soluble API onto the device surface might be the consequence.

Comparison of horizontal and vertical permeability assay

A direct comparison of both permeability assays was performed and fenofibrate was applied as

- **FF:** pure crystalline FF suspended in apical transport medium
  homogenized by magnetic stirring (SLS D50 $11 - 18\,\mu m$)

- **rawNS:** coarse crystalline FF suspended in an DOSS/HPMC solution
  homogenized by magnetic stirring (SLS D50 $11 - 13\,\mu m$)

- **NS:** FF nanosuspension NS 160nm
  obtained by wetmilling of rawNS (SLS D50 138 nm)

Figure 3.25(a) displays the permeated amounts of API over time and Table 3.8 summarizes the apparent permeability coefficients. Rapid metabolization of fenofibrate by Caco-2 esterases occurred and only fenofibric acid was detectable in the receiver compartment. After 120 min FFA was also detected in the donor compartment.

Figure 3.25(a) shows that in general lower amounts of API in the receiver compartment were detected in the vertical setup. A higher permeability of NS and raw NS compared to FF drug substance was seen for both assays. A significantly higher permeability was measured for rawNS than for NS in the horizontal assay. An explanation might be that the bigger particles sediment in the horizontal assay, which increases

Table 3.8: Permeabilities of fenofibrate drug substance and fenofibrate formulations determined by horizontal and vertical permeability assay.

Formulation	Horizontal assay	Vertical assay
	P_{app} [$* 10^{-6}$ cm/s]	
pure crystalline substance	0.64 ± 0.07	0.35 ± 0.08
coarse suspension (rawNS)	3.74 ± 0.26	2.00 ± 0.14
nanosuspension NS 160nm	2.61 ± 0.22	2.34 ± 0.33

the concentration gradient at the monolayer and consequently enhances permeability. A higher P_{app} was measured for NS than for rawNS in the vertical setup which was, however, not significant. No significant difference in the permeability of the nanosuspension was observed in the vertical vs horizontal assay (p < 0.05 for all tests).

The comparison of API recovery (Fig. 3.25(b)) reveals a much better mass balance for formulated fenofibrate (rawNS and NS). The stabilizers DOSS and HPMC prevent adsorption to plastic surfaces and improve particle wettability. A tendency for a lower recovery of API from the vertical system could be observed due to a higher device surface area. Adsorptive loss might contribute to lower permeated API amounts measured in the vertical assay.

The development of pH and TEER in the vertical assay (Fig. 3.25(d)) are the same as seen in the placebo experiment (Fig. 3.24). On the contrary stable TEER values were measured in the horizontal assay (Fig. 3.25(c)). The simultaneous monitoring of cell capacitance C_{Cl} provides insight into changes of the cell membrane surface area. A stable cell capacitance demonstrates that cells were not adversely affected during the experiment.

Comparison of permeability assays: Summary and conclusions

The aim of the permeability studies was to determine the permeability of APIs formulated as particle suspensions. Since gentle horizontal shaking in the horizontal assay cannot completely compensate for sedimentation of larger particles, a vertical permeability setup was evaluated. Not only the positioning of the cell monolayer, but also hydrodynamic conditions which create a minimized unstirred water layer (UWL) might be advantageous for permeability assessment of suspensions of poorly water soluble compounds.

Indeed the finding of a higher permeability from a micron versus a nano sized suspension in the horizontal setup might indicate that sedimentation influences permeability. On the other hand the expected permeability enhancing effect of particle size reduction could also not be seen in the vertical setup. Regarding the criterion of providing a good distinguishability between formulations none of the systems did offer clear advantages. As expected the API recovery from the side-by-side diffusion chambers was lower, even though the differences were small.

The main drawback of the vertical system is a decrease of TEER over time indicating a loss of cell monolayer integrity, which is a prerequisite for successful transport studies. Other shortcomings are leakage

(a) Permeation

(b) API recovery
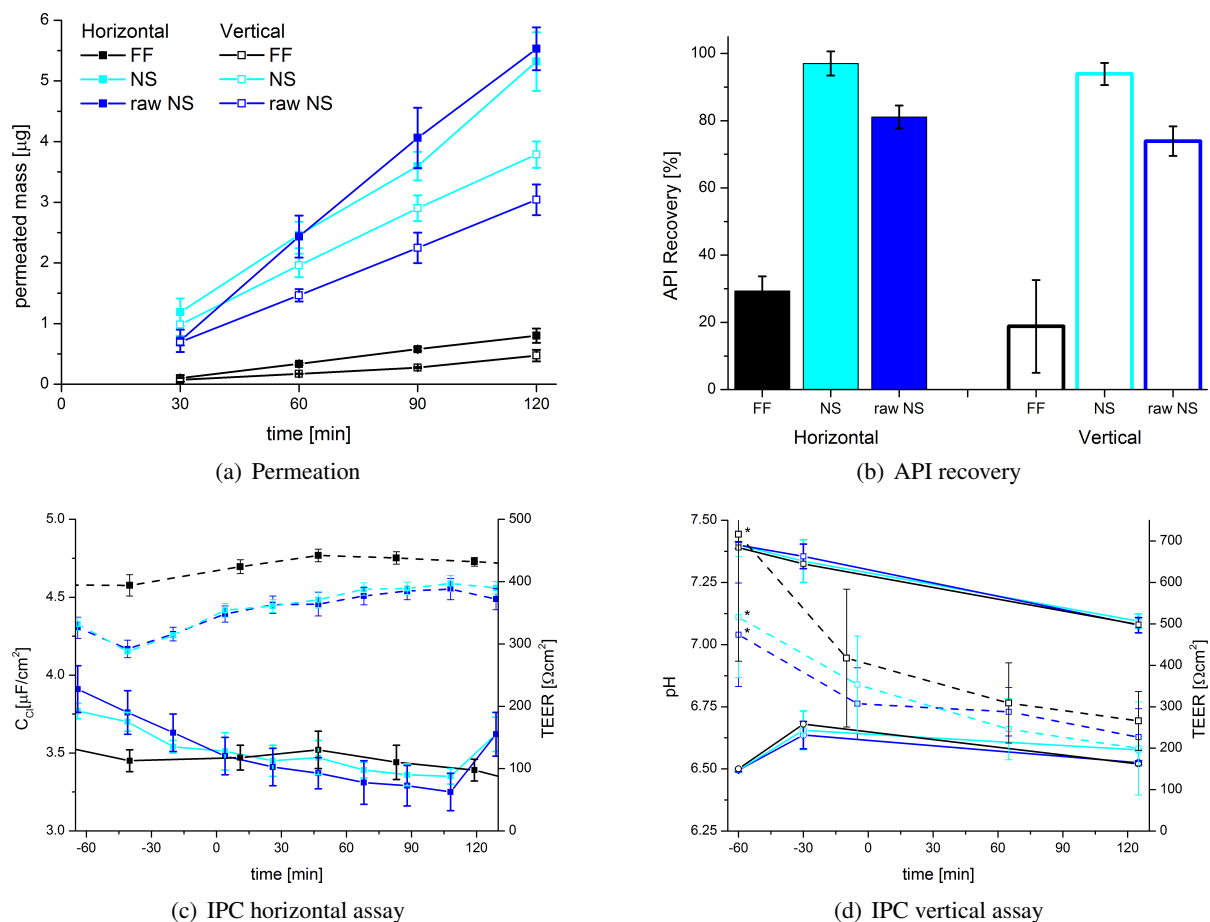
(c) IPC horizontal assay

(d) IPC vertical assay

Figure 3.25: Comparison of horizontal (closed symbols) and vertical (open symbols) permeability assay for pure FF crystalline suspension (black), FF nanosuspension NS 160nm (light blue) coarse FF crystalline suspension (blue). (a) Permeated amount of FFA versus sampling time. (b) API recovery. (c) In-process control (IPC) of capacitance C_{Cl} (compact lines) and TEER (dashed lines) for the horizontal assay. (d) IPC of apical pH (circles), basolateral pH (squares) and TEER (dashed lines) for the vertical assay. Marked TEER values (*) were determined in Snapwell^{TM} cell culture plates prior to chamber assembly ($n = 4 - 5$).

and difficulties in adjustment of a standardized gas flow and temperature. The CellZscope® device used for horizontal permeability studies offers clear experimental advantages, like an automated monitoring of TEER and capacitance in parallel. Additionally simultaneous experiments in 24 wells can be performed under easily adjustable temperature and shaking conditions. This optimizes throughput and repeatability. The horizontal system was selected for further studies due to the experimental drawbacks of the vertical setup. The vertical setup did not improve the permeation ranking of formulations.

3.7.3   Permeability of APIs formulated as crystalline micro- and nanosuspensions

Stability of nanosuspensions in transport media

The stability of selected nanosuspensions of FF and AS in apical transport media was evaluated with respect to particle size. The aim was to identify stable formulations suitable to study the effect of particle size on permeation. Selection of formulations was governed by the intention to cover a wide particle size range.
Figure 3.26(a,b) shows that the fenofibrate suspension NS 140nm was not stable in $HBSS^{++}$, but was in tFaSSIF. Salts are responsible for rapid particle agglomeration. Since the salt concentration in both media is equal, the better stability in tFaSSIF can be attributed to the phospholipid lecithin and the bile salt sodium taurocholate. As amphiphilic molecules they exhibit a particle stabilizing effect through adsorption to the particle surface area. No instabilities were observed for fenofibrate formulations NS 270nm and NS 1070nm.
The compound AS nanosuspension NS 100nm agglomerated immediately after dilution, whereas NS 150nm and NS 860nm were found to be stable in both media and were selected for further studies (Fig. 3.26(c,d)).

Permeability of APIs formulated as crystalline micro- and nanosuspensions

The fenofibrate permeability from formulations NS 140nm, NS270nm, NS1070nm and MS 7.9μm and the compound AS permeability from NS 150nm, NS 860nm and MS 6.8μm were determined by the horizontal permeability assay. The apical medium was varied and all experiments were performed with Caco-2 cells grown on permeable filter supports and with empty filters. In-process controls of TEER and capacitance were performed and the recovery of API at the end of each experiment was determined. All results can be found in Figure 3.27 and 3.28. The calculated P_{app} values are listed in Table 3.9. Table 3.10 summarizes all experiments and the effects of experimental conditions on the measured permeability and recovery.
Prior to experiments with formulations the effect of pure transport media on Caco-2 cells was studied in a placebo experiment. TEER and capacitance were stable for 180 min within ± 10% of the start value (data not shown). Stable TEER and capacitance was also given in experiments with formulations (Fig. 3.27(c,d) and 3.28(c,d)).
In assays performed with fenofibrate and with Caco-2 cells fenofibric acid was the only detectable substrate in the receiver compartment.
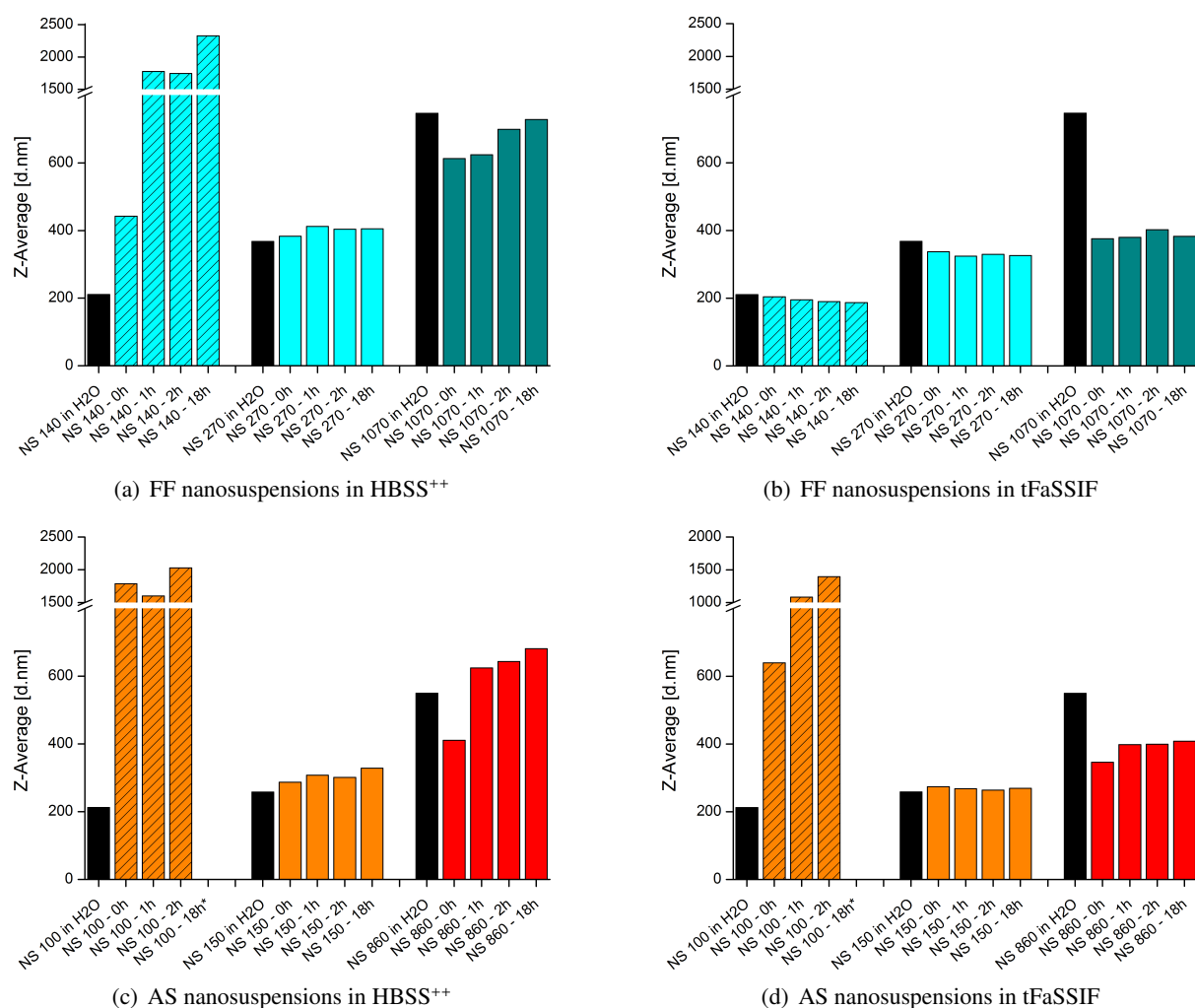
(a) FF nanosuspensions in HBSS^{++}

(b) FF nanosuspensions in tFaSSIF

(c) AS nanosuspensions in HBSS^{++}

(d) AS nanosuspensions in tFaSSIF

Figure 3.26: Stability of fenofibrate and compound AS suspensions in HBSS^{++} and tFaSSIF at a concentration of 0.5 mM. The particle size was measured by dynamic light scattering and is reported as Z average diameter. At 0, 1, 2 and 18 h after dilution the particle size was measured. As reference values the particle sizes measured in water are displayed (black columns) ($n = 1$).
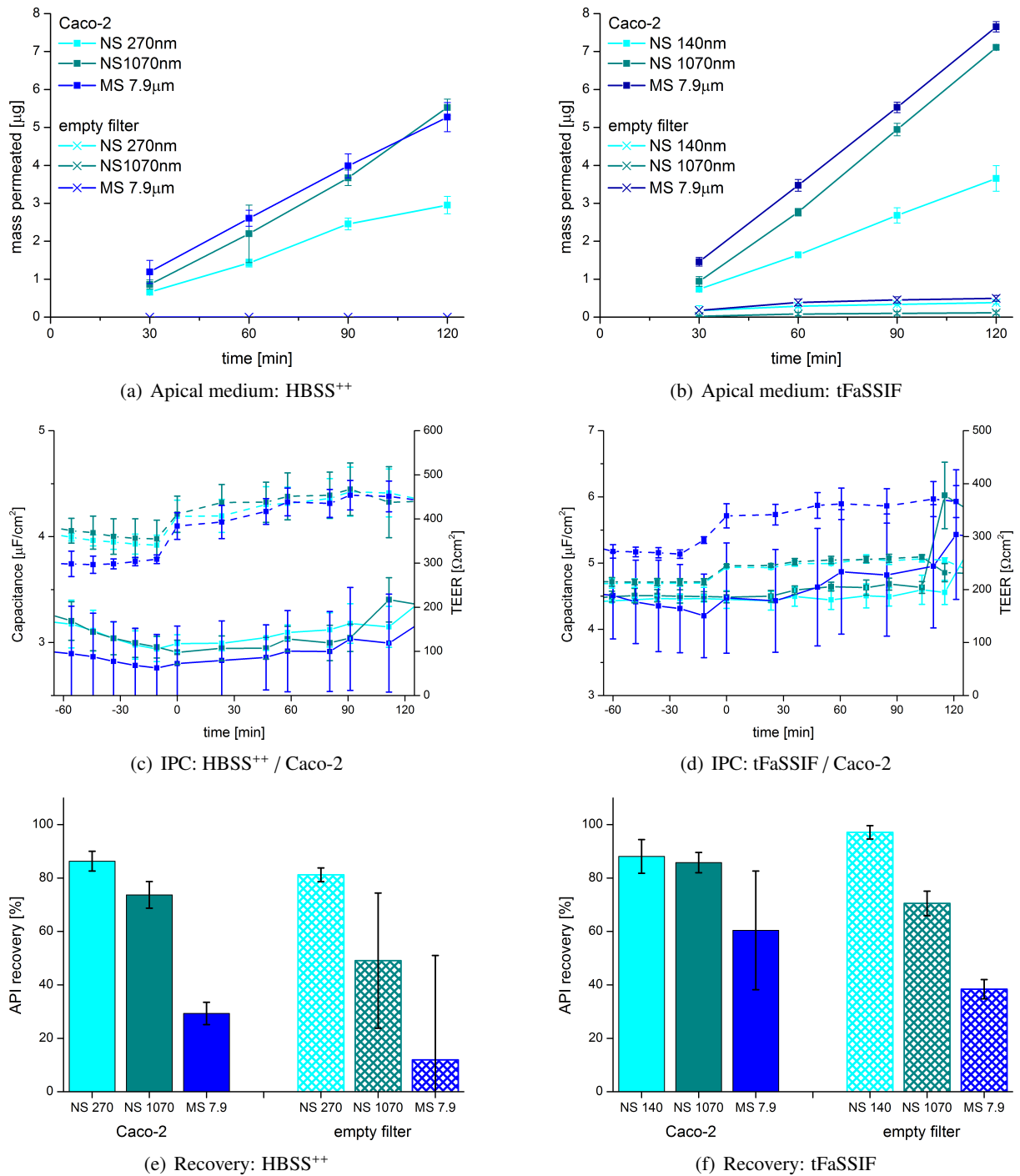
Figure 3.27: Permeability of fenofibrate suspensions determined by horizontal permeability assay. The apical medium was varied: HBSS[++] (a,c,e) and tFaSSIF (b,d,f) were used. Caco-2 monolayers grown on filters (squares) and empty filters (crosses) were evaluated as permeation barrier. Panels (c) and (d) show in-process controls (IPC) of capacitance (compact lines) and TEER (dashed lines). The permeation experiment was started at time zero and earlier data points represent the equilibration phase. Panels (e) and (f) show the total API recovery ($n = 3$).
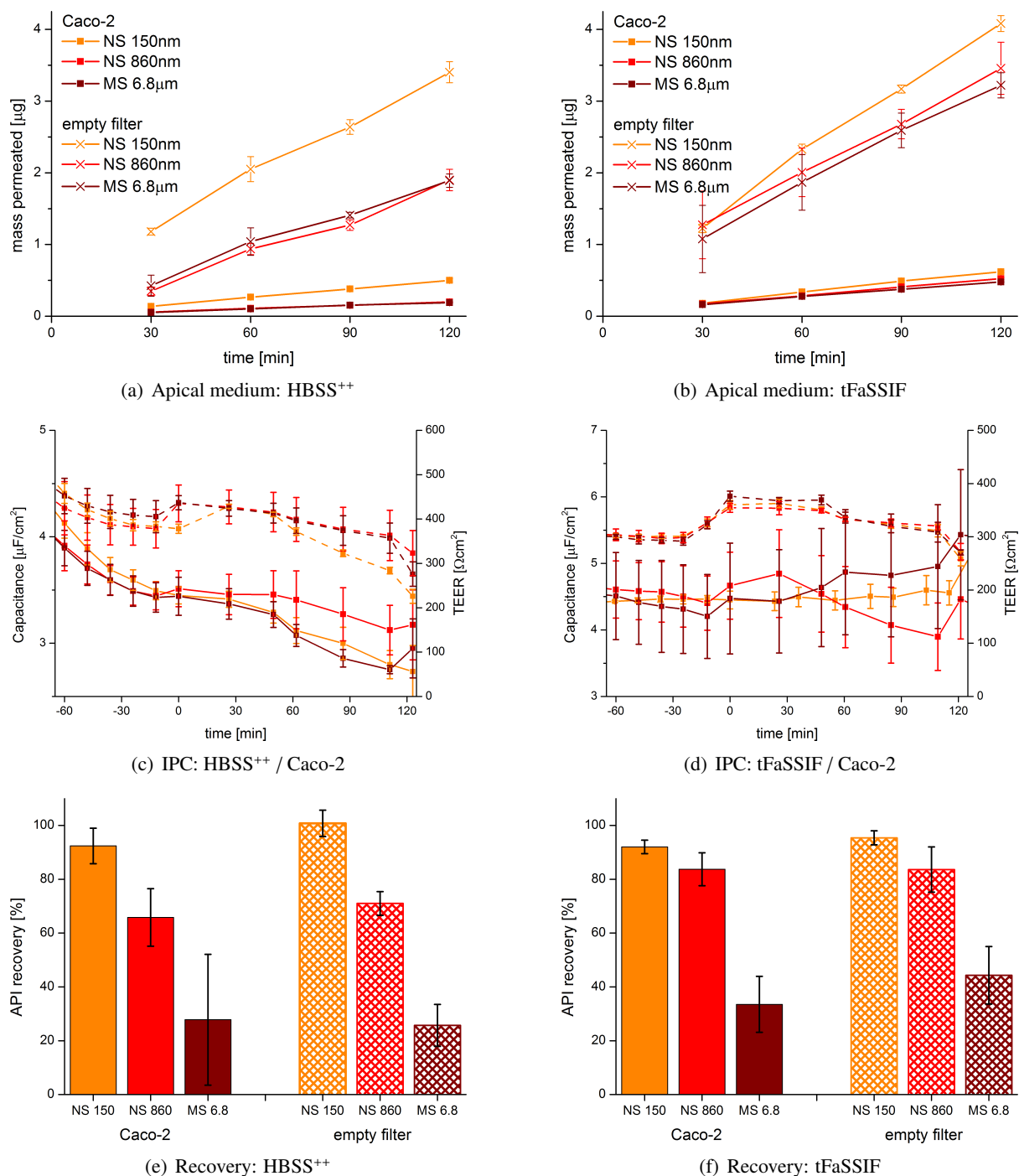
(a) Apical medium: HBSS^{++}

(b) Apical medium: tFaSSIF

(c) IPC: HBSS^{++} / Caco-2

(d) IPC: tFaSSIF / Caco-2

(e) Recovery: HBSS^{++}

(f) Recovery: tFaSSIF

Figure 3.28: Permeability of compound AS suspensions determined by horizontal permeability assay. The apical medium was varied: HBSS^{++} (a,c,e) and tFaSSIF (b,d,f) were used. Caco-2 monolayers grown on filters (squares) and empty filters (crosses) were evaluated as permeation barrier. Panels (c) and (d) show in-process controls (IPC) of capacitance (compact lines) and TEER (dashed lines). The permeation experiment was started at time zero and earlier data points represent the equilibration phase. Panels (e) and (f) show the total API recovery ($n = 3$).

Table 3.9: Apparent permeability coefficients (P_{app}) of fenofibrate and compound AS suspensions determined by in the horizontal permeability assay. The apical medium was varied: HBSS^{++} and tFaSSIF were used. In addition to Caco-2 monolayers grown on Transwell® filter inserts (Caco-2), the barrier properties of empty Transwell® filters (empty filter) were evaluated.

	HBSS^{++}		tFaSSIF	
	Caco-2	**empty filter**	**Caco-2**	**empty filter**
Formulation	P_{app} [$* 10^{-6}$ cm/s]			
Fenofibrate formulations				
NS 140nm			2.66 ± 0.33	0.14 ± 0.10
NS 270nm	2.21 ± 0.19	0.00 ± 0.00		
NS 1070nm	4.20 ± 0.06	0.00 ± 0.00	5.61 ± 0.08	0.08 ± 0.04
MS 7.9μm	3.69 ± 0.52	0.00 ± 0.00	5.60 ± 0.18	0.28 ± 0.06
Compound AS formulations				
NS 150nm	0.25 ± 0.01	1.52 ± 0.09	0.31 ± 0.03	1.98 ± 0.09
NS 860nm	0.10 ± 0.00	1.05 ± 0.08	0.25 ± 0.01	1.52 ± 0.14
MS 6.8μm	0.10 ± 0.00	1.00 ± 0.12	0.22 ± 0.00	1.50 ± 0.30

Effect of particle size. In the present study a positive effect of size reduction on permeability was seen for AS suspensions. For FF the smallest suspensions NS 140nm and NS 270nm had the significantly lowest permeabilities ($p < 0.05$), despite the fact that a solubility enhancing effect was demonstrated for NS 140nm (section 3.4.2). No permeability enhancing effect was observed for particles with a size of approx. $1\,\mu$m (FF NS 1070nm, AS NS 860nm) with reference to particles with approx. $7 - 8\,\mu$m (FF MS 7.9μm, AS MS 6.8μm) ($p < 0.05$). Expected equal solubilities for formulations in both size ranges can explain this result.

A specific feature of permeability studies on the ester prodrug fenofibrate is that fenofibrate is hydrolyzed during the assay by Caco-2 esterases. After 120 min the fenofibric acid concentrations in the apical compartment were approximately $11 - 22\,\mu$g/ml (Fig. 3.29). This corresponds to a metabolized fraction of $6 - 12\,\%$ (relating to the total apically applied API (FF)) or $5 - 30\,\%$ (relating to the total apically recovered API (FF+FFA)). A rapid hydrolysis and a more than 100-fold higher water solubility of fenofibric acid suggests a negligible fraction of dissolved fenofibrate present in the donor compartment. It is probable that higher concentrations of dissolved fenofibric acid prevail and that fenofibric acid is consequently the substrate mainly permeating across the Caco-2 monolayer. In that case the hydrolysis rate would control the diffusion rate. This hypothesis is supported by a good correlation between P_{app} values and the fenofibric acid concentrations in apical compartment after 120 min (Fig. 3.29). It seems that not the particle size or solubility did control permeabilities, but the rate of fenofibrate hydrolysis.

This hypothesis is supported by two published studies. Linn et al. (2012) studied the Caco-2 permeability of fenofibrate drug substance and a fenofibrate solid dispersion. The assumption that transport is controlled by hydrolysis is discussed in order to explain some of the experimental findings. Zhu et al. (2010) studied the site-specific absorption of fenofibrate versus fenofibric acid in humans by delivering FF and
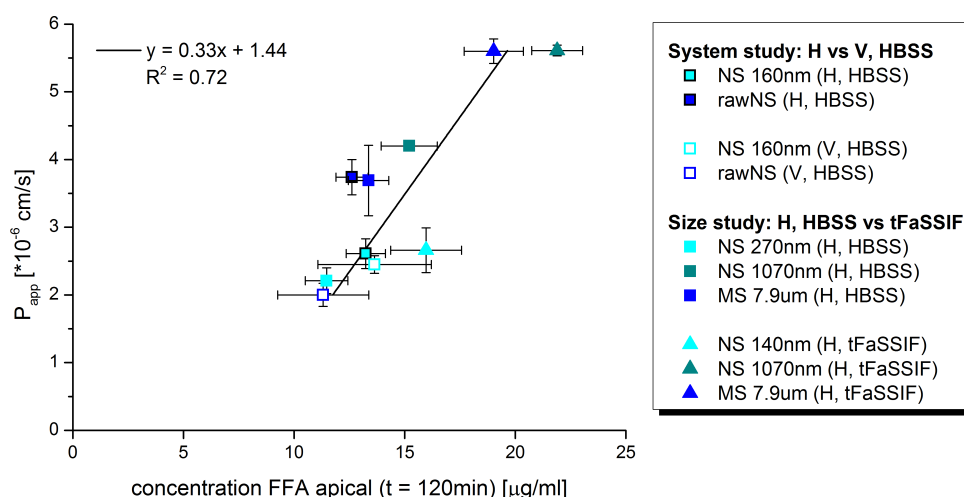
Figure 3.29: Correlation of apparent FF permeability P_{app} and fenofibric acid concentration in apical compartment. Included are experiments with different fenofibrate formulation, transport assay (H: horizontal, V: vertical) and transport medium.

FFA nanocrystal dispersions specifically to the stomach, proximal small bowel, distal small bowel and the colon. Higher C_{max}, lower T_{max} and higher bioavailability of FFA at all regions of the GI tract and especially at the colon suggest that FFA has improved absorption characteristics over FF.

Effect of Caco-2 monolayer compared to empty filter. No permeation of fenofibrate across empty filters was observed in the case of HBSS^{++} used as apical medium. This result is in contrast to expected higher permeabilities when the cell monolayer as permeation barrier is missing (Hidalgo et al. 1991; Yu and Sinko 1997). It seems that fenofibrate itself does not diffuse across the filter support. In the case of tFaSSIF as apical medium little amounts of fenofibrate pass the filter. Mixed micelles might function as carriers which transport fenofibrate through the pores.

In empty filter experiments better recoveries with tFaSSIF than with HBSS were observed, which indicates a lower absorptive loss caused by solublizing agents. With HBSS better recoveries were observed with Caco-2 cells than with empty filters, which indicates a higher absorptive loss when the plastic surface area is increased due to the missing cell monolayer. It can be concluded that FF adsorption to the apical filter surface or pores is most likely responsible for low permeabilities with empty filters. As well blocking of filter pores by particles might occur.

For AS particle suspensions the barrier properties of the cell monolayer become visible. With empty filters higher amounts of API are detected basolaterally. While the suspensions with medium and large particles are not distinguishable, clearly more API passes the filter when the smallest sized suspension is employed. Diffusion of the nanocrystals in NS 150nm through the $0.4\,\mu m$-pores and an improved solubility explain higher permeabilities.

Effect of apical transport medium. Higher P_{app} values can be measured for FF formulations in tFaS-SIF than in HBSS^{++}. While the effect is not significant for the smallest sized suspensions, tFaSSIF enhances the permeability significantly for the medium and large sized suspensions ($p < 0.05$). A higher

Table 3.10: Overview of effects of experimental conditions on permeability and recovery.

Given parameter	Measured parameter	FF/FFA	AS
particle size[*]	permeability	large = medium > small	small > medium = large
	recovery	small > medium > large	small > medium > large
Caco-2 vs empty filter	permeability	Caco-2 > empty	empty > Caco-2
	recovery	Caco-2 = empty	empty $\geq$ Caco-2
HBSS vs tFaSSIF	permeability	tFaSSIF > HBSS	tFaSSIF > HBSS
	recovery	tFaSSIF $\geq$ HBSS	tFaSSIF $\geq$ HBSS

[*] Small particle size refers to formulations FF NS 140nm and AS NS 150nm, medium particle size to FF NS 1070nm and AS NS 860nm and large particle size to FF MS 7.9μm and AS MS 6.8μm.

solubility in tFaSSIF might explain this finding. Additionally with tFaSSIF higher concentrations of fenofibric acid were found in the apical compartment. A good overall correlation of P_{app} and fenofibric acid concentration (Fig. 3.29) for both media might suggest that not the solubility enhancing effect, but a hydrolysis enhancing effect of tFaSSIF gives the main contribution.

The interpretation of AS permeation data is not complicated by simultaneous API metabolization. Here higher P_{app} values in tFaSSIF than in HBSS^{++} can be attributed to a higher solubility of AS in tFaSSIF. In literature diverse effects of solubilization by micellar encapsulation on permeability are discussed (Kleberg et al. 2010). A parallel increase of permeability with micellar solubility, like demonstrated in this study, is reported in literature. Brouwers et al. (2006) observed a 60 % increase in permeabiliy of amprenavir (poorly water soluble, logP 2.43) when using FaSSIF or human intestinal fluids compared to HBSS. On the contrary also a decreasing effect on permeability has been observed manifold and was explained by an entrapment of drug molecules in micelles and a reduction of free drug concentration (Ingels et al. 2004; Fossati et al. 2008; Yano et al. 2010).

A trend to better recoveries in tFaSSIF especially for the formulations with larger particles was observed for both APIs and is in good accordance with literature (Ingels et al. 2004; Fossati et al. 2008).

3.7.4 Permeability of fenofibrate formulations in literature

To the best knowledge of the authors only two studies investigating formulation effects on the permeability of fenofibrate in Caco-2 transport assays are published (Buch et al. 2009; Linn et al. 2012). Table 3.11 provides an overview of the here presented and previously published results and methods.

In both literature studies the permeability of pure crystalline fenofibrate was determined. Also the comparability is hampered by the usage of different experimental methods very similar fenofibrate permeabilities were determined. Positive effects on the permeability of fenofibrate formulated as solid dispersions could be demonstrated by both authors. Furthermore Buch et al. (2009) used a powderized TriCor® 145mg tablet as a nanoparticulate formulation and reports an approximately 10-fold permeability increase. However, this is not the ideal formulation to study the sole effect of particle size reduction. The reason is that the TriCor® tablet contains the ionic surfactant sodium lauryl sulfate (SLS) at unknown concentration. SLS can improve the solubility of fenofibrate strongly (Granero et al. 2005).

Table 3.11: Permeabilities of fenofibrate drug substance and fenofibrate formulations determined by horizontal and vertical permeability assay and comparison with reference values from literature.

Formulation	Horizontal assay	Vertical assay
	P_{app} [$* 10^{-6}\, cm/s$]	
Comparative study of permeability assays and particle sizes [1]		
pure crystalline substance	0.64 ± 0.07	0.35 ± 0.08
nanosuspension NS 160nm	2.61 ± 0.22	2.34 ± 0.33
nanosuspension NS 270nm	2.21 ± 0.19	
nano/microsuspension NS 1070nm	4.20 ± 0.06	
microsuspension MS 7.9μm	3.69 ± 0.52	
coarse suspension with HPMC and DOSS	3.74 ± 0.26	2.00 ± 0.14
Permeability of FF and FF formulations reported by Linn et al. (2012) [2]		
pure crystalline substance	0.86	
physical mixture: 20% FF in Soluplus®	1.35	
solid dispersion: 20% FF in Soluplus®	2.48	
Permeability of FF and FF formulations reported by Buch et al. (2009) [3]		
pure crystalline substance 28μm / 5μm *		0.13 / 0.19
powderized nanoparticulate tablet formulation **		1.11
powderized solid dispersion tablet formulation		1.91

Linn et al. (2012) and Buch et al. (2009) did not calculate P_{app} values. On the basis of the provided information P_{app} values were derived.

Experimental setup: membrane material and pore size, initial concentration in donor compartment, apical (A) and basolateral (B) transport medium.

[1] polyester 0.4μm, c_0 = 0.181 mg/ml, A: HBSS pH 6.5, B: HBSS pH 7.4.

[2] polyester 0.4μm, c_0 = 1.0 mg/ml, A: KRB pH 7.4, B: KRB pH 7.4 + 0.2% vitamin E TPGS 1000.

[3] polycarbonate 0.3μm, c_0 = 0.181 mg/ml, A: HBSS + 3mM NaTC + 0.75mM lecithin, pH 6.5 B: HBSS + 4.5% BSA pH 7.4. * average particle size. ** TriCor®, Abbott Laboratories, Abbott Park, IL, USA.

3.7.5   Summary and conclusions

The aim of the permeability studies was to evaluate the effect of particle size on the permeability of two APIs. Nano to micron sized particles were used to cover a wide particle size range and the concentrations of stabilizers DOSS and HPMC were equal for all formulations. A horizontal permeability assay was used with different apical media, one of which was a biorelevant transport medium. The permeabilities of pure crystalline fenofibrate, ketoconazole and griseofulvin drug substances determined in this study were in good accordance with literature.

The results for AS formulations meet the expectations and are in accordance to findings in literature: A smaller particle size improves the permeability, the Caco-2 monolayer and not the empty filter is the main permeation barrier and the micellar medium tFaSSIF improves the API recovery from the assay.

On the contrary, for fenofibrate unexpected findings were identified: A smaller particle size negatively affected permeation and lower permeabilities were seen with empty filters than with filters covered over by a Caco-2 monolayer. The latter indicates that adsorptive loss of API is an issue which has to be carefully considered in fenofibrate transport studies. In the discussion about the permeability results for fenofibrate formulations further aspects can be mentioned. The FF permeability can be influenced by the formulation, hydrolysis and micellar encapsulation. The interplay of all aspects makes the interpretation of results difficult. However, the data suggest that API hydrolysis of fenofibrate to fenofibric acid is a crucial parameter. Taking into account P_{app} values measured under various conditions (vertical vs horizontal assay, particle size, transport medium) an overall tendency for higher permeabilities with higher fenofibric acid concentrations was observed (Fig. 3.29).

To support this hypothesis and to gain further insight into the mechanism and influencing parameters of fenofibrate permeation more reference experiments are required. An evaluation of esterase activity under different conditions and transport experiments with an inhibition of hydrolytic enzymes will help to analyze the effect of hydrolysis systematically. Recently Ohura et al. (2010) highlighted the role of carboxylesterases in the assessment of transepithelial transport of ester prodrugs. With bis-p-nitrophenyl phosphate (BNPP) he describes a specific carboxylesterase inhibitor. Additional experiments to study the mechanism of fenofibrate/fenofibric acid permeation applied as nanocrystal formulation might cover: (I) a concentration titration of biorelevant surfactants to quantitatively estimate the effect of micellar solubilization on permeation, (II) the quantification on intracellular uptake into recovery calculations and (III) identification of transporters possibly involved in FF and FFA absorption.

3.8   In vivo pharmacokinetics

The aim of this *in vivo* pharmacokinetic study was to evaluate the effect of particle size on the bioavailability. Therefore suspensions of fenofibrate and compound AS were orally administered to rats. Solutions of both APIs were furthermore administered intravenously. The correlation between *in vitro* dissolution data and *in vivo* bioavailability was investigated. In addition it was evaluated whether *in silico* simulation can predict concentration-time profiles of nano and micron sized formulations correctly.

3.8.1   The effect of fenofibrate and compound AS particle size reduction on pharmacokinetics

The observed plasma concentration-time profiles and pharmacokinetic parameters for all formulations are summarized in Figure 3.30 and Table 3.12. After oral administration of fenofibrate only the metabolite fenofibric acid was detected in all plasma samples.

For fenofibrate crystal size reduction a trend towards shorter T_{max}, higher C_{max} and higher AUC values was observed. All pharmacokinetic parameters indicate that particle size reduction can improve the rate and extent of FF absorption from the GI tract. A 1.5-fold increase in bioavailability was achieved by particle size reduction from 7.9 μm to 140 nm and the absolute bioavailability was raised from 57 % to 83 % (Fig. 3.31(a)).

A similar effect of particle size reduction was observed for compound AS. Higher C_{max} and higher AUC values were achieved, while the size reduction had no effect on T_{max}. It seems that the extent, but not the rate of absorption is enhanced with decreasing particle size. An overall trend towards higher bioavailability for smaller particles can be assumed, although the formulation NS 1320nm does not fit into this tendency (Fig. 3.31(b)). A 1.8-fold increase in bioavailability was achieved by particle size reduction from 6.8 μm to 100 nm and the absolute bioavailability could be raised from 28 % to 50 %. Compared to fenofibrate lower absolute bioavailabilities were observed, which indicates a lower permeabiliy of compound AS. A lower permeability of AS was also found in *in vitro* studies on Caco-2 monolayers (Tab. 3.9). The nanosuspensions FF NS 140nm and AS NS 150nm exhibited similar particle size and showed a similar relative bioavailabiliy of 145 % and 135 %, respectively.

3.8.2   The in vivo effects of particle size reduction: Discussion

It has been described manifold that nanocrystal formulations can help to increase the oral bioavailability of poorly water soluble drugs. Here only few examples from literature are given: Wu et al. (2004); Jinno et al. (2006, 2008); Wang et al. (2010); Xia et al. (2010); Sigfridsson et al. (2011); Quinn et al. (2012). Some of their results are: The strategy of particle size reduction, surface area enhancement, dissolution rate enhancement leading to a higher systemic exposure is successful for dissolution rate-limited absorption. If the conditions for a dissolution rate-limited absorption are met, for example, depends on the applied dose and the absorption window of the drug substance. At low doses or with a broad absorption window a particle size reduction will not always lead to a higher systemic exposure (Wu et al. 2004; Sigfridsson et al. 2011).

(a) Fenofibrate / Fenofibric acid: p.o.

(b) Compound AS: p.o.

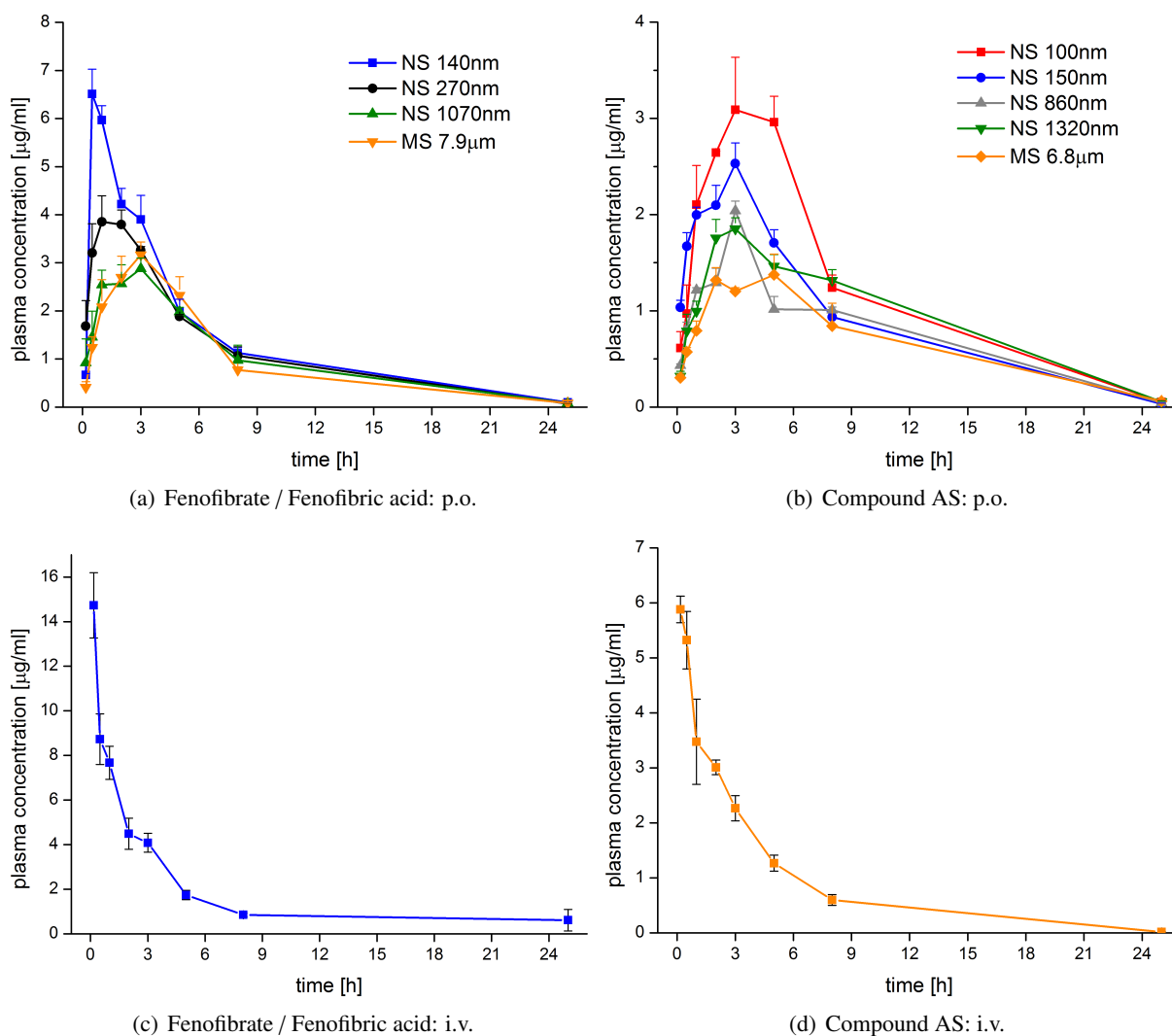(c) Fenofibrate / Fenofibric acid: i.v.

(d) Compound AS: i.v.

Figure 3.30: (a+b) Plasma concentration-time profiles of orally administered suspensions. (a) FF dose 2.1 mg/kg. (Only FFA found in plasma). (b) AS dose 2.7 mg/kg. (c+d) Plasma concentration-time profiles after i.v. administration of API solutions. (c) FFA dose 2.1 mg/kg. (d) AS dose 1.0 mg/kg. All data expressed as arithmetic mean $+/\pm$ standard error of the mean ($n = 3$).

Table 3.12: Pharmacokinetic parameters of FF and AS p.o. and i.v. administration. FFA dose i.v. 2.1 mg/kg, FF dose p.o. 2.1 mg/kg, AS dose i.v. 1.0 mg/kg, AS dose p.o. 2.7 mg/kg.

Formulation	Route	Dose	T_{max}	C_{max}	$AUC_{0 \to 25h}$	F_{abs}	F_{rel} [*]
		[mg/kg]	[h]	[ng/ml]	[ng/ml∗h]	[%]	[%]
Fenofibrate							
FFA solution	i.v.	2.1	0.2	14733	41711	100	–
NS 140nm	p.o.	2.1	0.5	6511	34532	83	145
NS 270nm	p.o.	2.1	1.0	3853	29276	70	123
NS 1070nm	p.o.	2.1	3.0	2881	25009	60	105
MS 7.9μm	p.o.	2.1	3.0	3168	23850	57	100
Compound AS							
AS solution	i.v.	1.0	0.2	5880	21972	100	–
NS 100nm	p.o.	2.7	3.0	3090	29658	50	181
NS 150nm	p.o.	2.7	3.0	2530	22240	37	135
NS 860nm	p.o.	2.7	3.0	2040	18701	32	114
NS 1320nm	p.o.	2.7	3.0	1853	22979	39	140
MS 6.8μm	p.o.	2.7	5.0	1375	16420	28	100

[*] The relative bioavailabilities F_{rel} of the nanosuspensions (NS) were calculated with reference to the *AUC* of the microsuspensions (MS).

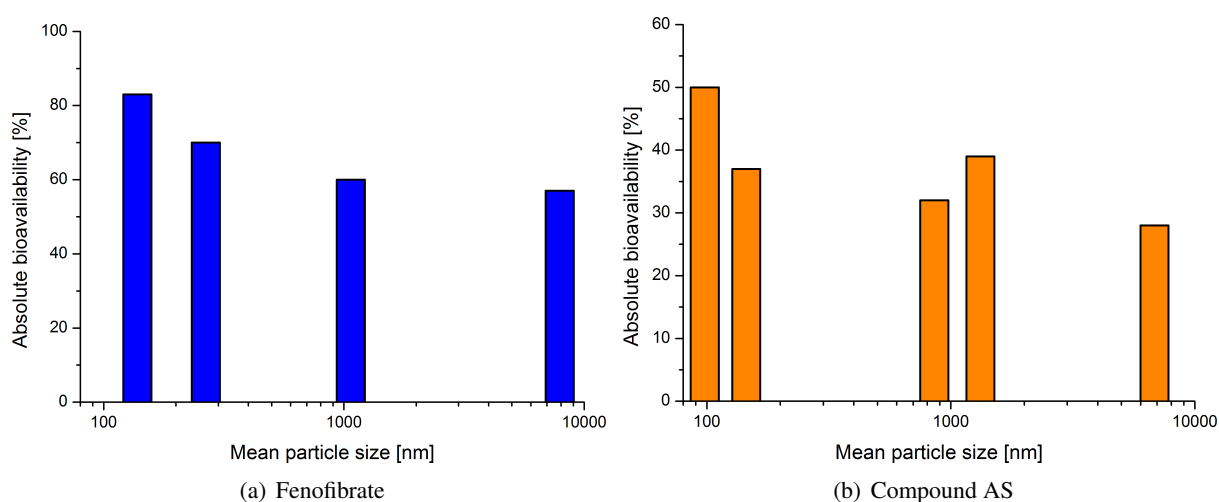(a) Fenofibrate

(b) Compound AS

Figure 3.31: FF and AS bioavailability as a function of particle size.

An improvement of the oral bioavailability of fenofibrate by particle size reduction was for example demonstrated by Li et al. (2009) (amorphous nanosuspensions), by Chen et al. (2009) (liposomes), by Jia et al. (2011) (silica/polymethylacrylate nanomatrix) and by Hanafy et al. (2007) (DissoCubes® nanosuspension and solid lipid nanoparticles). Crystalline nanosuspensions were used in the studies of Buch et al. (2009).

While in the majority of studies only one nano-formulation is evaluated against a larger sized reference formulation (microsuspension or coarse suspension), only few studies deal with a incremental particle size reduction. Examples for the latter can be found in Wu et al. (2004); Li et al. (2009); Xia et al. (2010); Wang et al. (2010) and will be shortly summarized below.

Wang et al. (2010) used silybin nanocrystal suspensions with particle sizes of 127 nm and 642 nm (DLS Z average, PDI 0.30 and 0.38) and compared it to an un-milled silybin suspension in a PK study on beagle dogs. A 2.9-fold and 2.3-fold bioavailability enhancement was observed for the nanocrystal formulations. No significant difference between both nanosuspensions was observed.

Li et al. (2009) performed a bioavailability study in rats with amorphous fenofibrate nanosuspensions (FF dose 27 mg/kg). The particle sizes were 194 nm and 356 nm (DLS Z average, PDI 0.25 and 0.19). Micronized and coarse drug powders with sizes of $5 - 10\,\mu m$ and $120 - 150\,\mu m$ were used as references. While micronization resulted in a 8-fold AUC enhancement with reference to the coarse suspension, an additional 2-fold AUC enhancement was observed for the nanosuspensions with reference to the micro-suspension. Larger C_{max} and shorter T_{max} of nanosuspensions indicated more rapid absorption of FF from the colloidal suspensions. This is a result which was likewise found in the present study. Li et al. (2009) report a lack of statistically significant differences in all PK parameters between the two nanosuspensions.

In the work of Xia et al. (2010) a wide particle size range was covered by six crystalline suspensions of nitrendipine. Their mean particle sizes were 200 nm, 629 nm, 2.7μm, 4.1μm, 20.2μm and 36.6μm. It could be criticized that the three smallest sized suspensions displayed very wide particle size distribution with clearly bi- or multimodal distributions. A PK study on rats was performed and incremental improvements in systemic exposure by a reduction in particle size were observed. AUC and C_{max} values of crystals with 200 nm to 20.2μm were significantly increased. The absolute bioavailabilities were 62 %, 52 %, 29 %, 27 %, 25 % and 10 % in order of increasing size.

Finally Wu et al. (2004) administered aprepitant suspensions with mean particle sizes of 120 nm, 480 nm, 1.9μm and 5.5μm to dogs. Incremental improvements in oral absorption correlated well with a reduction of particle size. A four-fold increase in AUC of the smallest suspension compared to the largest suspension (45-fold larger particles) was seen. Also the suspension with 480 nm particle size was able to increase the bioavailability, however, only a two-fold increase was observed. Hence the 120 nm suspension caused an additional two-fold bioavailability improvement compared to the 480 nm suspension. This result is in contrast to the studies of Wang et al. (2010); Li et al. (2009); Xia et al. (2010). They did not report an additional effect on systemic exposure once the crystal size reached the nanometer range.

The present study contributes two more investigations on the *in vivo* effects associated with incremental particle size reduction. The fenofibrate nanosuspension NS 140nm had significantly higher C_{max} than all other formulations. For compound AS suspensions a significantly higher C_{max} for NS 150nm compared
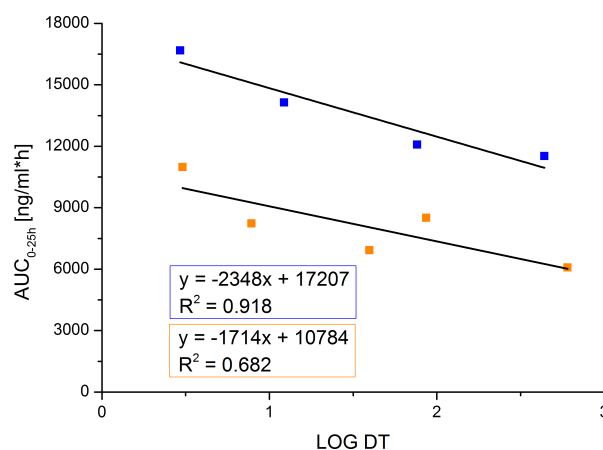
Figure 3.32: *In vitro-in vivo* correlation: Linear relationship between logarithmic dissolution time (LOG *DT*) and the *AUC* of fenofibrate (blue) and compound AS (orange) crystalline suspensions.

to the microsuspension was observed. C_{max} of NS 100nm was not significantly different from the microsuspension, however, the plasma concentration at 5 h was. No statistical differences were identified between NS 100nm and NS 150nm. Particle size reduction to a size of about $1\,\mu$m did not improve the bioavailability with reference to a particle size of about a size of $7 - 8\mu$m for both APIs (p < 0.05 for all tests).

In summary the presented studies demonstrated that a crystal size reduction to the nanometer scale improved the bioavailability of fenofibrate and compound AS. An additional effect in the comparison of two nanosuspensions was observed for fenofibrate, but not for compound AS.

3.8.3   In vitro-in vivo correlation

Following the concept of Xia et al. (2010) a linear regression analysis was performed on the logarithmic dissolution times (Log (DT)) with the *AUC* as a measure of bioavailability (Fig. 3.32). A good linear relationship was observed for fenofibrate (R^2 = 0.918). For compound AS the deviations between measured and fitted data are higher (R^2 = 0.682). However, the data points are evenly distributed around the fitted linear relation which suggests the possibility that a linear correlation might actually model the experimental data correctly.

3.8.4   Pharmacokinetic modeling & simulation

The effect of particle size reduction on *in vivo* PK was modeled with the GastroPlus[TM] software. The aim was to evaluate whether PK profiles could be correctly simulated and whether the nanofactor effect improves the simulation. The possibility to include the nanofactor effect into the ACAT model was offered by Simulations plus, Inc., because a faster dissolution and/or an enhanced solubility alone did not correctly simulate the absorption from nano-sized particles (section 1.2.3). The nanofactor effect allows for a local supersaturation at the apical membrane, leading to a steeper concentration gradient and thereby increasing absorption. It is based on the empirical model adjustment for each API.

Table 3.13 summarizes the simulation input parameters and some comments on the simulations setup are

Table 3.13: PK simulation with GastroPlus[TM]: input parameters.

Parameter		Fenofibrate / fenofibric acid	Compound AS
logP		5.29 *calc*	2.17 *obs*
pKa		–	*calc*[1]
Reference solubility	$[mg/ml]$	0.00029 *obs*	0.011 *obs*
Reference solubility pH		7.0 *calc*	5.8 *calc*
SGF solubility	$[mg/ml]$	0.00012 *obs*	0.0073 *obs*
FaSSIF solubility	$[mg/ml]$	0.01126 *obs*	0.0093 *obs*
FeSSIF solubility	$[mg/ml]$	0.03679 *obs*	0.03 *obs*
Bile salt solubilization ratio[2]		408000 *calc*	6928 *calc*
Caco-2 P_{app}	$[cm/s * 10^5]$	0.064 or 0.2 *obs*	0.031 *obs*
Simulated P_{eff} (Rat)	$[cm/s * 10^4]$	0.1500 or 0.3089 *calc*	0.0947 *calc*
Dose	$[mg]$	0.518	0.675
Dosage Form		Immediate release: Suspension	
Particle density	$[g/ml]$	1.2 *calc*	1.2 *calc*
Particle size distribution		*obs*[3]	*obs*[3]
Dissolution model		Johnson[4]	Wang-Flanagan[4]
Nanofactor[5]		0.2	0.1
Diffusion coefficient	$[cm^2/s * 10^5]$	0.67 *calc*	0.59 *calc*
Liver first pass extraction (FPE)	$[\%]$	3.9721 *calc*[6]	2.7072 *calc*
Fraction unbound in plasma (Fup)	$[\%]$	1.28 *calc*[6]	3.13 *calc*
Blood/Plasma concentration ratio		0.55 *calc*[6]	0.6 *calc*
Clearance CL	[l/h]	0.01277 *fit*	0.01279 *fit*
Volume of distribution V_c	$[l/kg]$	0.03631 *fit*	0.14417 *fit*
K12	$[1/h]$	9.2383 *fit*	0.51529 *fit*
K21	$[1/h]$	2.8343 *fit*	1.7645 *fit*
K13	$[1/h]$	0.3937 *fit*	0.00779 *fit*
K31	$[1/h]$	0.07277 *fit*	0.20788 *fit*
Compartmental PK model		3 compartments	3 compartments
ASF model[7]		Opt logD Model SA/V 6.1	
ACAT model		Rat - physiological - fasted[8]	
		with stomach transit time 0.05 h	

obs: observed/experimental value

calc: calculated by GastroPlus[TM]

fit: fitted by the GastroPlus[TM] PKPlus[TM] module from FFA/AS i.v. experimental profiles

[1] GastroPlus[TM] built in solubility-pH function

[2] solubility and diffusion coefficient adjusted for bile salt effect

[3] SLS particle size distribution with $9 - 16$ bins

[4] diffusion layer thickness adjusted to changing radius up to maximum $30\,\mu$m, particle shape factor 1

[5] manually adjusted with GastroPlus[TM] default for interfacial tension 0.05 J/m^2

[6] calculated by GastroPlus[TM] for FFA molecule

[7] The absorption scale factor (ASF) provides the absorption model. The applied model (default) incorporates a logD-dependent calibration of ASF based on human and rat permeability/fraction absorbed data.

[8] animal weight 0.25 kg

given here. The orally administered suspensions were characterized by SLS particle size measurements (section 3.1.1) and the obtained particle size distributions are used in the simulations. Experimental values for the physiochemical properties of APIs (solubility, permeability) were used as far as available and all other values were predicted by the ADMET Predictor$^{\text{TM}}$. The Johnson and Wang-Flanagan dissolution models were applied to simulate *in vivo* dissolution in different GI compartments. The observed i.v. concentration-time profiles were used to obtain pharmacokinetic parameters. Different settings (0-1) were tried for the nanofactor and the value which resulted in the best simulation for the smallest nano-sized formulations was selected for all formulations. For fenofibrate the modeling had an additional dimension: the conversion of the prodrug fenofibrate towards fenofibric acid. In the *in vitro* permeability and the *in vivo* PK studies the metabolization was already complete after intestinal absorption. This observation was accounted for in the model by applying the physiochemical parameters of FF for all steps prior to absorption and by applying the pharmacokinetic properties of FFA for all steps following absorption (elimination).

All simulation results are shown in Figure 3.33, Figure 3.34 and Table 3.14. Fenofibrate simulations were started using the pure crystalline API permeability $P_{app} = 0.64 * 10^{-6} \, cm/s$ (Tab. 3.8). Without the nanofactor effect the AUC of all formulations was underestimated and the observed shift of T_{max} could not be modeled. The nanofactor improved the AUC prediction and a clearly better fit was achieved for NS 140nm and NS 270nm. The discrimination between the four formulations corresponding to particle size was much better simulated. Now T_{max} decreased with deceasing particle size. It was, however, still too long especially for NS 140nm.

Since a higher permeability in the Caco-2 model was observed for nano-sized FF formulations than for pure crystalline API, the permeability was set to $P_{app} = 2 * 10^{-6} \, cm/s$ (average, rounded value measured for NS 140nm/NS 270nm, Tab. 3.11). This improved the overall predictivity of the simulation indicated by an average $R^2 = 0.761$ ($2 * 10^{-6} \, cm/s$) versus an average $R^2 = 0.652$ ($0.64 * 10^{-6} \, cm/s$). The profiles of the two smaller sized suspensions with an early T_{max} were much better simulated. However, the extent of absorption (AUC, F_{abs}) was now overestimated for the two larger sized suspensions. Inclusion of the nanofactor effect into the simulation greatly improved the prediction of the NS 140nm concentration-time profile. However, the overestimation of C_{max} and AUC of the other formulations, which was already observed without the nanofactor, was amplified.

In summary it was difficult to identify the overall best model for the simulation of the FF concentration-time profiles of all formulations. An inappropriate representation of the intestinal metabolization by the applied model might be one reason.

Compound AS simulations were started using the permeability $P_{app} = 0.22 * 10^{-6} \, cm/s$, which was determined for the AS microsuspension (Tab 3.9). The average R^2 values for all five formulations were 0.671 without the nanofactor and 0.786 with the nanofactor (data not shown). Application of the permeability $P_{app} = 0.31 * 10^{-6} \, cm/s$ which was determined for AS NS 150nm improved the correlation of predicted and observed plasma profiles for every single formulation. The average coefficients of determination were increased to $R^2 = 0.750$ without the nanofactor and $R^2 = 0.840$ with the nanofactor (Tab. 3.14). The inclusion of the nanofactor effect into the model clearly improved the predictivity of the model for NS 100nm and NS 150nm. The differences for NS 860nm, NS 1320nm and MS 6.8 μm were

less pronounced. While the nanofactor effect caused an overestimation of the microsuspensions bioavailability, it is not possible to identify the better model for medium sized formulations like NS 860nm and NS 1320nm.

In summary the simulation of the concentration-time profiles for AS formulations was remarkably good and the inclusion of the nanofactor effect clearly improved the overall suitability of the model.

One point which remains to be discussed is that no relevant differences between the nano-sized formulations (FF NS 140nm vs FF NS 270nm and AS NS 100nm vs AS NS 150nm) were seen in the simulations. However, they were observed *in vivo* (Fig. 3.30). The use of the nanofactor effect did not make a difference. A reason might be that a model adjustment allowing for supersaturation effects by nanocrystal alone is not sufficient. It should also be kept in mind that it is an empirical approach. Recently the challenge of nanoparticle absorption/dissolution modeling was also addressed by Johnson (2012). He modeled dissolution by the Johnson and Wang-Flanagan dissolution models and incorporated a particle size adjusted solubility according to the Ostwald-Freundlich equation. Even though his model was hence comprising many parameters it was not sufficient to explain observed differences between absorption from nano and micron sized particles. He confirmed that the dissolution rate enhancement alone cannot explain nanocrystal absorption profiles.

While the theoretical implications of particle size reduction on dissolution are already quite well represented in the advanced dissolution models, it becomes obvious that the implications on API absorption are still poorly investigated and understood. The present investigation confirms that the nanofactor effect can greatly improve the simulation of the *in vivo* behavior of orally applied nano-sized rapidly dissolving particles. However, it does not have the power to discriminate between different nano-sized formulations, which indicates that also other effects might contribute to the observed increase in extent of API absorption. Also a more mechanistic approach of taking into account supersaturation phenomena is required.

3.8.5 Summary and conclusions

The pharmacokinetic studies on suspensions with incrementally reduced particle size are an important contribution to the discussion about the *in vivo* effects of particle size reduction, since similarly designed studies are rare. The presented studies demonstrated that a crystal particle size reduction to the nanometer scale improved the relative bioavailability with reference to a microsuspension. This was true for both APIs, fenofibrate and compound AS. An additional bioavailability enhancing effect when two nanosuspensions are compared was only observed for fenofibrate, but not for compound AS.

The outstanding characteristics of the presented studies are that the suspensions are narrowly distributed and that dissolution data are available for all formulations. A good linear correlation of the logarithmic dissolution times (Log (DT)) with the *AUC* was observed. The Advanced Compartmental Absorption and Transit (ACAT) simulation model was used to simulate plasma concentration-time profiles with GastroPlus^{TM}. The use of the nanofactor effect, which offers an empirical model adjustment by allowing for nanocrystal dissolution exceeding the solubility limit, improved the predictivity of the model for the simulation of the absorption of API delivered as nano sized crystals. However, the model did not represent the *in vivo* observed discrimination between the smallest sized formulations.

(a) NS 140nm

(b) NS 270nm
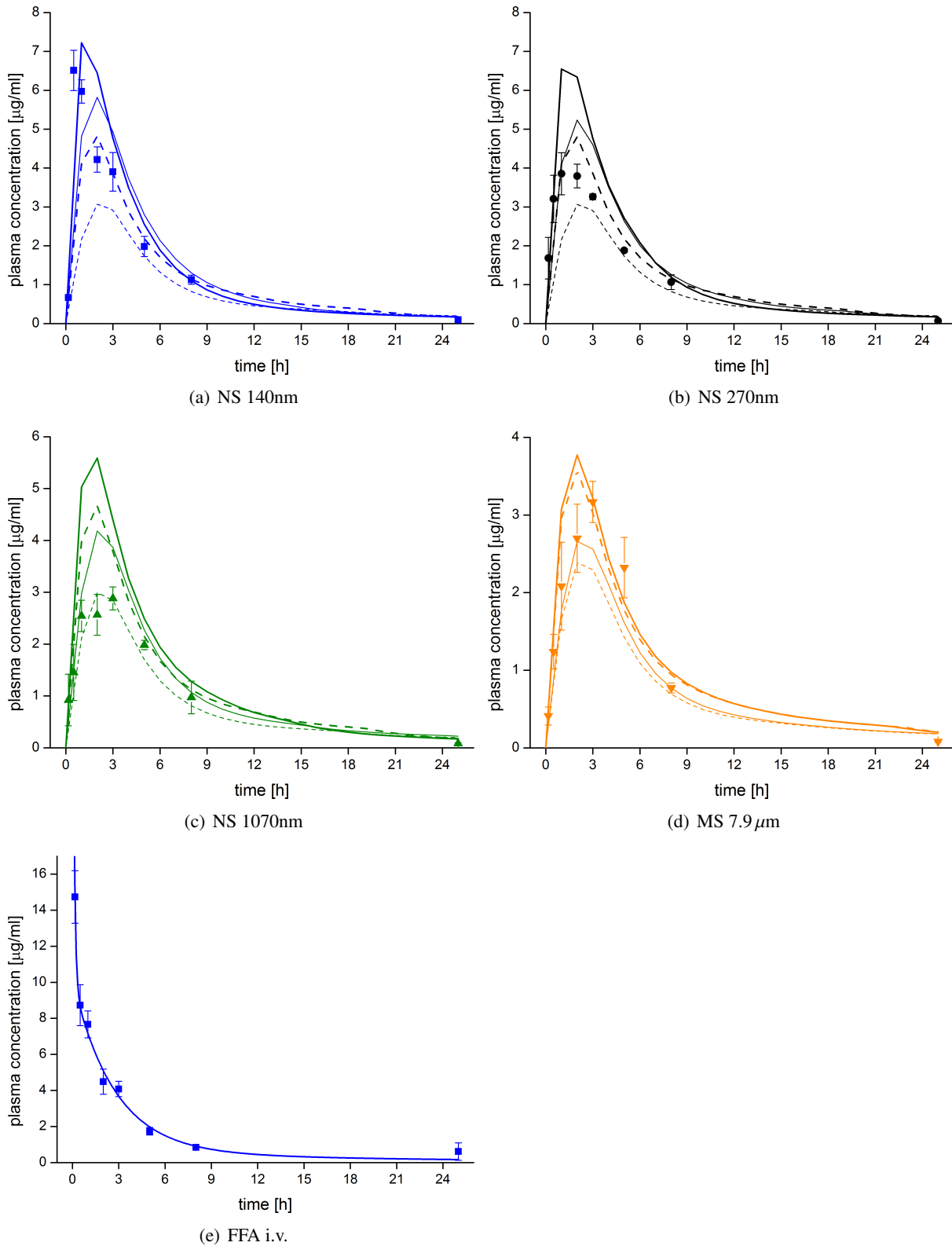
(c) NS 1070nm

(d) MS 7.9 μm

(e) FFA i.v.

Figure 3.33: FF simulated plasma concentration-time curves (lines) and experimental data (symbols). Simulation parameters: Caco-2 $P_{app} = 0.064 * 10^{-5}\, cm/s$ (thin lines) or Caco-2 $P_{app} = 0.2 * 10^{-5}\, cm/s$ (bold lines); with nanofactor 0.2 (compact lines) or without nanofactor (dashed lines).
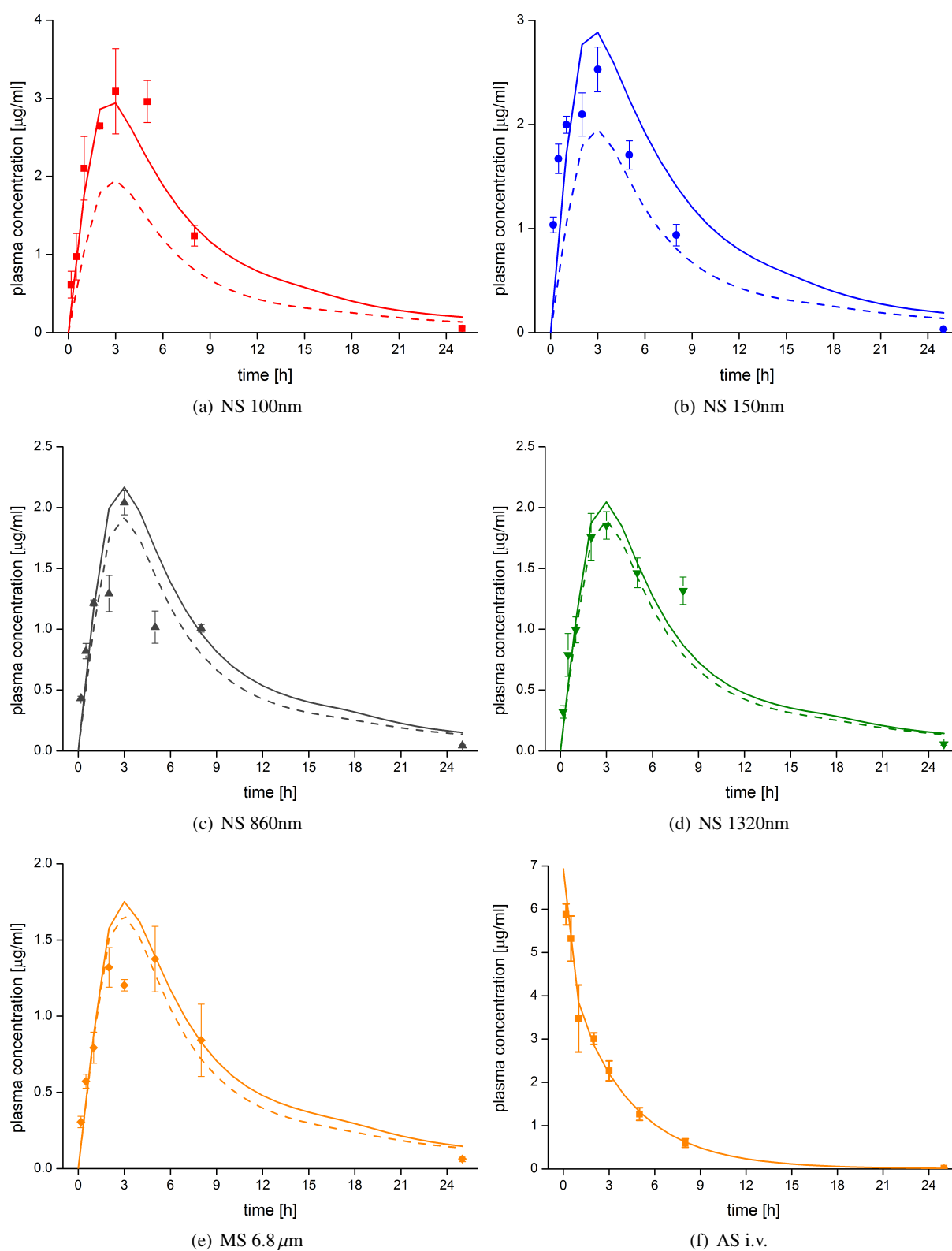
(a) NS 100nm

(b) NS 150nm

(c) NS 860nm

(d) NS 1320nm

(e) MS 6.8 μm

(f) AS i.v.

Figure 3.34: Compound AS simulated plasma concentration-time curves (lines) and experimental data (symbols). Simulation parameters: Caco-2 $P_{app} = 0.031 * 10^{-5}\,cm/s$; with nanofactor 0.1 (compact lines) or without nanofactor (dashed lines).

Table 3.14: PK parameters of FF and AS formulations simulated by the ACAT model with different settings.

Formulation	R^2	T_{max} [h]		C_{max} [ng/ml]		$AUC_{0\to25h}$ [ng/ml*h]		F_{abs} [%]		
			Small numbers denote deviations [*] *of predicted from observed value in %*							
Fenofibrate										
FFA i.v.	0.994	0	–	57060	+287[*]	37500	-10	100	±0	
$P_{app} = 0.064 * 10^{-5}\ cm/s$, **without nanofactor**										
NS 140nm	0.376	2.2	+340	3077	-53	21500	-38	59	-29	
NS 270nm	0.589	2.2	+120	3068	-20	21400	-27	59	-16	
NS 1070nm	0.885	2.2	-27	3001	+4	21000	-16	58	-4	●
MS 7.9µm	0.758	2.3	-23	2419	-24	17400	-27	48	-16	
$P_{app} = 0.064 * 10^{-5}\ cm/s$, **with nanofactor 0.2**										
NS 140nm	0.607	1.8	+260	5842	-10	34600	±0	93	+12	
NS 270nm	0.782	1.9	+90	5239	+36	32700	+12	88	+26	
NS 1070nm	0.802	2.1	-30	4183	+45	27700	+11	76	+26	
MS 7.9µm	0.854	2.3	-23	2695	-15	19100	-20	53	-8	
$P_{app} = 0.2 * 10^{-5}\ cm/s$, **without nanofactor**										
NS 140nm	0.548	1.5	+200	4872	-25	30500	-12	83	-1	
NS 270nm	0.867	1.6	+60	4850	+26	30400	+4	82	+18	●
NS 1070nm	0.733	1.7	-43	4719	+64	29900	+20	81	+35	
MS 7.9µm	0.854	1.8	-40	3590	+13	24300	+2	67	+17	●
$P_{app} = 0.2 * 10^{-5}\ cm/s$, **with nanofactor 0.2**										
NS 140nm	0.836	1.2	+140	7339	+13	35900	+4	96	+16	●
NS 270nm	0.736	1.4	+40	6869	+78	35700	+22	96	+37	
NS 1070nm	0.658	1.6	-47	5729	+99	33600	+34	90	+51	
MS 7.9µm	0.843	1.9	-37	3782	+19	25200	+6	69	+21	
Compound AS										
AS i.v.	0.983	0	–	6936	+18	19500	-11	100	±0	
$P_{app} = 0.031 * 10^{-5}\ cm/s$, **without nanofactor**										
NS 100nm	0.569	2.9	-3	1955	-37	16200	-45	32	-37	
NS 150nm	0.612	2.9	-3	1955	-23	16200	-27	32	-14	
NS 860nm	0.821	2.9	-3	1921	-6	16000	-14	31	-2	●
NS 1320nm	0.881	2.9	-3	1899	+2	15800	-31	31	-20	
MS 6.8µm	0.868	2.9	-42	1664	+21	14300	-13	28	±0	●
$P_{app} = 0.031 * 10^{-5}\ cm/s$, **with nanofactor 0.1**										
NS 100nm	0.896	2.6	-13	2988	-3	26200	-12	51	+2	●
NS 150nm	0.744	2.7	-10	2913	+15	26100	+17	51	+38	●
NS 860nm	0.800	2.8	-7	2172	+6	18900	+1	37	+15	
NS 1320nm	0.901	2.8	-7	2050	+11	17300	-25	34	-13	●
MS 6.8µm	0.858	2.9	-42	1751	+27	16000	-3	31	+12	

[*] *Deviation = (PredictedValue − ObservedValue)/ObservedValue * 100%*   ● best fit

The presented investigations on the relation of *in vitro* and *in vivo* data and on pharmacokinetic simulations are a first approach. It is planed to continue analysis of the experimental data for example by making use of the GastroPlus$^{\text{TM}}$ optimization tool. It mathematically fits model parameters to experimental data and allows for IVIVC investigations.

4

Summary and Outlook

Summary

The aim of this thesis was a biopharmaceutical characterization of oral nanocrystal formulations including solubility, dissolution, permeation and *in vivo* pharmacokinetic studies. Crystalline suspensions with an incrementally reduced particle size were developed to explicitly study the effect of particle size on the biopharmaceutical properties. Size reduction had by far the strongest influence on dissolution kinetics. A linear correlation of the logarithmic *in vitro* dissolution times with *in vivo* bioavailability was observed.

In the following the results and conclusions are summarized more in detail:
Crystalline nanosuspensions and microsuspensions of two drug substances, fenofibrate and the Merck Serono compound AS, were prepared. An incremental particle size reduction was performed by using the method of wet media milling. Nine fenofibrate and seven compound AS suspensions were prepared and all of them were aqueous suspensions of 20% API, 2.5% HPMC and 0.1% DOSS. The suspensions covered a wide particle size range (100 nm to 8 μm) and exhibited narrow particle size distributions.
It was challenging to determine the solubility and dissolution of nanocrystal formulations. Very small particles with rapid dissolution kinetics complicated the separation of solid from dissolved material. Therefore, this work focused on noninvasive analytical techniques which avoid the critical separation step. A method of monitoring the light scattering intensity with a Zetasizer Nano ZS$^{\text{TM}}$ instrument was developed and applied to measure solubilities and dissolution kinetics of nanocrystalline API.
Also alternative methods were evaluated for their suitability to assess nanocrystal dissolution. Modifications of the conventional USP II method by using 0.02 μm syringe filters or dialysis membranes did not improve its applicability for nanocrystal dissolution. Among the tested noninvasive in situ an-

alytical techniques (nanoparticle tracking analysis, NMR and Raman spectroscopy, isothermal titration calorimetry) the light scattering approach was the most promising one. It measures the drop of light scattering intensity during dissolution, which is caused by a reduction in particle number and size.

The light scattering dissolution method allowed for a continuous and fast nanocrystal dissolution assessment in a straightforward small scale experimental setup. Dissolution results were in good agreement with a conventional dissolution technique (USP II apparatus with sample filtration). The new approach was applicable to differentiate between different particle sizes and concentration gradients with a satisfying sensitivity and reproducibility. The nanocrystal size most suitable for the light scattering method was $100 - 500$ nm (particle diameter) and the method was still applicable up to a size of 1μm. Dissolution times as short as 90 s could be determined.

The experimentally obtained dissolution curves were successfully fitted by a biexponential decay model. This allowed for the calculation of dissolution times (time, when only 1 % of initial scattering intensity remains). The results of light scattering dissolution were in good agreement with the Noyes-Whitney dissolution model.

While a particle size reduction greatly accelerated the dissolution process, only moderately enhanced solubilities of nanosuspensions were observed ($10 - 20$ % for particles < 200 nm). This result highlights accelerated dissolution as main factor of the bioavailability enhancement through nanocrystals.

In Caco-2 permeability studies the effect of particle size on the permeability was evaluated. An assay with vertical monolayer arrangement was compared to the classical horizontal assay. The vertical setup did not improve the discriminative power and the adjustment of standardized experimental conditions was difficult. Therefore, the horizontal setup was selected for further experiments. A variation of apical transport medium by using a biorelevant medium instead of a classical buffered salt solution did not alter the permeabilities essentially.

For compound AS it was observed that a smaller particle size improved the permeability. This is an expected result, due to a moderately enhanced solubility and a markedly faster dissolution of the smaller particles. A fast dissolution guarantees for a constant high concentration of dissolved API at the absorption site and enables a good utilization of the APIs permeability potential. On the other hand a positive effect of size reduction on the permeability was not observed for fenofibrate. The findings in this study suggest that the enzymatic fenofibrate conversion in the Caco-2 assay might interfere with the effects of particle size reduction. The metabolite, fenofibric acid, has a higher solubility than fenofibrate and an equal permeability. A parallel increase of permeability with apical fenofibric acid concentration indicates that fenofibric acid might be the substrate mainly permeating across the epithelial barrier. The metabolization might play a crucial role and was not sufficiently investigated in this study.

In vivo pharmacokinetic studies of the oral administration of suspensions to rats completed the biopharmaceutical characterization. The *in vivo* studies demonstrated that a crystal size reduction to the nanometer scale improved the relative bioavailability with reference to a microsuspension. This was true for both APIs, fenofibrate and compound AS. The presented pharmacokinetic studies on several suspensions with incrementally reduced particle size give an important contribution to the discussion about the *in vivo* effects of particle size reduction, since similarly designed studies are rare. The outstanding characteristics of the presented studies are that the suspensions are narrowly distributed and

that dissolution data are available for all formulations.

The presented work covers a thorough particle size distribution analysis, solubility, dissolution, permeation and *in vivo* pharmacokinetic investigation of micro- and nanosuspensions of two drug substances. These data are very useful to investigate the *in vitro-in vivo* relation of oral nanocrystal formulations. In this work a good linear correlation of the logarithmic dissolution times to the bioavailability was demonstrated. Furthermore plasma concentration-time profiles were successfully simulated using the Advanced Compartmental Absorption and Transit (ACAT) model. For nanocrystal formulations the fit of simulated to observed profiles was improved by applying the nanofactor effect implemented in the ACAT model.

Outlook

The application of the light scattering method for nanocrystal solubility and dissolution studies of a greater number of APIs and formulations will help to better characterize the strengths and limitations of the new methods and to demonstrate a broad applicability.

Regarding the nanocrystal dissolution method future studies covering the following aspects would be interesting:

- A use of the light scattering dissolution method in later development phases and for quality control purposes would require an implementation of strategies to cope with undissolvable excipients due to their influence on light scattering measurements. In this work the successful application of prefiltration steps was demonstrated for the measurement of nanocrystal dissolution of the market product EMEND®.

- An evaluation of dissolution results on the basis of advanced dissolution models will help to gain further mechanistic insight from experimental data. Wang-Flanagan and Johnson developed advanced dissolution models taking into account particle shrinking and associated changes of the diffusion layer thickness and particle solubility. All these parameters are considered constant in the Noyes-Whitney dissolution model. Furthermore calculations with particle size distributions rather than an average particle size will help to refine the model.

- It would be interesting to theoretically model the course of light scattering intensity during dissolution. The decreasing scattering intensity is caused by changes in particle number and particle size. Depending on size the scattering properties of a particle are likely to change during dissolution.

- Another noninvasive analytical technique, the isothermal titration calorimetry, showed a potential for the dissolution testing of nanocrystals. Further studies with different formulations under different conditions will clarify the applicability of this method. A comparison of results to the light scattering method would be interesting.

Regarding the Caco-2 permeability studies on fenofibrate formulations a thorough investigation on the extent and influence of fenofibric acid formation during the assay is required. An evaluation of the

esterase activity or a specific inhibition of esterases would help to analyze the hydrolytic effect and its influence on fenofibrate permeability. Furthermore it would be interesting to extend the experiments on particle formulations, which aggregate in the transport media. The high bioavailability of compound AS formulation NS 100nm showed that an *in vitro* instability in physiologically relevant intestinal media was not translating into poor *in vivo* performance. The performance of aggregated NS 100nm nanocrystals in an *in vitro* permeability experiment will reveal if a disaggregation caused by the intestinal motility is responsible for good *in vivo* results.

The presented investigations on the relation of *in vitro* and *in vivo* data are a first approach. A deeper analysis is planned to be performed using the Advanced Compartmental Absorption and Transit (ACAT) Simulation Model implemented in the GastroPlus$^{\text{TM}}$ software.

Bibliography

M. M. Abdel-Mottaleb and A. Lamprecht. Standardized in vitro drug release test for colloidal drug carriers using modified USP dissolution apparatus I. *Drug Dev Ind Pharm*, 37(2):178–84, 2011.

M. Albinus. *Hagers Handbuch der pharmazeutischen Praxis Band 8 Stoffe E - O*. Springer Verlag, 5 edition, 1993.

P. K. Aldridge, D. W. Melvin, B. A. Williams, K. Bratin, L. J. Kostek, and S. S. Sekulic. A robotic dissolution system with on-line fiber-optic UV analysis. *J Pharm Sci*, 84(8):909–14, 1995.

D. E. Alonzo, G. G. Zhang, D. Zhou, Y. Gao, and L. S. Taylor. Understanding the behavior of amorphous pharmaceutical systems during dissolution. *Pharm Res*, 27(4):608–18, 2010.

G. L. Amidon, H. Lennernas, V. P. Shah, and J. R. Crison. A theoretical basis for a biopharmaceutic drug classification: the correlation of in vitro drug product dissolution and in vivo bioavailability. *Pharm Res*, 12(3):413–20, 1995.

K. Anhalt, S. Geissler, M. Harms, M. Weigandt, and G. Fricker. Development of a new method to assess nanocrystal dissolution based on light scattering. *Pharm Res*, 29(10):2887–901, 2012.

P. Artursson, K. Palm, and K. Luthman. Caco-2 monolayers in experimental and theoretical predictions of drug transport. *Adv Drug Deliv Rev*, 46(1-3):27–43, 2001.

P. V. Balimane and S. Chong. Evaluation of permeability and P-glycoprotein interactions: Industry outlook. In R. Krishna and L. Yu, editors, *Biopharmaceutics Applications in Drug Development*, pages 101–138. Springer US, 2008.

P. V. Balimane, Y. H. Han, and S. Chong. Current industrial practices of assessing permeability and p-glycoprotein interaction. *AAPS J*, 8(1):E1–13, 2006.

U. Bhardwaj and D. J. Burgess. A novel USP apparatus 4 based release testing method for dispersed systems. *Int J Pharm*, 388(1-2):287–94, 2010.

K. Bouchemal. New challenges for pharmaceutical formulations and drug delivery systems characterization using isothermal titration calorimetry. *Drug Discov Today*, 13(21-22):960–72, 2008.

A. Braun, S. Hammerle, K. Suda, B. Rothen-Rutishauser, M. Gunthert, S. D. Kramer, and H. Wunderli-Allenspach. Cell cultures as tools in biopharmacy. *Eur J Pharm Sci*, 11 Suppl 2:S51–60, 2000.

H. G. Brittain. Particle-size distribution IV. determination by laser-light scattering. *Pharm Tech*, 27(10): 102–114, 2003.

J. Brouwers, J. Tack, F. Lammert, and P. Augustijns. Intraluminal drug and formulation behavior and integration in in vitro permeability estimation: a case study with amprenavir. *J Pharm Sci*, 95(2): 372–83, 2006.

E. Brunner. Reaktionsgeschwindigkeit in Heterogenen Systemen. *Z Physik Chem*, 47(1):56–102, 1904.

P. Buch. *Solubility and permeability as in vitro predictors for in vivo performance of fenofibrate IR solid dosage forms*. phdthesis, 2010.

P. Buch, P. Langguth, M. Kataoka, and S. Yamashita. IVIVC in oral absorption for fenofibrate immediate release tablets using a dissolution/permeation system. *J Pharm Sci*, 98(6):2001–9, 2009.

S. T. Buckley, S. M. Fischer, G. Fricker, and M. Brandl. In vitro models to evaluate the permeability of poorly soluble drug entities: challenges and perspectives. *Eur J Pharm Sci*, 45(3):235–50, 2012.

F. Buyukozturk, J. C. Benneyan, and R. L. Carrier. Impact of emulsion-based drug delivery systems on intestinal permeability and drug release kinetics. *J Control Release*, 142(1):22–30, 2010.

M. J. Chapman. Pharmacology of fenofibrate. *Am J Med*, 83(5B):21–5, 1987.

N. Charalampopoulos, K. Avgoustakis, and C. G. Kontoyannis. Differential pulse polarography: a suitable technique for monitoring drug release from polymeric nanoparticle dispersions. *Anal Chim Acta*, 491:57–62, 2003.

A. Chatterjee, S. P. Moulik, S. K. Sanyal, B. K. Mishra, and P. M. Puri. Thermodynamics of micelle formation of ionic surfactants: A critical assessment for sodium dodecyl sulfate, cetyl pyridinium chloride and dioctyl sulfosuccinate (Na salt) by microcalorimetric, conductometric, and tensiometric measurements. *J Phys Chem B*, 105(51):12823–12831, 2001.

M. V. Chaubal and C. Popescu. Conversion of nanosuspensions into dry powders by spray drying: a case study. *Pharm Res*, 25(10):2302–8, 2008.

C. S. Chen and C. W. Brown. A drug dissolution monitor employing multiple fiber optic probes and a UV/visible diode array spectrophotometer. *Pharm Res*, 11(7):979–83, 1994.

Y. Chen, Y. Lu, J. Chen, J. Lai, J. Sun, F. Hu, and W. Wu. Enhanced bioavailability of the poorly water-soluble drug fenofibrate by using liposomes containing a bile salt. *Int J Pharm*, 376(1-2):153–60, 2009.

P. Costa and J. M. Sousa Lobo. Modeling and comparison of dissolution profiles. *Eur J Pharm Sci*, 13 (2):123–33, 2001.

M. T. Crisp, C. J. Tucker, T. L. Rogers, 3rd Williams, R. O., and K. P. Johnston. Turbidimetric measurement and prediction of dissolution rates of poorly soluble drug nanocrystals. *J Control Release*, 117 (3):351–9, 2007.

A. Dahan, J. M. Miller, A. Hoffman, G. E. Amidon, and G. L. Amidon. The solubility-permeability interplay in using cyclodextrins as pharmaceutical solubilizers: mechanistic modeling and application to progesterone. *J Pharm Sci*, 99(6):2739–49, 2010.

A. Dokoumetzidis, V. Papadopoulou, and P. Macheras. Analysis of dissolution data using modified versions of Noyes-Whitney equation and the Weibull function. *Pharm Res*, 23(2):256–61, 2006.

J. B. Dressman, G. L. Amidon, C. Reppas, and V. P. Shah. Dissolution testing as a prognostic tool for oral drug absorption: immediate release dosage forms. *Pharm Res*, 15(1):11–22, 1998.

M. M. Elsayed and G. Cevc. Turbidity spectroscopy for characterization of submicroscopic drug carriers, such as nanoparticles and lipid vesicles: size determination. *Pharm Res*, 28(9):2204–22, 2011.

V. Filipe, A. Hawe, and W. Jiskoot. Critical evaluation of nanoparticle tracking analysis (NTA) by NanoSight for the measurement of nanoparticles and protein aggregates. *Pharm Res*, 27(5):796–810, 2010.

L. Fossati, R. Dechaume, E. Hardillier, D. Chevillon, C. Prevost, S. Bolze, and N. Maubon. Use of simulated intestinal fluid for Caco-2 permeability assay of lipophilic drugs. *Int J Pharm*, 360(1-2): 148–55, 2008.

H. Freundlich. *Colloid and Capillary Chemistry*. E. P. Dutton and Company, New York, 1923.

G. Fricker and D. S. Miller. Relevance of multidrug resistance proteins for intestinal drug absorption in vitro and in vivo. *Pharmacol Toxicol*, 90(1):5–13, 2002.

E. Galia, E. Nicolaides, D. Horter, R. Lobenberg, C. Reppas, and J. B. Dressman. Evaluation of various dissolution media for predicting in vivo performance of class I and II drugs. *Pharm Res*, 15(5):698–705, 1998.

C. Galli. Experimental determination of the diffusion boundary layer width of micron and submicron particles. *Int J Pharm*, 313(1-2):114–22, 2006.

Z. Gao. Mathematical modeling of variables involved in dissolution testing. *J Pharm Sci*, 100(11): 4934–4942, 2011.

G. E. Granero, C. Ramachandran, and G. L. Amidon. Dissolution and solubility behavior of fenofibrate in sodium lauryl sulfate solutions. *Drug Dev Ind Pharm*, 31(9):917–22, 2005.

A. Hanafy, H. Spahn-Langguth, G. Vergnault, P. Grenier, M. Tubic Grozdanis, T. Lenhardt, and P. Langguth. Pharmacokinetic evaluation of oral fenofibrate nanosuspensions and SLN in comparison to conventional suspensions of micronized drug. *Adv Drug Deliv Rev*, 59(6):419–26, 2007.

J. H. Hanks and R. E. Wallace. Relation of oxygen and temperature in the preservation of tissues by refrigeration. *Proc Soc Exp Biol Med*, 71(2):196–200, 1949.

A. Heinz, K. C. Gordon, C. M. McGoverin, T. Rades, and C. J. Strachan. Understanding the solid-state forms of fenofibrate – a spectroscopic and computational study. *Eur J Pharm Biopharm*, 71(1):100–8, 2009.

A. Helle, S. Hirsjarvi, L. Peltonen, J. Hirvonen, S. K. Wiedmer, and T. Hyotylainen. Novel, dynamic on-line analytical separation system for dissolution of drugs from poly(lactic acid) nanoparticles. *J Pharm Biomed Anal*, 51(1):125–30, 2010.

D. Heng, D. J. Cutler, H. K. Chan, J. Yun, and J. A. Raper. What is a suitable dissolution method for drug nanoparticles? *Pharm Res*, 25(7):1696–701, 2008.

I. J. Hidalgo. Assessing the absorption of new pharmaceuticals. *Curr Top Med Chem*, 1(5):385–401, 2001.

I. J. Hidalgo, K. M. Hillgren, G. M. Grass, and R. T. Borchardt. Characterization of the unstirred water layer in caco-2 cell monolayers using a novel diffusion apparatus. *Pharm Res*, 8(2):222–7, 1991.

W. I. Higuchi and E. N. Hiestand. Dissolution rates of finely divided drug powders. I. effect of a distribution of particle sizes in a diffusion-controlled process. *J Pharm Sci*, 52:67–71, 1963.

W. I. Higuchi, E. L. Rowe, and E. N. Hiestand. Dissolution rates of finely divided drug powders. II. micronized methyl-prednisolone. *J Pharm Sci*, 52:162–4, 1963.

R. J. Hintz and K. C. Johnson. The effect of particle size distribution on dissolution rate and oral absorption. *Int J Pharm*, 51(1):9–17, 1989.

A. W. Hixson and J. H. Crowell. Dependence of reaction velocity upon surface and agitation I – theoretical consideration. *Ind Eng Chem*, 23:923–931, 1931.

W. Huang, S. L. Lee, and L. X. Yu. Mechanistic approaches to predicting oral drug absorption. *AAPS J*, 11(2):217–24, 2009.

I. Hubatsch, E. G. Ragnarsson, and P. Artursson. Determination of drug permeability and prediction of drug absorption in Caco-2 monolayers. *Nat Protoc*, 2(9):2111–9, 2007.

F. Ingels, S. Deferme, E. Destexhe, M. Oth, G. Van den Mooter, and P. Augustijns. Simulated intestinal fluid as transport medium in the Caco-2 cell culture model. *Int J Pharm*, 232(1-2):183–92, 2002.

F. Ingels, B. Beck, M. Oth, and P. Augustijns. Effect of simulated intestinal fluid on drug permeability estimation across Caco-2 monolayers. *Int J Pharm*, 274(1-2):221–32, 2004.

F. M. Ingels and P. F. Augustijns. Biological, pharmaceutical, and analytical considerations with respect to the transport media used in the absorption screening system, Caco-2. *J Pharm Sci*, 92(8):1545–58, 2003.

S. Jamzad and R. Fassihi. Role of surfactant and pH on dissolution properties of fenofibrate and glipizide – a technical note. *AAPS PharmSciTech*, 7(2):E33, 2006.

Z. Jia, P. Lin, Y. Xiang, X. Wang, J. Wang, X. Zhang, and Q. Zhang. A novel nanomatrix system consisted of colloidal silica and pH-sensitive polymethylacrylate improves the oral bioavailability of fenofibrate. *Eur J Pharm Biopharm*, 79(1):126–34, 2011.

J. Jinno, N. Kamada, M. Miyake, K. Yamada, T. Mukai, M. Odomi, H. Toguchi, G. G. Liversidge, K. Higaki, and T. Kimura. Effect of particle size reduction on dissolution and oral absorption of a poorly water-soluble drug, cilostazol, in beagle dogs. *J Control Release*, 111(1-2):56–64, 2006.

J. Jinno, N. Kamada, M. Miyake, K. Yamada, T. Mukai, M. Odomi, H. Toguchi, G. G. Liversidge, K. Higaki, and T. Kimura. In vitro-in vivo correlation for wet-milled tablet of poorly water-soluble cilostazol. *J Control Release*, 130(1):29–37, 2008.

K. C. Johnson. Comparison of methods for predicting dissolution and the theoretical implications of particle-size-dependent solubility. *J Pharm Sci*, 101(2):681–9, 2012.

A. Judefeind and Melgardt M. de Villiers. Drug loading into and in vitro release from nanosized drug delivery systems. In Melgardt M. de Villiers, Pornanong Aramwit, and Glen S. Kwon, editors, *Nanotechnology in Drug Delivery*. Springer, New York, 2009.

D. Juenemann, H. Bohets, M. Ozdemir, R. de Maesschalck, K. Vanhoutte, K. Peeters, L. Nagels, and J. B. Dressman. Online monitoring of dissolution tests using dedicated potentiometric sensors in biorelevant media. *Eur J Pharm Biopharm*, 78(1):158–65, 2011a.

D. Juenemann, E. Jantratid, C. Wagner, C. Reppas, M. Vertzoni, and J. B. Dressman. Biorelevant in vitro dissolution testing of products containing micronized or nanosized fenofibrate with a view to predicting plasma profiles. *Eur J Pharm Biopharm*, 77(2):257–64, 2011b.

D. Junemann and J. Dressman. Analytical methods for dissolution testing of nanosized drugs. *J Pharm Pharmacol*, 64(7):931–43, 2012.

J. Karlsson and P. Artursson. A new diffusion chamber system for the determination of drug permeability coefficients across the human intestinal epithelium that are independent of the unstirred water layer. *Biochim Biophys Acta - Biomembranes*, 1111(2):204–210, 1992.

J. Karlsson, A. Ungell, J. Grasjo, and P. Artursson. Paracellular drug transport across intestinal epithelia: influence of charge and induced water flux. *Eur J Pharm Sci*, 9(1):47–56, 1999.

M. Kataoka, Y. Masaoka, Y. Yamazaki, T. Sakane, H. Sezaki, and S. Yamashita. In vitro system to evaluate oral absorption of poorly water-soluble drugs: simultaneous analysis on dissolution and permeation of drugs. *Pharm Res*, 20(10):1674–80, 2003.

M. Kataoka, Y. Masaoka, S. Sakuma, and S. Yamashita. Effect of food intake on the oral absorption of poorly water-soluble drugs: in vitro assessment of drug dissolution and permeation assay system. *J Pharm Sci*, 95(9):2051–61, 2006.

M. Kataoka, K. Sugano, C. da Costa Mathews, J. W. Wong, K. L. Jones, Y. Masaoka, S. Sakuma, and S. Yamashita. Application of dissolution/permeation system for evaluation of formulation effect on oral absorption of poorly water-soluble drugs in drug development. *Pharm Res*, 29(6):1485–94, 2012.

A. M. Kaukonen, L. Laitinen, J. Salonen, J. Tuura, T. Heikkila, T. Limnell, J. Hirvonen, and V. P. Lehto. Enhanced in vitro permeation of furosemide loaded into thermally carbonized mesoporous silicon (TCPSi) microparticles. *Eur J Pharm Biopharm*, 66(3):348–56, 2007.

Y. Kawabata, K. Wada, M. Nakatani, S. Yamada, and S. Onoue. Formulation design for poorly water-soluble drugs based on biopharmaceutics classification system: basic approaches and practical applications. *Int J Pharm*, 420(1):1–10, 2011.

P. Kayaert, B. Li, I. Jimidar, P. Rombaut, F. Ahssini, and G. Van den Mooter. Solution calorimetry as an alternative approach for dissolution testing of nanosuspensions. *Eur J Pharm Biopharm*, 76(3): 507–13, 2010.

G. M. Keating and K. F. Croom. Fenofibrate: A review of its use in primary dyslipidaemia, the metabolic syndrome and Type 2 Diabetes Mellitus. *Drugs*, 67(1):121–153, 2007.

F. Kesisoglou and Y. Wu. Understanding the effect of API properties on bioavailability through absorption modeling. *AAPS J*, 10(4):516–25, 2008.

F. Kesisoglou, S. Panmai, and Y. Wu. Nanosizing – oral formulation development and biopharmaceutical evaluation. *Adv Drug Deliv Rev*, 59(7):631–44, 2007.

K. Kleberg, J. Jacobsen, and A. Mullertz. Characterising the behaviour of poorly water soluble drugs in the intestine: application of biorelevant media for solubility, dissolution and transport studies. *J Pharm Pharmacol*, 62(11):1656–68, 2010.

Y. Konishi, K. Hagiwara, and M. Shimizu. Transepithelial transport of fluorescein in Caco-2 cell monolayers and use of such transport in in vitro evaluation of phenolic acid availability. *Biosci Biotechnol Biochem*, 66(11):2449–57, 2002.

R. Krishna and L. Yu. *Biopharmaceutics Applications in Drug Development*. Springer US, 2008.

R. Laakso, E. Kristoffersson, and M. Marvola. Bi-exponential first-order release kinetics of indomethacin from tablets containing polysorbate 80. *Int J Pharm*, 19(1):35–42, 1984.

T. Laaksonen, P. Liu, A. Rahikkala, L. Peltonen, E. I. Kauppinen, J. Hirvonen, K. Jarvinen, and J. Raula. Intact nanoparticulate indomethacin in fast-dissolving carrier particles by combined wet milling and aerosol flow reactor methods. *Pharm Res*, 28(10):2403–11, 2011.

T. Lange. *Neue Ansätze der Wirkstoffcharakterisierung mittels Durchflusszellen, In-vitro Wirkstofffreisetzungen und Wirkstoffpermeation*. phdthesis, 2009.

F. Langenbucher. Linearization of dissolution rate curves by the Weibull distribution. *J Pharm Pharmacol*, 24(12):979–81, 1972.

P. Langguth, G. Fricker, and H. Wunderli-Allenspach. *Biopharmazie*. WILEY-VCH Verlag GmbH & Co. KGaA, Weinheim, 2004.

P. Langguth, A. Hanafy, D. Frenzel, P. Grenier, A. Nhamias, T. Ohlig, G. Vergnault, and H. Spahn-Langguth. Nanosuspension formulations for low-soluble drugs: pharmacokinetic evaluation using spironolactone as model compound. *Drug Dev Ind Pharm*, 31(3):319–29, 2005.

S. L. Lee, A. S. Raw, and L. Yu. Dissolution testing. In R. Krishna and L. Yu, editors, *Biopharmaceutics Applications in Drug Development*, pages 47–74. Springer US, 2008.

W. Li, Y. Yang, Y. Tian, X. Xu, Y. Chen, L. Mu, Y. Zhang, and L. Fang. Preparation and in vitro/in vivo evaluation of revaprazan hydrochloride nanosuspension. *Int J Pharm*, 408(1-2):157–62, 2011.

X. Li, L. Gu, Y. Xu, and Y. Wang. Preparation of fenofibrate nanosuspension and study of its pharmacokinetic behavior in rats. *Drug Dev Ind Pharm*, 35(7):827–33, 2009.

L. Lindfors, S. Forssen, P. Skantze, U. Skantze, A. Zackrisson, and U. Olsson. Amorphous drug nanosuspensions. 2. experimental determination of bulk monomer concentrations. *Langmuir*, 22(3):911–6, 2006.

M. Linn, E. M. Collnot, D. Djuric, K. Hempel, E. Fabian, K. Kolter, and C. M. Lehr. Soluplus® as an effective absorption enhancer of poorly soluble drugs in vitro and in vivo. *Eur J Pharm Sci*, 45(3): 336–43, 2012.

C. A. Lipinski. Poor aqueous solubility – an industry wide problem in drug discovery. *Am Pharm Rev*, 5:82–85, 2002.

B. Magenheim, M. Y. Levy, and S. Benita. A new in vitro technique for the evaluation of drug release profile from colloidal carriers – ultrafiltration technique at low pressure. *Int J Pharm*, 94(1-3):115–123, 1993.

A. M. Marino, M. Yarde, H. Patel, S. Chong, and P. V. Balimane. Validation of the 96 well Caco-2 cell culture model for high throughput permeability assessment of discovery compounds. *Int J Pharm*, 297 (1-2):235–41, 2005.

N. R. Mathias and J. Crison. The use of modeling tools to drive efficient oral product design. *AAPS J*, 14(3):591–600, 2012.

R. Mellaerts, R. Mols, P. Kayaert, P. Annaert, J. Van Humbeeck, G. Van den Mooter, J. A. Martens, and P. Augustijns. Ordered mesoporous silica induces pH-independent supersaturation of the basic low solubility compound itraconazole resulting in enhanced transepithelial transport. *Int J Pharm*, 357 (1-2):169–79, 2008.

L. Mora, K. Y. Chumbimuni-Torres, C. Clawson, L. Hernandez, L. Zhang, and J. Wang. Real-time electrochemical monitoring of drug release from therapeutic nanoparticles. *J Control Release*, 140(1): 69–73, 2009.

M. Muller. Microdialysis in clinical drug delivery studies. *Adv Drug Deliv Rev*, 45(2-3):255–69, 2000.

W. Nernst. Theorie der Reaktionsgeschwindigkeit in Heterogenen Systemen. *Z Physik Chem*, 47(1): 52–55, 1904.

A. Noyes and W. R. Whitney. The rate of solution of solid substances in their own solutions. *J Am Chem Soc*, 19:930–4, 1897.

K. Ohura, H. Sakamoto, S. Ninomiya, and T. Imai. Development of a novel system for estimating human intestinal absorption using Caco-2 cells in the absence of esterase activity. *Drug Metab Dispos*, 38(2): 323–31, 2010.

I. Olver, S. Shelukar, and K. C. Thompson. Nanomedicines in the treatment of emesis during chemotherapy: focus on aprepitant. *Int J Nanomedicine*, 2(1):13–8, 2007.

W. Ostwald. Über die vermeintliche Isomerie des roten und gelben Quecksilberoxyds und die Oberflächenspannung fester Körper. *Z Physik Chem*, 34:495–503, 1900.

J. Parmentier, F. J. Hartmann, and G. Fricker. In vitro evaluation of liposomes containing bio-enhancers for the oral delivery of macromolecules. *Eur J Pharm Biopharm*, 76(3):394–403, 2010.

N. Patel, B. Forbes, S. Eskola, and J. Murray. Use of simulated intestinal fluids with Caco-2 cells and rat ileum. *Drug Dev Ind Pharm*, 32(2):151–61, 2006.

K. Quinn, R. P. Gullapalli, E. Merisko-Liversidge, E. Goldbach, A. Wong, G. G. Liversidge, W. Hoffman, J. M. Sauer, J. Bullock, and G. Tonn. A formulation strategy for gamma secretase inhibitor ELND006, a bcs class II compound: development of a nanosuspension formulation with improved oral bioavailability and reduced food effects in dogs. *J Pharm Sci*, 101(4):1462–74, 2012.

B. E. Rabinow. Nanosuspensions in drug delivery. *Nat Rev Drug Discov*, 3(9):785–96, 2004.

S. Rao, Y. Song, F. Peddie, and A. M. Evans. Particle size reduction to the nanometer range: a promising approach to improve buccal absorption of poorly water-soluble drugs. *Int J Nanomedicine*, 6:1245–51, 2011.

C. Rommel, M. Camps, and H. Ji. PI3K delta and PI3K gamma: partners in crime in inflammation in rheumatoid arthritis and beyond? *Nat Rev Immunol*, 7(3):191–201, 2007.

K. M. Rosenblatt, D. Douroumis, and H. Bunjes. Drug release from differently structured monoolein/poloxamer nanodispersions studied with differential pulse polarography and ultrafiltration at low pressure. *J Pharm Sci*, 96(6):1564–75, 2007.

W. Rubas, M. E. Cromwell, Z. Shahrokh, J. Villagran, T. N. Nguyen, M. Wellton, T. H. Nguyen, and R. J. Mrsny. Flux measurements across Caco-2 monolayers may predict transport in human large intestinal tissue. *J Pharm Sci*, 85(2):165–9, 1996.

P. Saha and J. H. Kou. Effect of bovine serum albumin on drug permeability estimation across Caco-2 monolayers. *Eur J Pharm Biopharm*, 54(3):319–24, 2002.

H. Saveyn, D. Mermuys, O. Thas, and P. van der Meeren. Determination of the refractive index of water-dispersible granules for use in laser diffraction experiments. *Particle & Particle Systems Characterization*, 19(6):426–432, 2002.

Y. Shono, E. Jantratid, F. Kesisoglou, C. Reppas, and J. B. Dressman. Forecasting in vivo oral absorption and food effect of micronized and nanosized aprepitant formulations in humans. *Eur J Pharm Biopharm*, 76(1):95–104, 2010.

K. Sigfridsson, A. Nordmark, S. Theilig, and A. Lindahl. A formulation comparison between micro- and nanosuspensions: the importance of particle size for absorption of a model compound, following repeated oral administration to rats during early development. *Drug Dev Ind Pharm*, 37(2):185–92, 2011.

P. J. Sinko. *Martin´s Physical Pharmacy and Pharmaceutical Science*. Lippincott Williams & Wilkins, 5 edition, 2005.

K. Sugano, A. Okazaki, S. Sugimoto, S. Tavornvipas, A. Omura, and T. Mano. Solubility and dissolution profile assessment in drug discovery. *Drug Metab Pharmacokinet*, 22(4):225–54, 2007.

Y. Takahashi, H. Kondo, T. Yasuda, T. Watanabe, S. Kobayashi, and S. Yokohama. Common solubilizers to estimate the Caco-2 transport of poorly water-soluble drugs. *Int J Pharm*, 246(1-2):85–94, 2002.

R. Takano, K. Sugano, A. Higashida, Y. Hayashi, M. Machida, Y. Aso, and S. Yamashita. Oral absorption of poorly water-soluble drugs: computer simulation of fraction absorbed in humans from a miniscale dissolution test. *Pharm Res*, 23(6):1144–56, 2006.

S. Tavelin, J. Grå sjö, J. Taipalensuu, G. Ocklind, P. Artursson, and C. Wise. Applications of epithelial cell culture in studies of drug transport epithelial cell culture protocols. volume 188 of *Methods in Molecular Biology*, pages 233–272. Humana Press, 2002.

T. Tay, A. Allahham, D. A. Morton, and P. J. Stewart. Understanding improved dissolution of indomethacin through the use of cohesive poorly water-soluble aluminium hydroxide: Effects of concentration and particle size distribution. *J Pharm Sci*, 100(10):4269–4280, 2011.

M. Thanou, J. C. Verhoef, and H. E. Junginger. Chitosan and its derivatives as intestinal absorption enhancers. *Adv Drug Deliv Rev*, 50 Suppl 1:S91–101, 2001.

A. P. Tinke, K. Vanhoutte, R. De Maesschalck, S. Verheyen, and H. De Winter. A new approach in the prediction of the dissolution behavior of suspended particles by means of their particle size distribution. *J Pharm Biomed Anal*, 39(5):900–7, 2005.

K. Tsinman, A. Avdeef, O. Tsinman, and D. Voloboy. Powder dissolution method for estimating rotating disk intrinsic dissolution rates of low solubility drugs. *Pharm Res*, 26(9):2093–100, 2009.

K. Tsutsumi, S. K. Li, A. H. Ghanem, N. F. Ho, and W. I. Higuchi. A systematic examination of the in vitro ussing chamber and the in situ single-pass perfusion model systems in rat ileum permeation of model solutes. *J Pharm Sci*, 92(2):344–59, 2003.

C. J. Tucker. Real time monitoring of small particle dissolution by way of light scattering. US Patent, 2002.

H. C. van de Hulst. *Light scattering by Small Particles*. John Wiley & Sons, Inc., New York, 1957.

B. Van Eerdenbrugh, G. Van den Mooter, and P. Augustijns. Top-down production of drug nanocrystals: nanosuspension stabilization, miniaturization and transformation into solid products. *Int J Pharm*, 364 (1):64–75, 2008.

B. Van Eerdenbrugh, J. Vermant, J. A. Martens, L. Froyen, J. V. Humbeeck, G. Van den Mooter, and P. Augustijns. Solubility increases associated with crystalline drug nanoparticles: Methodologies and significance. *Mol Pharm*, 7(5):1858–1870, 2010.

B. Van Eerdenbrugh, D. E. Alonzo, and L. S. Taylor. Influence of particle size on the ultraviolet spectrum of particulate-containing solutions: implications for in-situ concentration monitoring using UV/Vis fiber-optic probes. *Pharm Res*, 28(7):1643–52, 2011.

D. A. Volpe. Variability in Caco-2 and mdck cell-based intestinal permeability assays. *J Pharm Sci*, 97 (2):712–25, 2008.

J. Wang and D. R. Flanagan. General solution for diffusion-controlled dissolution of spherical particles. 1. theory. *J Pharm Sci*, 88(0022-3549 (Print)):731–738, 1999.

Y. Wang, D. Zhang, Z. Liu, G. Liu, C. Duan, L. Jia, F. Feng, X. Zhang, Y. Shi, and Q. Zhang. In vitro and in vivo evaluation of silybin nanosuspensions for oral and intravenous delivery. *Nanotechnology*, 21(15):155104, 2010.

J. Wegener, D. Abrams, W. Willenbrink, H. J. Galla, and A. Janshoff. Automated multi-well device to measure transepithelial electrical resistances under physiological conditions. *Biotechniques*, 37(4): 590, 592–4, 596–7, 2004.

Y. Wu, A. Loper, E. Landis, L. Hettrick, L. Novak, K. Lynn, C. Chen, K. Thompson, R. Higgins, U. Batra, S. Shelukar, G. Kwei, and D. Storey. The role of biopharmaceutics in the development of a clinical nanoparticle formulation of MK-0869: a beagle dog model predicts improved bioavailability and diminished food effect on absorption in human. *Int J Pharm*, 285(1-2):135–46, 2004.

D. Xia, F. Cui, H. Piao, D. Cun, Y. Jiang, M. Ouyang, and P. Quan. Effect of crystal size on the in vitro dissolution and oral absorption of nitrendipine in rats. *Pharm Res*, 27(9):1965–76, 2010.

K. Yano, Y. Masaoka, M. Kataoka, S. Sakuma, and S. Yamashita. Mechanisms of membrane transport of poorly soluble drugs: role of micelles in oral absorption processes. *J Pharm Sci*, 99(3):1336–45, 2010.

M. Yazdanian, S. L. Glynn, J. L. Wright, and A. Hawi. Correlating partitioning and Caco-2 cell perme-
ability of structurally diverse small molecular weight compounds. *Pharm Res*, 15(9):1490–4, 1998.

J. Yguerabide and E. E. Yguerabide. Light-scattering submicroscopic particles as highly fluorescent
analogs and their use as tracer labels in clinical and biological applications. *Anal Biochem*, 262(2):
157–76, 1998.

H. Yu and P. J. Sinko. Influence of the microporous substratum and hydrodynamics on resistances to
drug transport in cell culture systems: calculation of intrinsic transport parameters. *J Pharm Sci*, 86
(12):1448–57, 1997.

L. X. Yu, J. R. Crison, and G. L. Amidon. Compartmental transit and dispersion model analysis of small
intestinal transit flow in humans. *Int J Pharm*, 140(1):111–118, 1996a.

L. X. Yu, E. Lipka, J. R. Crison, and G. L. Amidon. Transport approaches to the biopharmaceutical
design of oral drug delivery systems: prediction of intestinal absorption. *Adv Drug Deliv Rev*, 19(3):
359–76, 1996b.

H. Y. Yun, E. Joo Lee, S. Youn Chung, S. O. Choi, H. Kee Kim, J. T. Kwon, W. Kang, and K. I. Kwon.
The effects of food on the bioavailability of fenofibrate administered orally in healthy volunteers via
sustained-release capsule. *Clin Pharmacokinet*, 45(4):425–32, 2006.

T. Zhu, J. C. Ansquer, M. T. Kelly, D. J. Sleep, and R. S. Pradhan. Comparison of the gastrointestinal
absorption and bioavailability of fenofibrate and fenofibric acid in humans. *J Clin Pharmacol*, 50(8):
914–21, 2010.

List of Abbreviations

ACAT	Advanced Compartmental Absorption and Transit model
AcN	acetonitrile
API	active pharmaceutical ingredient
AS	Merck Serono Compound AS
ATP	adenosine triphosphate
BCS	Biopharmaceutical classification system
DLS	dynamic light scattering
DMEM	Dulbecco´s modified Eagle´s medium
DOSS	dioctyl sulfosuccinate sodium salt
DSC	differential scanning calorimetry
FaSSIF	fasted state simulated intestinal fluid
FF	fenofibrate
FFA	fenofibric acid
GF	griseofulvin
GI	gastrointestinal
HBSS	Hanks´ balanced salts solution
HPLC	high pressure liquid chromatography
HPMC	hydroxypropylmethylcellulose
i.v.	intravenous
IPC	in-process control
ITC	isothermal titration calorimetry

KC	ketoconazole
kcps	kilo counts per second
MRP	multidrug resistance protein
MS	microsuspension
NMR	nuclear magnetic resonance spectroscopy
NS	nanosuspension
NTA	nanoparticle tracking analysis
P-gp	P-glycoprotein
p.o.	peroral
PBS	phosphate buffered saline
PDI	polydispersity index
Ph. Eur.	Pharmacopoeia Europaea
PK	pharmacokinetic
PZN	Pharma Zentral Nummer
rpm	rounds per minute
SEM	scanning electron microscopy
SGF	simulated gastric fluid
SGF + Tween	simulated gastric fluid supplemented with 0.1% polysorbate 80
SLS	static light scattering
TEER	trans epithelial electrical resistance
TFA	trifluoroacetic acid
TOC	total organic carbon
USP	United States Pharmacopeia
UWL	unstirred water layer
vs	versus

Danksagung

für seinen Einsatz bei diversen Softwareangelegenheiten.

Allen Kollegen aus Exploratory Pharmaceutical Development bei Merck Serono danke ich für ihre Hilfe, ihren Rat und eine angenehme Atmosphäre inner- und außerhalb des Werksgeländes. Vor allem richtet sich mein persönlicher Dank an Patrizia Boniforte, Annette Eppler, Agnes Fekete, Nadja Foster, Meike Harms, Alexandra Hill, Tobias Miller, Stefan Schiller und Bernd Sterner.

Für ihre Unterstützung gilt mein Dank ebenso allen Kollegen aus der Abteilung für Pharmazeutische Technologie und Biopharmazie am Institut in Heidelberg: Alexandra Bernd, Kerstin Frank, Dominik Gartzke, Nassim Heshmati, Evelyn Hollnack-Pusch, Olga Huber, Sarah Fischer, Johanna Kanzer, Julianne Kläs, Marise Kolter, Anne Mahringer, Sabrina Nickel, Silvia Pantze, Johannes Parmentier, Fabian Polyak, Sonia Rust, Hendrik Schneider und Christoph Vogel.

Von Herzen möchte abschließend den Menschen danken, ohne die ich nicht stehen würde wo ich heute angekommen bin. Mein Dank gilt meiner Familie und Raoul.

Meine Eltern, mein Bruder, meine Großeltern und meine Tante ermöglichten es mir meinen Weg zu finden und zu gehen. Sie standen mir stets als vertrauensvolle Begleiter und Ratgeber zur Seite. Im Besonderen danke ich meiner Mutter und meinem Bruder Peter, die immer für mich da sind und mir Kraft geben. Raoul bin ich sehr dankbar für sein unerschütterliches Vertrauen in mich und meine Fähigkeiten. Er stärkte mich und begleitete mich durch Höhen und Tiefen. Er war mir ein wichtiger Berater und Ruhepol. In einzigartiger Weise hielt er mir in arbeitsreichen Zeiten den Rücken frei.

Ihre Liebe und ihr Zuspruch geben mir Halt und Motivation. Ich danke ihnen sehr dafür.